# Magnetic Induction in Convecting Galilean Oceans

Steven Douglas Vance[1,1], Bruce G Bills[1,1], Corey J Cochrane[1,1], Krista M. Soderlund[2,2], N. Gómez-Pérez[3,3], M. J Styczinski[4,4], and Carol S Paty[5,5]

[1]Jet Propulsion Laboratory, California Institute of Technology
[2]University of Texas at Austin
[3]British Geologic Survey
[4]University of Washington
[5]University of Oregon

November 30, 2022

**Abstract**

To date, analyses of magnetic induction in putative oceans in Jupiter's large icy moons have assumed uniform conductivity in the modeled oceans. However, the phase and amplitude response of the induced fields will be influenced by the increasing electrical conductivity along oceans' convective adiabatic temperature profiles. Here, we examine the amplitudes and phase lags for magnetic diffusion in modeled oceans of Europa, Ganymede, and Callisto. We restrict our analysis to spherically symmetric configurations, treating interior structures based on self-consistent thermodynamics, accounting for variations in electrical conductivity with depth in convective oceans (missing citation). The numerical approach considers tens of radial layers. The induction response of the adiabatic conductivity profile differs from that of an ocean with uniform conductivity set to that at the ice-ocean interface, or to the mean value of the adiabatic profile, by more than 10\% in many cases. We compare these modeled signals with magnetic fields induced by oceanic fluid motions that might be used to measure oceanic flows (missing citation); (missing citation); (missing citation). For turbulent convection (missing citation), we find that these signals can dominate induction signal at low latitudes, underscoring the need for spatial coverage in magnetic investigations. Based on end-member ocean compositions (missing citation); (missing citation), we quantify the residual magnetic induction signals that might be used to infer the oxidation state of Europa's ocean and to investigate stable liquids under high-pressure ices in Ganymede and Callisto. Fully exploring this parameter space for the sake of planned missions requires electrical conductivity measurements in fluids at low temperature and to high salinity and pressure.

## References

# Magnetic Induction in Convecting Galilean Oceans

**S. D. Vance[1], B. G. Bills[1], C. J. Cochrane[1], K. M. Soderlund[2], N. Gómez-Pérez[3], M. J. Styczinski[4], and C. Paty[5]**

[1]Jet Propulsion Laboratory, California Institute of Technology, Pasadena, USA
[2]Institute for Geophysics, John A. & Katherine G. Jackson School of Geosciences, The University of Texas at Austin, USA
[3]British Geological Survey, Edinburgh, UK
[4]Dept. of Physics, University of Washington, Seattle, USA
[5]Dept. of Earth Sciences, University of Oregon, Eugene, USA

**Key Points:**

- Diffusive induction accounting for adiabatic ocean temperatures is distinct in phase and amplitude from induction based on electrical conductivity at the ice-ocean interface
- Based on turbulent global convection models, oceanic flows may generate induced magnetic fields observable by planned spacecraft missions
- Determining ocean composition from magnetic induction requires additional thermodynamic and electrical conductivity data

Corresponding author: S. D. Vance, `svance@jpl.caltech.edu`

## Abstract

To date, analyses of magnetic induction in putative oceans in Jupiter's large icy moons have assumed uniform conductivity in the modeled oceans. However, the phase and amplitude response of the induced fields will be influenced by the increasing electrical conductivity along oceans' convective adiabatic temperature profiles. Here, we examine the amplitudes and phase lags for magnetic diffusion in modeled oceans of Europa, Ganymede, and Callisto. We restrict our analysis to spherically symmetric configurations, treating interior structures based on self-consistent thermodynamics, accounting for variations in electrical conductivity with depth in convective oceans (Vance et al., 2018). The numerical approach considers tens of radial layers. The induction response of the adiabatic conductivity profile differs from that of an ocean with uniform conductivity set to that at the ice-ocean interface, or to the mean value of the adiabatic profile, by more than 10% in many cases. We compare these modeled signals with magnetic fields induced by oceanic fluid motions that might be used to measure oceanic flows (e.g., Chave, 1983; Minami, 2017; Tyler, 2011). For turbulent convection (Soderlund et al., Soderlund et al.2014), we find that these signals can dominate induction signal at low latitudes, underscoring the need for spatial coverage in magnetic investigations. Based on end-member ocean compositions (Zolotov, 2008; Zolotov & Kargel, 2009), we quantify the residual magnetic induction signals that might be used to infer the oxidation state of Europa's ocean and to investigate stable liquids under high-pressure ices in Ganymede and Callisto. Fully exploring this parameter space for the sake of planned missions requires electrical conductivity measurements in fluids at low temperature and to high salinity and pressure.


## 1 Introduction

The jovian system is of particular interest for studying magnetic induction in icy ocean worlds. Jupiter has a strong magnetic field whose dipole axis is tilted 9.5° with respect to its rotation axis (Acuna & Ness, 1976), while the orbits of the Galilean moons lie very nearly in the equatorial plane of Jupiter. This means that Jupiter?s magnetic field varies in time at the orbital positions of the satellites. Also, the outer layers of the satellites themselves are believed to consist mainly of water ice at the surface, underlain by salty oceans. Brines are good conductors, while ice is a significant insulator.

Magnetic induction from Jupiter's diurnal signal sensed by the *Galileo* mission provides the most compelling direct observational evidence for the existence of oceans within Europa and Ganymede (Hand & Chyba, 2007; K. Khurana, Kivelson, Hand, & Russell, 2009; Khurana et al., 1998; Kivelson et al., 2000; Saur, Strobel, & Neubauer, 1998; Schilling, Neubauer, & Saur, 2007). The case has also been made for an induction response from an ocean in Callisto (Zimmer, Khurana, & Kivelson, 2000), but this interpretation is clouded by possible ionospheric interference (Hartkorn & Saur, 2017; Liuzzo, Feyerabend, Simon, & Motschmann, 2015).

Longer period signals penetrate more deeply, as penetration of the magnetic field into the interior is a diffusive process. It is convenient that the skin depths at the dominant periods of variation experienced by Europa, Ganymede, and Callisto are comparable to the expected ocean depths, which makes it possible to probe the properties of their oceans using magnetic induction. The spectrum of frequencies driving induced magnetic responses includes not just the orbits of the Galilean satellites and the rotation of Jupiter's tilted dipole field, but also their harmonics and natural oscillations (Saur, Neubauer, & Glassmeier, 2009; Seufert, Saur, & Neubauer, 2011). Electrical conductivity structure within the subsurface oceans—for example, from convective adiabatic temperature gradients (Vance et al., 2018) and stratification (Vance & Goodman, 2009a)—will respond at these frequencies.

Further variations in the magnetic fields arise from the motion of the moons about Jupiter. Perturbations to the orbits of the moons arise from multiple sources, including the oblate figure of Jupiter, gravitational interactions with the other satellites, and even from Saturn and the Sun (Lainey, Duriez, & Vienne, 2006; Lieske, 1998).

Here, we examine the amplitudes and phase lags for magnetic diffusion in modeled oceans of Europa, Ganymede, and Callisto. We restrict our analysis to spherically symmetric configurations, treating interior structures based on self-consistent thermodynamics, which account for variations in electrical conductivity with depth in convective oceans (Vance et al., 2018). In addition, we consider the generation of induced magnetic fields by oceanic fluid motions that may bias the interpretation of a satellite's magnetic behavior if not accommodated and which, more optimistically, might be used to probe the ocean flows directly (e.g., Chave, 1983; Minami, 2017; Tyler, 2011). Based on end-member ocean compositions (Zolotov, 2008; Zolotov & Kargel, 2009), we demonstrate the possibilities for using magnetic induction to infer the oxidation state of Europa's ocean and to identify stable liquid layers under high-pressure ices in Ganymede and Callisto.

In Section 2 we describe a numerical method for computing the induction response. Section 3 examines the diffusive induction response of Jupiter's ocean moons, first describing the frequency content of temporal variations in Jupiter's field in the reference frames of the Galilean moons (S 3.1), then the interior structure models that include layered electrical conductivity consistent with the modeled compositions (S 3.2). In Section 3.3, we detail the corresponding amplitude and phase responses of the diffusive magnetic induction, and finally in Section 3.4, we compare the diffusive fields to the field imposed by Jupiter. Section 4 describes simulations of oceanic flows (S 4.1) and resulting magnetic induction (S 4.2) that adds to the diffusive component. Section 5 describes the prospects for detecting these different signals.

## 2 Induction Response Model

We are interested in the magnetic fields induced within a spherically symmetric body, in which electrical conductivity is a piece-wise constant function of distance from the center. We thus assume bounding radii

$$\{r_1, r_2, r_3, \cdots, r_m\} \tag{1}$$

where

$$r_m = R \tag{2}$$

is the outer radius of the spherical body.

The corresponding conductivity values are

$$\{\sigma_1, \sigma_2, \sigma_3, \cdots, \sigma_m\} \tag{3}$$

We also assume that there is an imposed external magnetic potential, represented by a sum of terms, each of which has the form

$$\Phi[r, \theta, \phi, t] = R\ B_e \left(\frac{r}{R}\right)^n S_{n,m}[\theta, \phi]\ \ \exp[-i\ \omega\ t] \tag{4}$$

where $\{r, \theta, \phi\}$ are spherical coordinates ($r$ is radius, $\theta$ is colatitude, and $\phi$ is longitude) of the field point, $B_e$ is a scale factor, $S_{n,m}[\theta, \phi]$ is a surface spherical harmonic function of degree $n$ and order $m$, while $t$ is time and $\omega$ is the frequency of oscillation of the imposed potential.

Within each layer, the magnetic field vector $B$ must satisfy the differential equation

$$\nabla^2 B = -k^2 B \tag{5}$$

where $k$ is a scalar wavenumber given by

$$k^2 = i\ \omega\ \mu_0\ \sigma \tag{6}$$

where $\omega$ is frequency, $\sigma$ is electrical conductivity, and the magnetic constant (permeability of free space) is given by

$$\mu_0 = 4\pi \times 10^{-7} N/A^2 \tag{7}$$

with units $N$ and $A$ being Newton and Ampere.

### 2.1 Radial Basis Functions

The poloidal component of the magnetic field inside the body is given by sums of terms with the forms

$$B_r[r,\theta,\phi,t] = \frac{C}{r}\,(F[r])\ \ n(n+1)\ S_{n,m}[\theta,\phi]\ \ \exp[-i\ \omega\ t] \tag{8}$$

$$B_\theta[r,\theta,\phi,t] = \frac{C}{r}\left(\frac{d\ rF[r]}{dr}\right)\ \ \frac{dS_{n,m}[\theta,\phi]}{d\theta}\exp[-i\ \omega\ t] \tag{9}$$

$$B_\phi[r,\theta,\phi,t] = \frac{C}{r\sin[\theta]}\left(\frac{d\ rF[r]}{dr}\right)\ \ \frac{dS_{n,m}[\theta,\phi]}{d\phi}\exp[-i\ \omega\ t] \tag{10}$$

where $C$ is a constant, and $F[r]$ is a function of radius, which we need to determine.

Applying separation of variables to the governing differential equation (5), one finds that the radial factor $F[r]$ in the solution must satisfy the ordinary differential equation

$$\frac{d^2F}{dr^2} + \left(\frac{2}{r}\right)\frac{dF}{dr} + (k^2 - \frac{n(n+1)}{r^2})F = 0 \tag{11}$$

This is a second order equation having two solutions:

$$F_n^+[r] = j_n[k\ r] \tag{12}$$

$$F_n^-[r] = y_n[k\ r] \tag{13}$$

where $j_n[x]$ is a spherical Bessel function of the first kind of order $n$, and argument $x$, and $y_n[x]$ is a spherical Bessel function of the second kind.

It will also be convenient to define another set of related functions

$$\begin{aligned} G_n^+[r] &= \frac{d}{dr}\left(r\ F_n^+[r]\right) \\ &= (n+1)\ \ j_n[k\ r] - (k\ r)\ \ j_{n+1}[k\ r] \end{aligned} \tag{14}$$

and

$$\begin{aligned} G_n^-[r] &= \frac{d}{dr}\left(r\ F_n^-[r]\right) \\ &= (n+1)\ \ y_n[k\ r] - (k\ r)\ \ y_{n+1}[k\ r] \end{aligned} \tag{15}$$

In the magnetic induction problem, as applied to the Galilean satellites, the only case of interest is for an imposed dipole field, where $n = 1$. In that case, the radial basis functions for the radial component of the field, are

$$\begin{aligned} F_1^+[k\ r] &= j_1[k\ r] \\ &= \frac{\sin[k\ r] - (k\ r)\cos[k\ r]}{(k\ r)^2} \end{aligned} \tag{16}$$

and

$$\begin{aligned} F_1^-[k\ r] &= y_1[k\ r] \\ &= \frac{-\cos[k\ r] - (k\ r)\sin[k\ r]}{(k\ r)^2} \end{aligned} \tag{17}$$

In similar fashion, the radial basis functions for the transverse components are

$$\begin{aligned} G_1^+[k\ r] &= 2\ j_1[k\ r] - (k\ r)\ j_2[k\ r] \\ &= \frac{(k\ r)\cos[k\ r] - \left(1 - k^2\ r^2\right)\sin[k\ r]}{(k\ r)^2} \end{aligned} \tag{18}$$

and

$$\begin{aligned} G_1^-[k\ r] &= 2\ y_1[k\ r] - (k\ r)\ y_2[k\ r] \\ &= \frac{(k\ r)\sin[k\ r] + \left(1 - k^2\ r^2\right)\cos[k\ r]}{(k\ r)^2} \end{aligned} \tag{19}$$

In both cases, the latter form is singular at the origin ($r = 0$), so in the innermost spherical layer, we only use $F^+[k\ r]$ and $G^+[k\ r]$. In other layers, we use linear combinations of $F^+$ and $F^-$ and linear combinations of $G^+$ and $G^-$.

### 2.2 Internal Boundary Conditions

The resulting piece-wise-defined radial functions characterize the radial part of the magnetic field. The radial component has the form

$$F[r] = \begin{cases} c_1\ F^+[k_1 r] & \text{if} \quad 0 < r \le r_1 \\ c_2\ F^+[k_2 r] \quad + d_2\ F^-[k_2 r] & \text{if} \quad r_1 < r \le r_2 \\ c_3\ F^+[k_3 r] \quad + d_3\ F^-[k_3 r] & \text{if} \quad r_2 < r \le r_3 \\ \\ c_m\ F^+[k_m r] \quad + d_m\ F^-[k_m r] & \text{if} \quad r_{m-1} < r \le r_m \end{cases} \tag{20}$$

The transverse components yield similar structure, but with $G$ replacing $F$.

The constants $c_j$ and $d_j$ are determined by continuity of radial ($r$) and transverse ($\theta, \phi$) components of the magnetic field across the boundaries. For each internal boundary, it must hold that

$$\begin{aligned} F[r_j] &= c_j\ F^+\left[k_j\ r_j\right] + d_j\ F^-\left[k_j\ r_j\right] \\ &= c_{j+1}\ F^+\left[k_{j+1}\ r_j\right] + d_{j+1}\ F^-\left[k_{j+1}\ r_j\right] \end{aligned} \tag{21}$$

to ensure continuity of the radial component of the magnetic field, and likewise for $G$ to ensure continuity of the transverse components. These continuity constraints yield two equations at each internal boundary, from which we can determine the layer coefficients.

The internal boundary conditions are only part of the story. In a model with $m$ layers, we have $2m - 1$ coefficients to determine (recall that $d_1 = 0$, to avoid singular behavior at the origin), but only $m - 1$ internal boundaries, and thus only $2m - 2$ constraints. The external boundary condition provides the additional information to make the problem evenly determined.

Even without the external boundary condition, a provisional solution is obtained by setting $c_1 = 1$ and using the internal boundary constraints to determine the other coefficient values. Using notation similar to that of Parkinson (1983, page 314), we can write a recursion relation that transforms the coefficients in the $j$th layer into those for the layer above it

$$\begin{bmatrix} c_{j+1} \\ d_{j+1} \end{bmatrix} = T_j[k_j, k_{j+1}, r_j] \cdot \begin{bmatrix} c_j \\ d_j \end{bmatrix} \tag{22}$$

where the transformation matrix has elements

$$T_j[k_j, k_{j+1}, r_j] = \frac{1}{\alpha_j} \begin{bmatrix} \beta_j & \gamma_j \\ \delta_j & \varepsilon_j \end{bmatrix} \tag{23}$$

with

$$\alpha_j = F^+ [k_{j+1} \ r_j] * G^- [k_{j+1} \ r_j] - F^- [k_{j+1} \ r_j] * G^+ [k_{j+1} \ r_j] \tag{24}$$

which is a function of the conductivity in the layer above the boundary only. The other elements depend on the conductivities on both sides of the boundary

$$\beta_j = F^+ [k_j \ \ r_j] * G^- [k_{j+1} \ r_j] - F^- [k_{j+1} \ r_j] * G^+ [k_j \ \ r_j] \tag{25}$$

$$\gamma_j = F^- [k_j \ \ r_j] * G^- [k_{j+1} \ r_j] - F^- [k_{j+1} \ r_j] * G^- [k_j \ \ r_j] \tag{26}$$

and

$$\delta_j = F^+ [k_{j+1} \ r_j] * G^+ [k_j \ \ r_j] - F^+ [k_j \ \ r_j] * G^+ [k_{j+1} \ r_j] \tag{27}$$

$$\varepsilon_j = F^+ [k_{j+1} \ r_j] * G^- [k_j \ \ r_j] - F^- [k_j \ \ r_j] * G^+ [k_{j+1} \ r_j] \tag{28}$$

We thus start in the central spherical layer, with $c_1 = 1$ and $d_1 = 0$, and then propagate upward through the stack of layers until we have the coefficients in each of the $m$ layers. This set of layer coefficients, with the radial basis functions, yields structures as given in equations (22) and (23).

### 2.3 External Boundary Conditions

The final step is matching the external surface boundary condition. Outside the sphere, the magnetic field is represented by a scalar potential which is the sum of an imposed external contribution and an induced internal contribution. That sum has spatial dependence given by the form

$$\Phi[r, \theta, \phi] = R \left( B_e \left(\frac{r}{R}\right)^n + B_i \left(\frac{R}{r}\right)^{n+1} \right) S_n[\theta, \phi] \tag{29}$$

We have dropped the subscript $m$ from $S_{n,m}$ because a suitable choice of axes results in $m = 0$ for both external and internal fields for the case of spherical symmetry we consider here. The vector field is obtained from the potential via

$$B = -\nabla\Phi \tag{30}$$

The radial component of the vector field, evaluated at the surface ($r = R$), is

$$B_r = -\left(n \ B_e - (n+1)B_i\right) S_n[\theta, \phi] \tag{31}$$

and the tangential components are

$$B_\theta = -(B_e + B_i)\frac{\partial S_n[\theta, \phi]}{\partial \theta} \tag{32}$$

and

$$B_\phi = -(B_e + B_i)\frac{1}{\sin[\theta]}\frac{\partial S_n[\theta, \phi]}{\partial \phi} \tag{33}$$

Matching these with the corresponding interior components, as given in equations (8), (9), and (10), but evaluated at the top of the upper-most layer, we obtain

$$-(n \ B_e - (n+1) \ B_i)R = n \ (n+1) \ (c_m \ F^+[k_m \ R] + d_m \ F^-[k_m \ R]) \tag{34}$$

and

$$-(B_e + B_i)R = \left(c_m \ G^+[k_m \ R] + d_m \ G^-[k_m \ R]\right) \tag{35}$$

From these two equations, we can first solve for $B_e$ and $B_i$. The result is

$$\widehat{B}_e = \frac{-1}{R(2n+1)} \left(c_m \; A_m + d_m \; B_m\right) \tag{36}$$

$$\widehat{B}_i = \frac{1}{R(2n+1)} \left(c_m \; C_m + d_m \; D_m\right) \tag{37}$$

where we introduce $\widehat{B}_e$ and $\widehat{B}_i$ to distinguish solutions in terms of internal properties from the external and induced magnetic moments. We also define the parameters $A_m$, $B_m$, $C_m$, and $D_m$ by

$$\begin{aligned} A_m &= (n+1)\left(n \; F^{+}[k_m \; R] + \; G^{+}[k_m \; R]\right) \\ B_m &= (n+1)\left(n \; F^{-}[k_m \; R] + \; G^{-}[k_m \; R]\right) \end{aligned} \tag{38}$$

and

$$\begin{aligned} C_m &= n\left((n+1)\, F^{+}[k_m \; R] - G^{+}[k_m \; R]\right) \\ D_m &= n\left((n+1)\, F^{-}[k_m \; R] - G^{-}[k_m \; R]\right) \end{aligned} \tag{39}$$

As previously noted, choice of $c_1 = 1$ permits solution of layer coefficients $c_j$ and $d_j$ relative to each other with only knowledge of the interior properties. We can then solve for $\widehat{B}_e$ and $\widehat{B}_i$ in terms of the interior structure quantities $k_j$ and $r_j$. We can then conveniently relate this to the magnetic field that will be induced from the conducting body for a given external field $B_e^*$ by introducing a scale factor:

$$S = \frac{B_e^*}{\widehat{B}_e} \tag{40}$$

Choosing a normalized value of

$$B_e^* = 1 \tag{41}$$

means that physically correct layer coefficients may be determined by multiplying the magnitude of the applied external field to the coefficients $c_j^*$ and $d_j^*$, obtained from

$$\begin{bmatrix} c_j^* \\ d_j^* \end{bmatrix} = S \begin{bmatrix} c_j \\ d_j \end{bmatrix} \tag{42}$$

For an applied external field $B_e^*$ in real units, the physical magnetic field within each layer is then given by

$$\begin{aligned} B_{r,j}[r,\theta,\phi,t] &= \frac{B_e^*}{r}\left(c_j^* F^{+}[k_j r] + d_j^* F^{-}[k_j r]\right) n(n+1) S_n[\theta,\phi] \;\exp[-i \; \omega \; t] \\ B_{\theta,j}[r,\theta,\phi,t] &= \frac{B_e^*}{r}\left(c_j^* G^{+}[k_j r] + d_j^* G^{-}[k_j r]\right) \frac{dS_n[\theta,\phi]}{d\theta} \;\exp[-i \; \omega \; t] \\ B_{\phi,j}[r,\theta,\phi,t] &= \frac{B_e^*}{r\sin[\theta]}\left(c_j^* G^{+}[k_j r] + d_j^* G^{-}[k_j r]\right) \frac{dS_n[\theta,\phi]}{d\phi} \;\exp[-i \; \omega \; t] \end{aligned} \tag{43}$$

The ratio of internal and external field strengths at the exterior surface is given from equations (36) and (37) via

$$Q \equiv \frac{\widehat{B}_i}{\widehat{B}_e} = -\frac{c_m^* \; C_m + d_m^* \; D_m}{c_m^* \; A_m + d_m^* \; B_m} \tag{44}$$

In Zimmer et al. (2000) and Khurana et al. (2009), this complex ratio is written as the product of a real magnitude and a phase shift:

$$Q = A^* \exp[i \; \gamma^*] \tag{45}$$

where $A^*$ is a positive real number representing amplitude and $\gamma^*$ is a real number representing the phase of the induced field relative to the imposed field.

In the aforementioned previous work, an explicit formula is given for the result from a 3-layer model, in which the conductivities in the innermost ($j = 1$) and outermost ($j = 3$) layers are zero, and the middle layer (intended to represent a salty ocean in Europa) has a finite conductivity. In this model, there are essentially four free parameters—3 bounding radii ($r_1, r_2, r_3$) and a middle layer conductivity ($\sigma_2$)—that determine the critical wavenumber ($k_2$). We refer to this model as the ocean-only model.

In our notation, the resulting ratio $Q$ for the ocean-only model is

$$Q \;=\; \frac{-n}{n+1}\,\frac{j_{n+1}[k_2\ r_1] * y_{n+1}[k_2\ r_2] - j_{n+1}[k_2\ r_2] * y_{n+1}[k_2\ r_1]}{j_{n+1}[k_2\ r_1] * y_{n-1}[k_2\ r_2] - j_{n-1}[k_2\ r_2] * y_{n+1}[k_2\ r_1]} \tag{46}$$

Because we know the complex phase of the wavenumber $k$, we can use properties of Bessel functions to solve for the amplitude and phase for the induced magnetic field. We defined $k^2 = i\omega\mu\sigma$ (Eq. 6), so $k = \exp[i\pi/4]\sqrt{\omega\mu\sigma}$. The (real) magnitude of $k$ is $|k| = \sqrt{\omega\mu\sigma}$, and all layers will have the same complex phase $\pi/4$. We can therefore express the wavenumber for each layer as

$$k_j = \kappa_j \exp[i\pi/4], \quad \kappa_j = \sqrt{\omega\mu_j\sigma_j} \tag{47}$$

When $\kappa_2 r_2$ is large, $j_{n+1}[\kappa_2\, r_2] = -j_{n-1}[\kappa_2\ r_2]$ and $y_{n+1}[\kappa_2\, r_2] = -y_{n-1}[\kappa_2\ r_2]$. We can make use of these relations to note that the amplitude and phase for the induced magnetic field for a perfectly conducting sphere of radius $r_2$ will be $n/(n+1)$ and 0, respectively. Thus, we can also define an amplitude and phase for the induction response relative to those for a perfectly conducting sphere of radius $R$:

$$A = A^*\,\frac{n+1}{n}\left(\frac{r_2}{R}\right)^3, \quad \gamma = \gamma^* \tag{48}$$

A perfectly conducting sphere of radius $R$ therefore has a relative amplitude of $A = 1$ and $\gamma = 0$.

# 3 Diffusive Induction in Jupiter's Ocean Moons

## 3.1 Spectral Content of the Imposed Magnetic Field Variations

Temporal variations in the magnetic field occur in the reference frames of Jupiter's satellites. Figure 1 shows the strongest components, arising from the orbital and synodic periods and their harmonics. Seufert et al. (2011) determined the frequency spectra for the time-varying magnetic perturbations applied to each of the four Galilean moons based on the VIP4 model of J. Connerney, Acuna, Ness, and Satoh (1998) and the Jovian current sheet model of Khurana (1997). Seufert et al. (2011) also examined the frequency spectra of magnetic perturbations from dynamic migration of the Jovian magnetopause based on solar wind data from the Ulysses spacecraft, which we do not consider here.

To calculate the frequencies, we first compute the magnetic field using the JRM09 Jupiter field model accounting for Juno measurements (J. E. P. Connerney et al., 2018) and using the plasma sheet model from Khurana (1997). We then compute the field at the orbital positions of the moons using the most recent and up-to-date NAIF-produced spice kernels and three years of data covering the duration of the Europa Clipper mission (tour 17F12v2). Finally, we compute the Fourier transform of the entire data sets to determine the induction frequencies.

The temporal variations in imposed magnetic field at each satellite depend on the orbits of the satellites and the magnetic field of Jupiter. To find them, we compute Jupiter's magnetic field in a Jupiter-centered coordinate system from a spherical

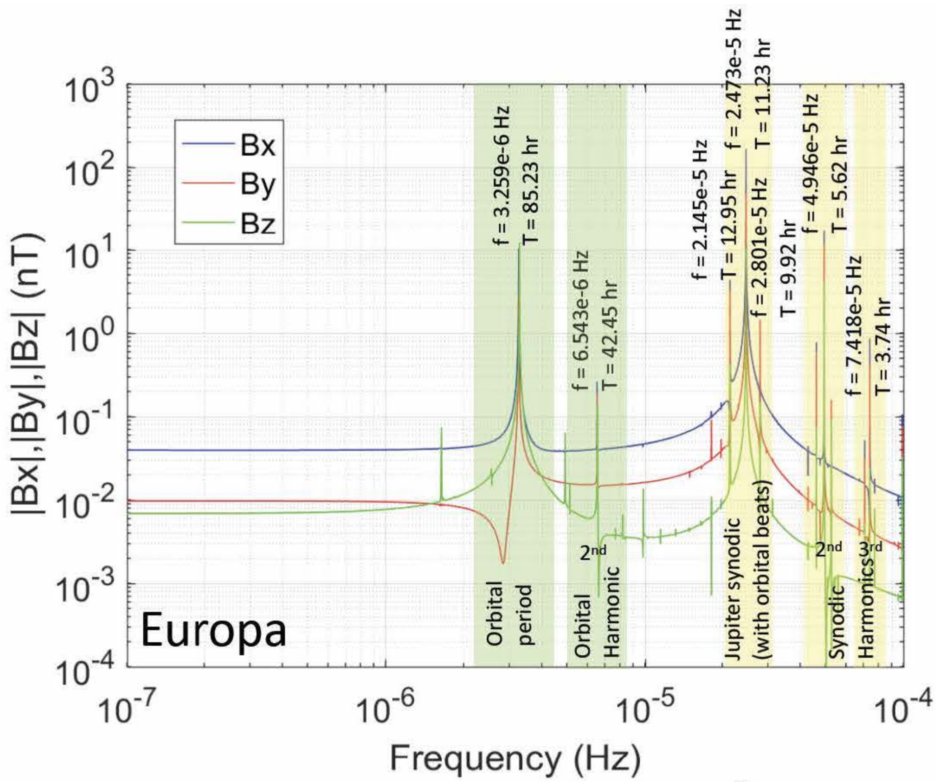


Figure 1: Europa: Variations in orbital parameters over time introduce magnetic fluctuations at multiple frequencies beyond the Jupiter rotation and satellite orbital frequencies. The different vector components contain unique information at multiple frequencies resulting from the harmonics and beats of the orbital and rotational oscillations.

harmonic series representation of the magnetic potential, which is a variant of Eq. 4:

$$\Phi[r,\theta,\phi] = R \sum_{n=1} \left(\frac{R}{r}\right)^{n+1} \sum_{m=0}^{n} P_{n,m}[\sin[\theta]] \;\left(g_{n,m}\cos[m\phi] + h_{n,m}\sin[m\phi]\right). \tag{49}$$

The magnetic field vector is the negative gradient of the scalar potential

$$B = -\nabla\Phi \tag{50}$$

$$= -\left\{\frac{\partial\Phi}{\partial x}, \frac{\partial\Phi}{\partial y}, \frac{\partial\Phi}{\partial z}\right\} \tag{51}$$

The mean radius is $R = 71,492$ km. The rotation rate of Jupiter, as defined in the System III longitude (Seidelmann & Divine, 1977), is $\omega = 870.536°$/day.

### 3.2 Electrical Conductivity in Adiabatic Galilean Oceans

Fluid temperature, pressure, and salt content determine the electrical conductivity of an aqueous solution, and thus dictate the magnetic induction responses of the Galilean oceans. The amplitude and phase of the magnetic fields induced by the oceans depend on the conductive properties of the oceans, which are influenced by the composition of the dissolved salts. With sufficient prior knowledge of the ice thickness and hints to the ocean's composition—for example, from geological and compositional measurements by the Europa Clipper (Buffington et al., 2017)—magnetic induction

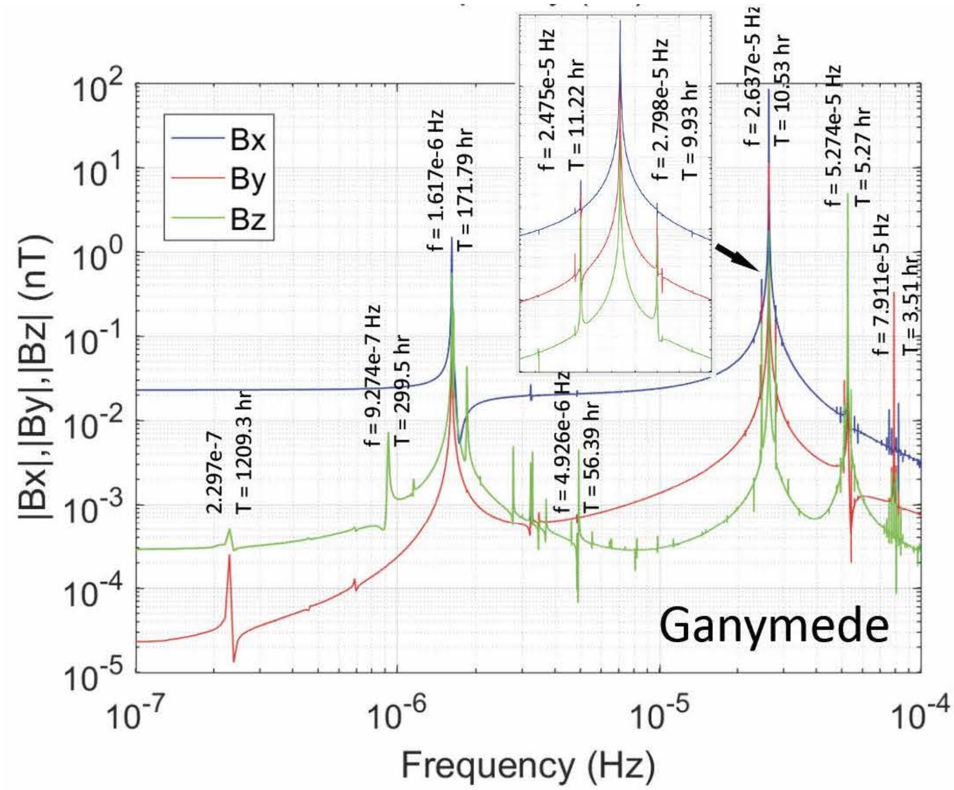


Figure 2: Ganymede: Variations in orbital parameters over time introduce magnetic fluctuations at multiple frequencies beyond the Jupiter rotation and satellite orbital frequencies.

studies can provide information on the amounts and compositions of the salts that link to global thermal and geochemical processes. On Europa, the flux of surface-generated oxygen to the ocean may have created oxidizing (acidic) conditions (Hand & Chyba, 2007; Pasek & Greenberg, 2012; Vance et al. , 2016) permitting the presence of dissolved $MgSO_4$ in addition to NaCl (Zolotov, 2008; Zolotov & Kargel, 2009).

Depth-dependent electrical conductivity can arise from melting or freezing at the ice–ocean interface, and from dissolution and precipitation within the ocean or at the water–rock interface. Even for oceans with uniform salinity, as is typically assumed, conductivity will increase with depth along the ocean's convective adiabatic profile because the greater temperature and pressure increase the electrical conductivity. Figure 4 depicts this variation for Europa and Ganymede, based on forward models of Vance et al. (2018) that use available thermodynamic and geophysical data to explore the influences of the ocean, rock layer, and any metallic core on the radial structures of known icy ocean worlds. For each ocean, we consider a nominal 10 wt% $MgSO_4$ salinity, as investigated in previous work. The published equation of state and electrical conductivity data are adequate for the pressures in the largest moon, Ganymede, up to 1.6 GPa (Vance et al., 2018). The pressure conditions in Europa's ocean are low enough ($<$ 200 MPa) that the equation of state for seawater (McDougall & Barker, 2011) provides plausible values of conductivity for salinity of 35 ppt less. For Europa, the respective radial models of electrical conductivity for oceans containing seawater and $MgSO_4$ are consistent with compositions linked to chemically reducing and oxidizing model oceans cited above.

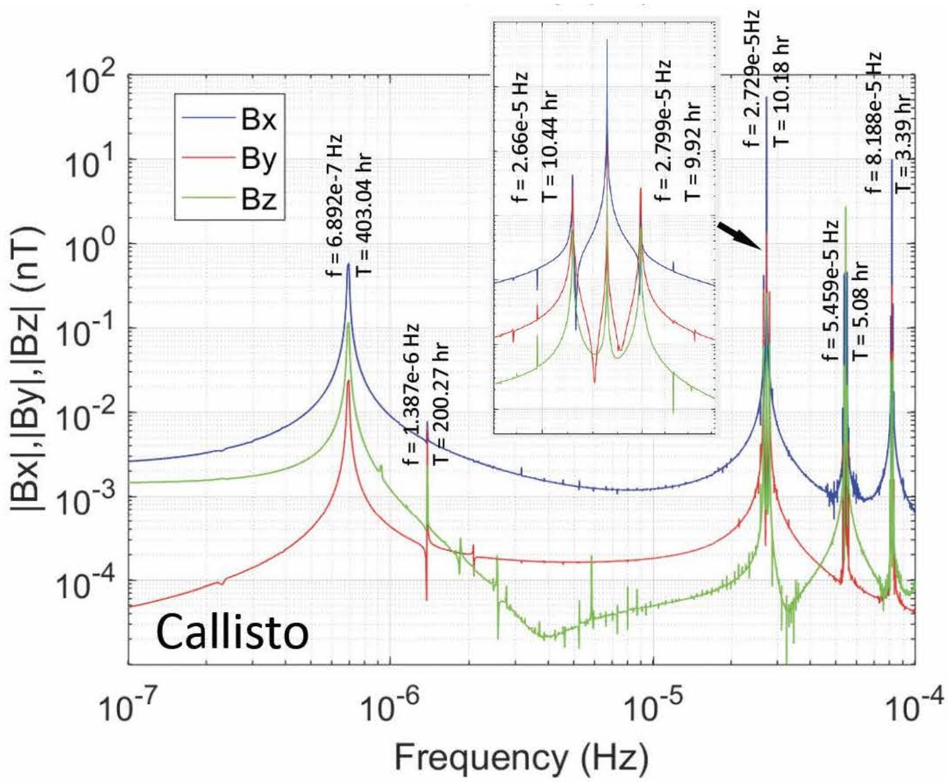


Figure 3: Callisto: Variations in orbital parameters over time introduce magnetic fluctuations at multiple frequencies beyond the Jupiter rotation and satellite orbital frequencies.

Radial conductivity profiles for Europa (Fig. 4; top) illustrate the coupling to temperature and composition. We consider ice thicknesses of 5 and 30 km (magenta and blue curves, respectively) as representative extremes. Seawater (dot–dashed lines), though less concentrated than the modeled composition of $MgSO_4$ (dashed lines), has a stronger melting point suppression, leading to an overall colder ocean for the same thickness of ice. Adiabats for pure water (solid lines) are shown for comparison. The lower temperature for seawater combines with the different electrical conductivity for the different dissolved ions to create distinct profiles unique to ocean composition and ice thickness (upper right).

Larger Ganymede (Fig. 4; bottom) also has distinct conductivity profiles for both ice thickness and ocean composition. They reveal an additional nuance to deep planetary oceans that can influence the induction response. Although electrical conductivity generally increases with depth, it begins to decrease at the greatest depths for the warm Ganymede ocean (right-most curve). This inflection occurs because the ocean achieves GPa+ pressures, at which the packing of water molecules begins to inhibit the charge exchange of the dissolved ions (Schmidt & Manning, 2017).

Dense brines may also reside at the base of the high-pressure ices on Ganymede, and even between them (Journaux, Daniel, Caracas, Montagnac, & Cardon, 2013; Journaux et al., 2017; S. Vance, Bouffard, Choukroun, & Sotin, 2014; Vance et al., 2018). Although more detailed modeling of the coupled geochemical and geodynamic regimes is needed, this scenario seems consistent with recent simulations of two-phase convection in high-pressure ices (Choblet, Tobie, Sotin, Kalousová, & Grasset, 2017). These simulations imply that fluids should occur at the water-rock interface through

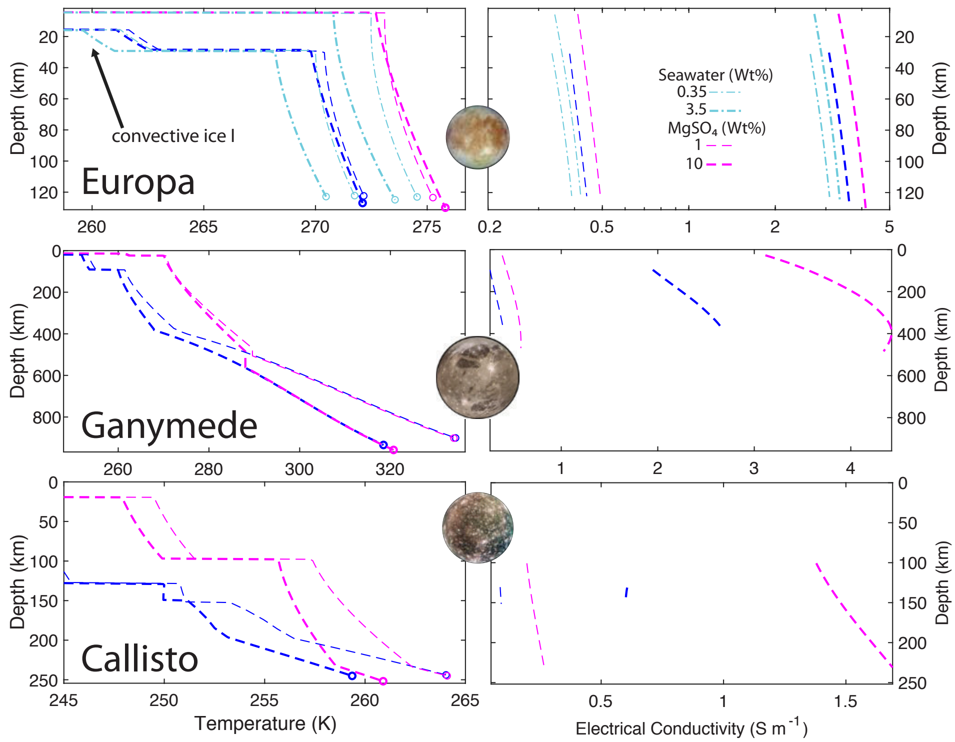


Figure 4: Adiabatic ocean temperature (left) and electrical conductivity (right). Convecting oceans with $MgSO_4$ (dashed lines) are warmer. Standard seawater (mostly NaCl; dot–dashed lines) creates colder oceans and lower electrical conductivities. Thicker ice (blue), corresponds to colder adiabatic profiles in the underlying oceans, which also lowers electrical conductivity. Open and closed circles correspond to the inferred depth to the upper boundary of the silicate layer for the saline and pure water oceans, respectively. Conductivities in the liquid regions are several orders of magnitude larger than in the ice and rock. Adapted from Vance et al. (2018).

long periods of the evolution of even of large icy world containing high-pressure ices. If such a fluid layer exists under the high-pressure ice, it will create an induction response at low frequencies, as discussed below.

### 3.3 Amplitude and Phase Lag of the Diffusive Response

The normalized surface induction response for Europa, Ganymede, and Callisto, shown in Fig. 5, are based on the adiabatic ocean electrical conductivity profiles shown in Fig. 4, assuming spherical symmetry (Section 2). Warmer and thus thicker oceans (magenta curves) have larger amplitude responses, corresponding to overall higher values of the conductance. The induction signatures for the adiabatic ocean profile are nearly equal to those of oceans with uniform conductivity equal to the mean of the adiabatic model (Section 2). These signatures differ, however, from those of an ocean with uniform conductivity based on the temperature and electrical conductivity at the ice–ocean interface.

For Europa, the induction signatures for modeled oxidized (10 wt% $MgSO_4$) and reduced (seawater) oceans are nearly identical in their amplitude responses. However, the two ocean models show phase separation of a few degrees at the orbital frequency of $3.6\times10^{-6}$ Hz (85.23 hr period).

Local enhancements in the ocean conductivity can have a discernible induction response. For Ganymede, we simulated a second ocean layer at the water–rock interface at a depth of 900 km, under 530 km of ice VI (Vance et al., 2018), modeled as a 10-km-thick high-conductivity region (20 S/m) corresponding to a nearly saturated $MgSO_4$ solution, consistent with (Hogenboom, Kargel, Ganasan, & Lee, 1995) and (Calvert, Cornelius, Griffiths, & Stock, 1958). The influence of such a layer (dotted lines in Fig. 5) is a ∼4% increase in the amplitude response and a corresponding ∼7% decrease in the phase response around $2.3\times10^{-7}$ Hz. A ∼1% decrease in amplitude is also seen at frequencies of $0.93\times10^{-6}$ Hz and $1.6\times10^{-6}$ Hz.

For Callisto, there is a small range of conditions under which oceans may be present. Salty oceans considered by Vance et al. (2018) have thicknesses of 20 and 132 km. For the thinner ocean, a 96 km layer of high-pressure ice underlies the ocean. The depicted state is likely transient, as ice III is buoyant in the modeled 10wt% $MgSO_4$ composition, and an upward snow effect should hasten the transfer of heat from the interior. Simulating a subsequent stage with ice III above the ocean awaits improved thermodynamic data, and will be discussed in future work. The present simulations illustrate the effect of the greater skin depth for the thicker and deeper ocean in terms of a higher amplitude response at lower frequencies and phase curve also shifted in the direction of lower frequencies.

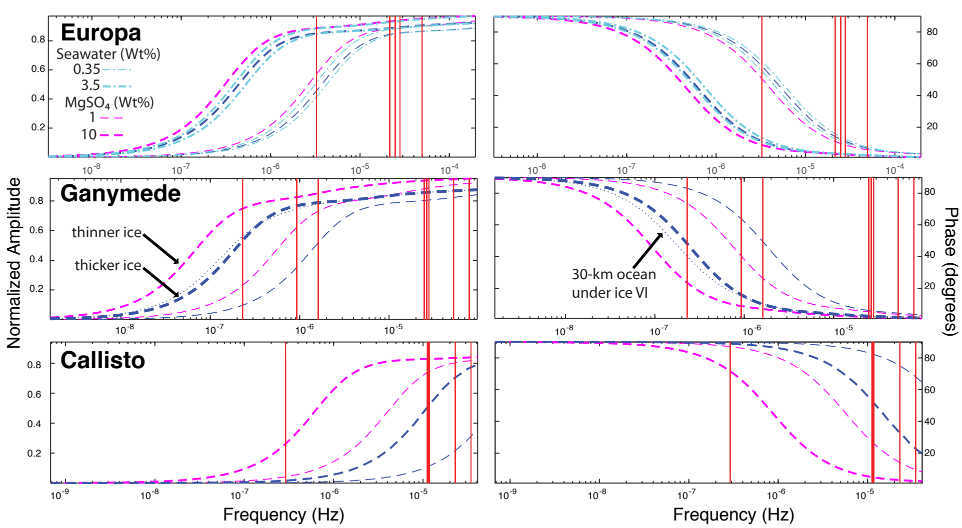


Figure 5: Normalized magnetic induction amplitudes (left) and phases (right) for the conductivity profiles in Fig. 4, at frequencies including the induction peaks noted in Fig. 1 (vertical red lines).

### 3.4 Mean Diffusive Response Relative to the Imposed Field

For the sake of comparing the passive induction responses of Europa, Ganymede and Callisto with fields induced by oceanic flows, we introduce the residual field, $B_R$. This quantity allows us to quickly examine the frequency dependent induction response for a given interior model, accounting for both the amplitude ($A$) and phase shift ($\phi$). For the geometric mean frequency components of Jupiter's field ($|B| = \sqrt{B_x^2 + B_y^2 + B_z^2}$), we define $B_R$ as

$$B_R = |B|(\cos\phi - A) \tag{52}$$

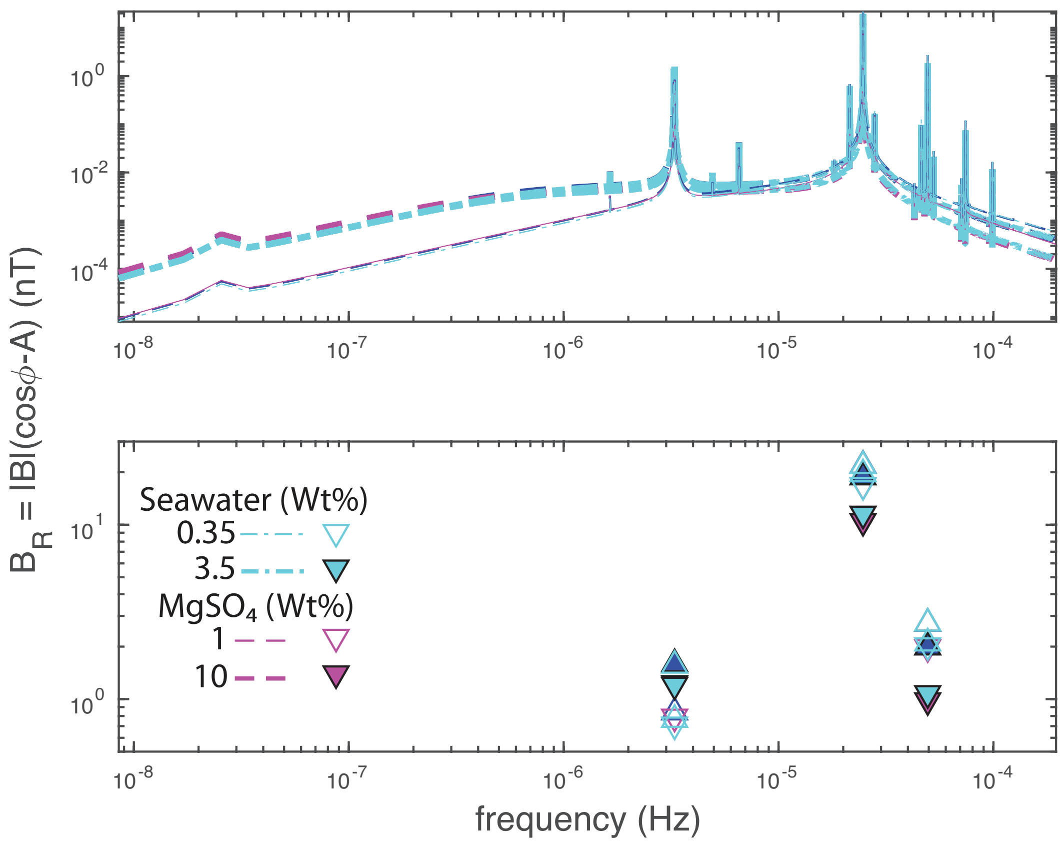


Figure 6: Europa:Residual field ($B_R$) of the diffusive induction response. Thick lines are higher salinities (10wt% and 3.5wt%, respectively) for oceans with aqueous $MgSO_4$ (magenta and blue −−) and seawater (cyan dash-dot). Thinner lines are for oceans with 10% of those concentrations. The lower pane shows responses at the strongest inducing frequencies in Figure 1. Filled symbols are for the higher concentrations. Upward triangles are for thicker ice (30 km) and downward triangles are for thinner ice (5 km).

More information can be gained by examining the directional components of Jupiter's field (Figure 1).

Figures 6, 7, and 8 show the spectra of residual fields for Europa, Ganymede, and Callisto, respectively. Subpanels in each figure isolate the peak responses at the main driving frequencies shown in Figure 1. Tables 1, 2, and 3 include the corresponding data. Figures S1-S3 illustrate possible errors arising from analyses assuming a uniform conductivity of the ocean. They plot the deviations (in percent) between the residual fields ($B_R$) of the adiabatic oceans (Figure 4) and the equivalent responses obtained by giving the oceans uniform conductivity, either as the equivalent mean value or the value at the top of the ocean (i.e. at the ice–ocean interface).

## 4 Magnetic Induction from Oceanic Fluid Flows

Another component of the induced magnetic response might occur in the icy Galilean satellites, arising not from Jupiter's changing magnetic field, but from charges moving with oceanic fluid flows. Such induced magnetic fields are typically neglected because they are expected to be relatively weak. On Earth, ocean currents induce fields on the order of 100 nT in a background field of about 40,000 nT; these fields

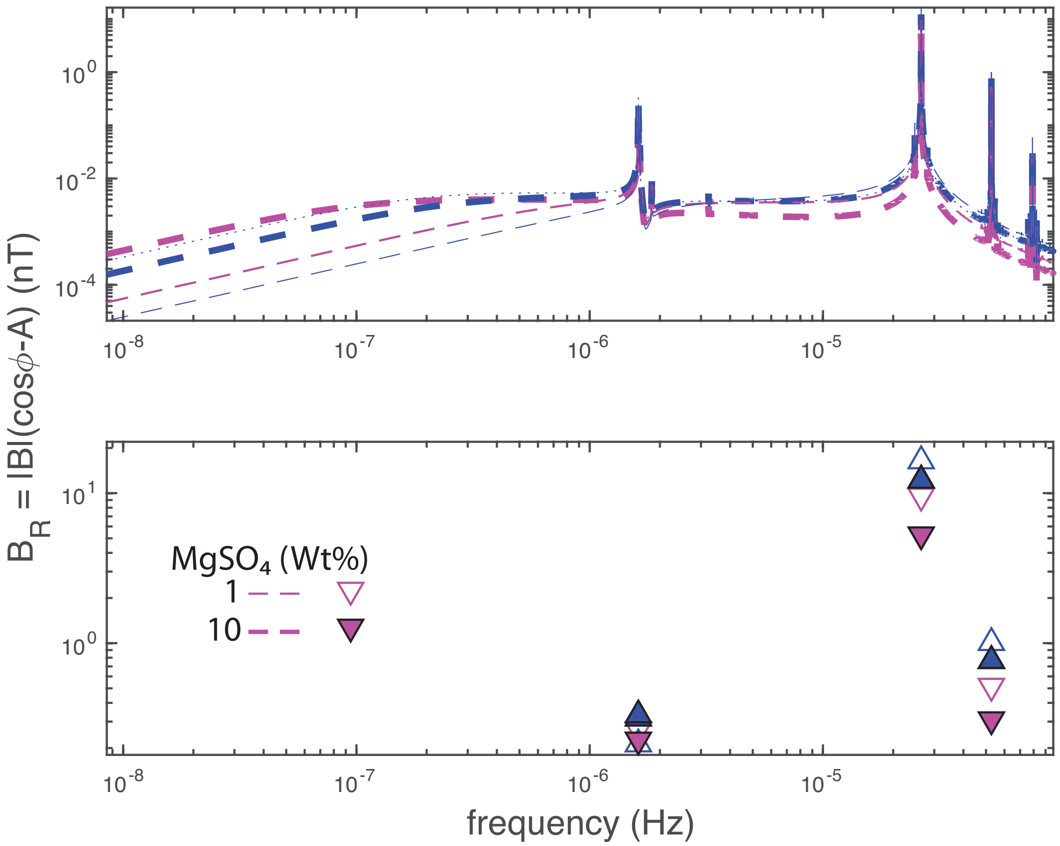


Figure 7: Ganymede: Residual field ($B_R$) of the diffusive induction response. Thick lines are higher salinities (10wt%) for oceans with aqueous $MgSO_4$ (magenta and blue −−). Thinner lines are for oceans with 1wt% $MgSO_4$. The dotted line is for the case with a 30-km-thick oceanic layer underneath the high-pressure ice. The lower pane shows responses at the strongest inducing frequencies in Figure 1. Filled symbols are for the higher concentrations. Upward triangles are for thicker ice ($\sim$ 100 km) and downward triangles are for thinner ice ($\sim$ 30 km)

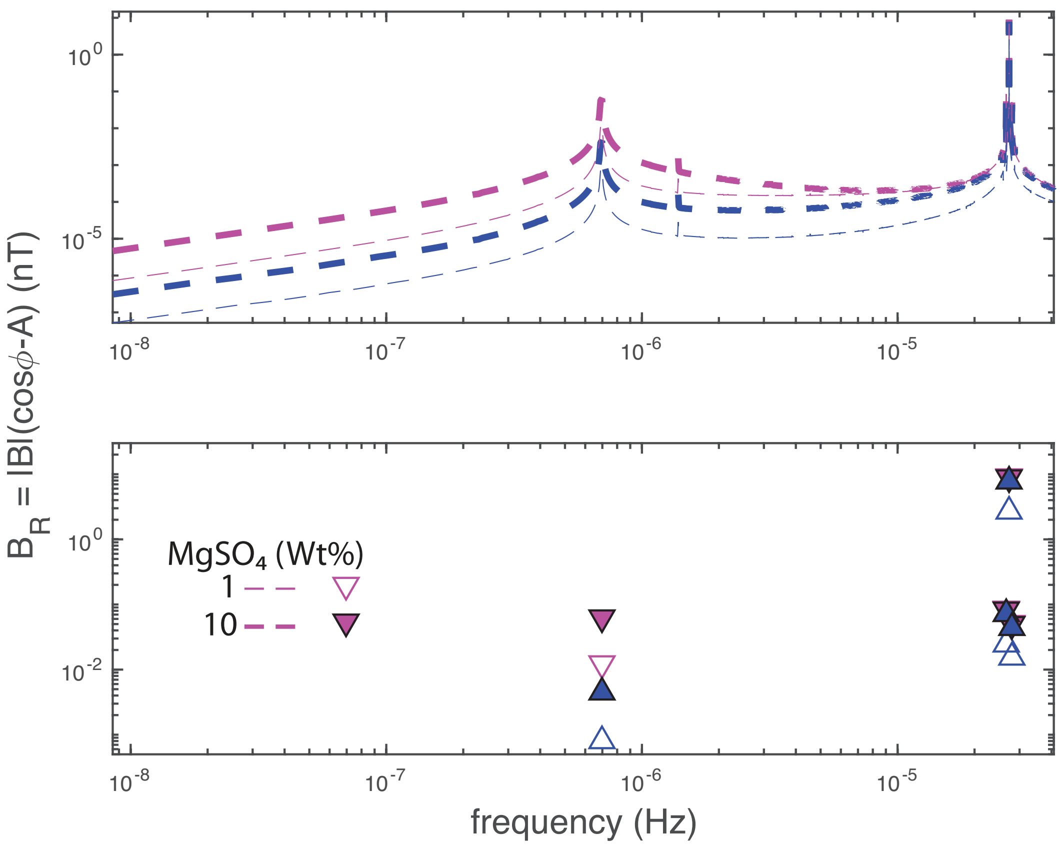


Figure 8: Callisto: Residual field ($B_R$) of the diffusive induction response. Thick lines are higher salinities (10wt%) for oceans with aqueous $MgSO_4$ (magenta and blue −−). Thinner lines are for oceans with 1wt% $MgSO_4$. The lower pane shows responses at the strongest inducing frequencies in Figure 1. Filled symbols are for the higher concentrations. Upward triangles are for thicker ice (∼ 130 km) and downward triangles are for thinner ice (∼ 100 km).

| | $T_b$ (K) | $T_{mean}$ (K) | $D_I$ (km) | $D_{ocean}$ (km) | $B_R$ (nT) | | |
|---|---|---|---|---|---|---|---|
| Europa | | | $f$ ($\times 10^{-6}$Hz) | | **3.25** | **24.73** | **49.46** |
| **$MgSO_4$ 1Wt%** | 270.4 | 271.5 | 31 | 120 | 0.841 | 21.862 | 2.715 |
| $<\sigma>= 0.4227$ S m$^{-1}$ | 270.4 | 271.5 | 31 | 120 | 0.823 | 21.417 | 2.654 |
| $\sigma_{top} = 0.3847$ S m$^{-1}$ | 270.4 | 271.5 | 31 | 120 | 0.769 | 21.304 | 2.650 |
| | 273.1 | 274.3 | 6 | 147 | 0.791 | 16.892 | 1.980 |
| $<\sigma>= 0.4640$ S m$^{-1}$ | 273.1 | 274.3 | 6 | 147 | 0.755 | 15.964 | 1.900 |
| $\sigma_{top} = 0.4107$ S m$^{-1}$ | 273.1 | 274.3 | 6 | 147 | 0.702 | 16.122 | 1.928 |
| **$MgSO_4$ 10Wt%** | 269.8 | 271.3 | 30 | 127 | 1.591 | 18.741 | 1.983 |
| $<\sigma>= 3.4478$ S m$^{-1}$ | 269.8 | 271.3 | 30 | 127 | 1.539 | 18.234 | 1.961 |
| $\sigma_{top} = 3.0763$ S m$^{-1}$ | 269.8 | 271.3 | 30 | 127 | 1.536 | 18.686 | 2.008 |
| | 272.7 | 274.5 | 5 | 154 | 1.233 | 10.477 | 0.982 |
| $<\sigma>= 3.8547$ S m$^{-1}$ | 272.7 | 274.5 | 5 | 154 | 1.167 | 9.800 | 0.935 |
| $\sigma_{top} = 3.3197$ S m$^{-1}$ | 272.7 | 274.5 | 5 | 154 | 1.173 | 10.634 | 1.000 |
| **Seawater 0.35165 Wt%** | 270.0 | 271.1 | 31 | 120 | 0.763 | 21.749 | 2.719 |
| $<\sigma>= 0.3734$ S m$^{-1}$ | 270.0 | 271.1 | 31 | 120 | 0.746 | 21.112 | 2.645 |
| $\sigma_{top} = 0.3339$ S m$^{-1}$ | 270.0 | 271.1 | 31 | 120 | 0.684 | 21.026 | 2.636 |
| | 272.5 | 273.6 | 6 | 146 | 0.712 | 16.850 | 2.029 |
| $<\sigma>= 0.3945$ S m$^{-1}$ | 272.5 | 273.6 | 6 | 146 | 0.678 | 16.046 | 1.926 |
| $\sigma_{top} = 0.3415$ S m$^{-1}$ | 272.5 | 273.6 | 6 | 146 | 0.614 | 15.921 | 1.947 |
| **Seawater 3.5165 Wt%** | 268.2 | 269.7 | 31 | 122 | 1.559 | 19.524 | 2.091 |
| $<\sigma>= 2.9548$ S m$^{-1}$ | 268.2 | 269.7 | 31 | 122 | 1.523 | 18.989 | 2.052 |
| $\sigma_{top} = 2.6476$ S m$^{-1}$ | 268.2 | 269.7 | 31 | 122 | 1.510 | 19.349 | 2.098 |
| | 270.8 | 272.3 | 5 | 148 | 1.205 | 11.538 | 1.079 |
| $<\sigma>= 3.1457$ S m$^{-1}$ | 270.8 | 272.3 | 5 | 148 | 1.138 | 10.805 | 1.024 |
| $\sigma_{top} = 2.7346$ S m$^{-1}$ | 270.8 | 272.3 | 5 | 148 | 1.140 | 11.350 | 1.068 |

Table 1: Europa: Residual fields ($B_R$) at the main inducing frequencies in Fig 1. For the different ocean compositions and thicknesses of the upper ice I lithosphere ($D_I$; Figure 4, the adiabatic response is given first, followed by the response for the ocean with uniform conductivity set to the mean of the adiabatic ocean ($\langle\sigma\rangle$), and then for the case with uniform conductivity set to the value at the ice-ocean interface ($\sigma_{top}$).

are observable by space-based magnetometers and have been used to monitor ocean currents (Constable & Constable, 2004; Tyler, Maus, & Luhr, 2003). If there are oceanic flow-driven induction signals present in the icy Galilean satellites, and if the spatial or temporal structures of these induction signals allow them to be separated from the contributions driven by variations in Jupiter's magnetic field, it would permit characterization of the ocean flows themselves as has been done for the Earth's ocean (e.g., Chave, 1983; Grayver et al., 2016; Minami, 2017; Tyler et al., 2003). Conversely, if such induced signals are present but the analysis does not accommodate that fact, then the recovered electrical conductivity estimates will be biased and inaccurate.

While Tyler (2011) discusses the possibility of magnetic remote sensing to detect resonant ocean tides on Europa in the limits of shallow water equations and thin-

| | $T_b$ (K) | $T_{mean}$ (K) | $D_I$ (km) | $D_{ocean}$ (km) | $B_R$ (nT) | | |
|---|---|---|---|---|---|---|---|
| Ganymede | | | $f$ ($\times 10^{-6}$Hz) | | **1.62** | **26.37** | **52.74** |
| **$MgSO_4$ 1Wt%** | 270.7 | 279.0 | 25 | 442 | 0.265 | 9.580 | 0.517 |
| $< \sigma >= 0.5166$ S m$^{-1}$ | 270.7 | 279.0 | 25 | 442 | 0.243 | 8.753 | 0.477 |
| $\sigma_{top} = 0.3890$ S m$^{-1}$ | 270.7 | 279.0 | 25 | 442 | 0.229 | 9.601 | 0.516 |
| | 261.5 | 266.1 | 93 | 272 | 0.212 | 16.389 | 1.007 |
| $< \sigma >= 0.3295$ S m$^{-1}$ | 261.5 | 266.1 | 93 | 272 | 0.203 | 15.626 | 0.967 |
| $\sigma_{top} = 0.2608$ S m$^{-1}$ | 261.5 | 266.1 | 93 | 272 | 0.175 | 15.906 | 0.999 |
| **$MgSO_4$ 10Wt%** | 270.1 | 278.2 | 28 | 455 | 0.226 | 5.286 | 0.309 |
| $< \sigma >= 4.0541$ S m$^{-1}$ | 270.1 | 278.2 | 28 | 455 | 0.209 | 4.991 | 0.290 |
| $\sigma_{top} = 3.1056$ S m$^{-1}$ | 270.1 | 278.2 | 28 | 455 | 0.226 | 5.325 | 0.306 |
| | 260.0 | 263.5 | 96 | 282 | 0.316 | 12.202 | 0.762 |
| $< \sigma >= 2.3476$ S m$^{-1}$ | 260.0 | 263.5 | 96 | 282 | 0.304 | 11.919 | 0.750 |
| $\sigma_{top} = 1.9483$ S m$^{-1}$ | 260.0 | 263.5 | 96 | 282 | 0.304 | 12.174 | 0.761 |
| 30 km 20 S m$^{-1}$ layer | 260.0 | 263.5 | 96 | 282 | 0.332 | 12.156 | 0.765 |

Table 2: Ganymede: Residual fields ($B_R$) at the main inducing frequencies in Fig 1. For the different ocean compositions and thicknesses of the upper ice I lithosphere ($D_I$; Figure 4, the adiabatic response is given first, followed by the response for the ocean with uniform conductivity set to the mean of the adiabatic ocean ($\langle\sigma\rangle$), and then for the case with uniform conductivity set to the value at the ice-ocean interface ($\sigma_{top}$).

shell electrodynamics, we are not aware of any studies that have examined magnetic induction signatures due to other flows or for other satellites (e.g., Gissinger & Petitdemange, 2019; Lemasquerier et al., 2017; Rovira-Navarro et al., 2019; Soderlund, 2019). Here, we focus on global fluid motions that may be driven by convection within the oceans of Europa, Ganymede, and Callisto, followed by estimates of the induction response that may be expected from these flows.

### 4.1 Oceanic Fluid Motions

The majority of ocean circulation studies have focused on hydrothermal plumes at Europa, with global models being developed relatively recently (, Soderlund et al.2014; Soderlund, 2019; Vance & Goodman, 2009b). Thermal convection in Europa's ocean is expected in order to efficiently transport heat from the deeper interior that arises primarily from radiogenic and tidal heating in the mantle. Moreover, by estimating the extent to which rotation will organize the convective flows, Europa's ocean was predicted to have quasi-three-dimensional turbulence (, Soderlund et al.2014; Soderlund, 2019). As shown in Figure 9, this turbulence generates three-jet zonal flows with retrograde (westward) flow at low latitudes, prograde (eastward) flow at high latitudes, and meridional overturning circulation. Upwelling at the equator and downwelling at middle to high latitudes from this circulation effectively forms a Hadley-like cell in each hemisphere.

Application of these calculations to Ganymede suggests convection is expected within its ocean as well and may have similar convective flows, although there is significantly more uncertainty in the predicted convective regime (Soderlund, 2019).

| | $T_b$ (K) | $T_{mean}$ (K) | $D_I$ (km) | $D_{ocean}$ (km) | $B_R$ (nT) | | | |
|---|---|---|---|---|---|---|---|---|
| Callisto | | | $f$ ($\times10^{-6}$Hz) | | **0.69** | **26.60** | **27.29** | **27.99** |
| **$MgSO_4$ 1Wt%** | 257.4 | 259.6 | 99 | 132 | 0.012 | 0.085 | 9.201 | 0.052 |
| $< \sigma >= 0.2307$ S m$^{-1}$ | 257.4 | 259.6 | 99 | 132 | 0.012 | 0.084 | 8.990 | 0.050 |
| $\sigma_{top} = 0.1965$ S m$^{-1}$ | 257.4 | 259.6 | 99 | 132 | 0.010 | 0.083 | 8.926 | 0.050 |
| | 250.8 | 250.9 | 128 | 21 | 0.001 | 0.024 | 2.688 | 0.015 |
| $< \sigma >= 0.0895$ S m$^{-1}$ | 250.8 | 250.9 | 128 | 21 | 0.001 | 0.025 | 2.740 | 0.016 |
| $\sigma_{top} = 0.0874$ S m$^{-1}$ | 250.8 | 250.9 | 128 | 21 | 0.001 | 0.024 | 2.689 | 0.015 |
| **$MgSO_4$ 10Wt%** | 255.7 | 256.9 | 99 | 130 | 0.063 | 0.083 | 8.875 | 0.050 |
| $< \sigma >= 1.5256$ S m$^{-1}$ | 255.7 | 256.9 | 99 | 130 | 0.062 | 0.082 | 8.763 | 0.049 |
| $\sigma_{top} = 1.3789$ S m$^{-1}$ | 255.7 | 256.9 | 99 | 130 | 0.058 | 0.082 | 8.822 | 0.049 |
| | 250.0 | 251.5 | 129 | 18 | 0.004 | 0.072 | 7.778 | 0.044 |
| $< \sigma >= 0.6025$ S m$^{-1}$ | 250.0 | 251.5 | 129 | 18 | 0.005 | 0.072 | 7.781 | 0.044 |
| $\sigma_{top} = 0.6062$ S m$^{-1}$ | 250.0 | 251.5 | 129 | 18 | 0.005 | 0.072 | 7.790 | 0.044 |

Table 3: Callisto: Residual fields ($B_R$) at the main inducing frequencies in Fig 1. For the different ocean compositions and thicknesses of the upper ice I lithosphere ($D_I$; Figure 4, the adiabatic response is given first, followed by the response for the ocean with uniform conductivity set to the mean of the adiabatic ocean ($\langle\sigma\rangle$), and then for the case with uniform conductivity set to the value at the ice-ocean interface ($\sigma_{top}$).

Convection in Callisto's potential ocean may be in the double-diffusive regime if the ocean's composition is nearly saturated (Vance et al., 2018). However, considering thermal convection as an upper bound, application of the scaling arguments in Soderlund (2019) to Callisto suggest similar ocean flows may be expected here as well.

The nominal ocean model shown in Figure 9 is, therefore, applicable to all three ocean worlds considered here. As described in Soderlund (2019), the model was carried out using the MagIC code (Wicht, 2002) with the SHTns library for the spherical harmonics transforms (Schaeffer, 2013) and is characterized by the following dimensionless input parameters: shell geometry $\chi = r_i/r_o = 0.9$, Prandtl number $Pr = \nu/\kappa = 1$, Ekman number $E = \nu/\Omega D^2 = 3.0 \times 10^{-4}$, and Rayleigh number $Ra = \alpha g \Delta T D^3/\nu\kappa$, where $r_i$ and $r_o$ are the inner and outer radii of the ocean, $D = r_o - r_i$ is ocean thickness, $\Omega$ is rotation rate, $\nu$ is kinematic viscosity, $\kappa$ is thermal diffusivity, $\alpha$ is thermal expansivity, $g$ is gravitational acceleration, and $\Delta T$ is superadiabatic temperature contrast. The boundaries are impenetrable, stress-free, and isothermal.

The model outputs, such as the velocity field, are also non-dimensional. For example, the Rossby number $Ro = U/\Omega D$ is the ratio of rotational $\Omega^{-1}$ to inertial $D/U$ timescales that allows the dimensional flow speeds to be determined: $U = \Omega D Ro$ using ocean thickness $D$ as the length scale and rotation rates $\Omega = [2.1 \times 10^{-5}, 1.0 \times 10^{-5}, 4.4 \times 10^{-6}]$ s$^{-1}$ for Europa, Ganymede, and Callisto, respectively. Following Table 1, Europan ocean thicknesses of $120-154$ km are considered. This range of liquid ocean thicknesses extends to $272-455$ km for Ganymede (Table 2) and $18-132$ km for Callisto (Table 3), given the larger uncertainties on their internal structures. We therefore assume the following mean parameter values in Figure 9: $D_{Europa} = 135$ km, $D_{Ganymede} = 360$ km, and $D_{Callisto} = 75$ km, with the ranges considered in Table 4. Flows are fastest for Ganymede and Europa, where the zonal jets can reach m/s speeds, the mean latitudinal flows have peak speeds of tens of cm/s, and the mean radial flows are $\sim 10$ cm/s.

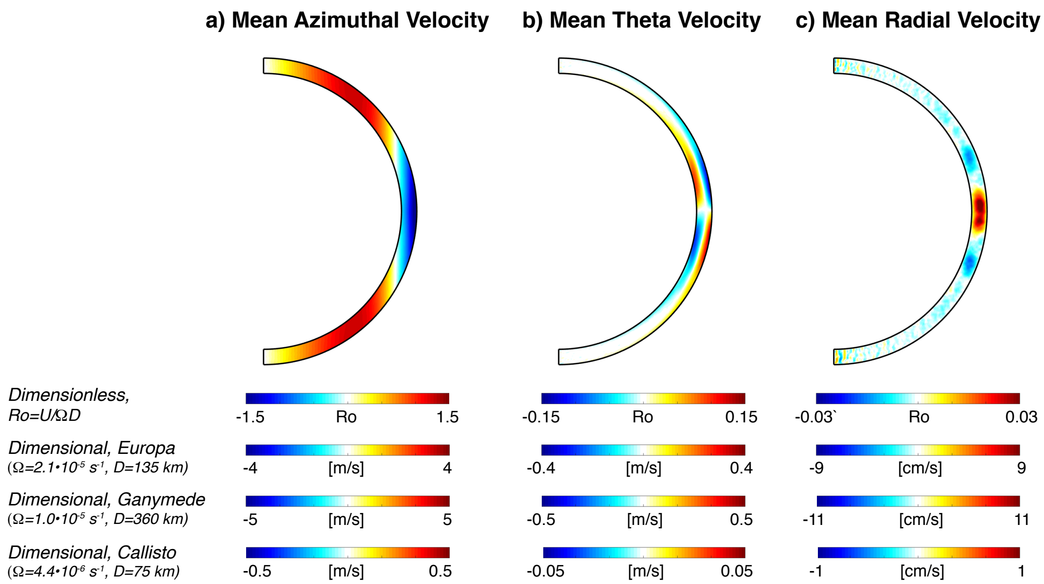


Figure 9: Mean flow fields in our nominal global ocean model from Soderlund (2019), averaged over 18 planetary rotations and all longitudes. **a)** Zonal velocity field where red denotes prograde flows and blue denotes retrograde flows. **b)** Theta velocity field where red denotes away from the north pole and blue denotes toward the north pole. **c)** Radial velocity field where red denotes upwelling flows and blue denotes downwelling flows.

### 4.2 Generation of Induced Magnetic Fields

The magnetic induction equation can be used to estimate the components of the magnetic field $\mathbf{B}$ induced by ocean currents with velocity $\mathbf{u}$ and those arising from changes in the externally imposed field:

$$\frac{\partial \mathbf{B}}{\partial t} = \nabla \times (\mathbf{u} \times \mathbf{B}) - \nabla \times (\eta \nabla \times \mathbf{B}) \tag{53}$$

where $\eta = (\mu_0 \sigma)^{-1}$ is the magnetic diffusivity. Here, the first term represents the evolution of the magnetic field, the second term represents magnetic induction, and the third term represents magnetic diffusion.

Neglecting variations in oceanic electrical conductivity with depth and assuming an incompressible fluid, equation 53 simplifies to

$$\frac{\partial \mathbf{B}}{\partial t} = (\mathbf{B} \cdot \nabla)\mathbf{u} - (\mathbf{u} \cdot \nabla)\mathbf{B} + \eta \nabla^2 \mathbf{B}, \tag{54}$$

after also expanding the induction term and utilizing $\nabla \cdot \mathbf{B} = 0$ and $\nabla \cdot \mathbf{u} = 0$. Let us decompose the total magnetic field into jovian imposed $\mathbf{F}$ and the satellite's induced $\mathbf{b}$ field components:

$$\mathbf{B} = \mathbf{F} + \mathbf{b} \tag{55}$$

with $|\mathbf{F}| \gg |\mathbf{b}|$. The induction equation then becomes

$$\frac{\partial \mathbf{b}}{\partial t} = -\frac{\partial \mathbf{F}}{\partial t} + (\mathbf{F} \cdot \nabla)\mathbf{u} - (\mathbf{u} \cdot \nabla)(\mathbf{F} + \mathbf{b}) + \eta \nabla^2 (\mathbf{F} + \mathbf{b}) \tag{56}$$

Here, the first term is the evolution of the induced magnetic field, the second term is induction due to variations in Jupiter's magnetic field, the third term is induction due to oceanic fluid motions, the fourth term is advection of the field by ocean flows, and the fifth and sixth terms are diffusion of the Jovian and induced fields.

Let us next assume that the Jovian field can be approximated by $\mathbf{F} = F_o\hat{\mathbf{z}}$, where $F_o$ is constant and homogeneous and $\hat{\mathbf{z}}$ is aligned with the rotation axis, in which case equation 56 further simplifies to:

$$\frac{\partial \mathbf{b}}{\partial t} = F_o\frac{\partial \mathbf{u}}{\partial z} - (\mathbf{u}\cdot\nabla)\mathbf{b} + \eta\nabla^2\mathbf{b}. \tag{57}$$

We will also focus on the quasi-steady induction signal generated by ocean flows rather than the rapidly varying contribution that could be difficult to distinguish from other magnetic field perturbations. Towards this end, the induced magnetic field and velocity fields are decomposed into mean and fluctuating components: $\mathbf{b} = \overline{\mathbf{b}} + \mathbf{b}'$ and $\mathbf{u} = \overline{\mathbf{u}} + \mathbf{u}'$. Inserting this into equation 57 and using Reynolds averaging yields

$$\frac{\partial \overline{\mathbf{b}}}{\partial t} = F_o\frac{\partial \overline{\mathbf{u}}}{\partial z} - (\overline{\mathbf{u}}\cdot\nabla)\overline{\mathbf{b}} - \overline{(\mathbf{u}'\cdot\nabla)\mathbf{b}'} + \eta\nabla^2\overline{\mathbf{b}}. \tag{58}$$

Next, we focus on the radial and latitudinal components because the zonal flow ($\overline{u_\phi}$) is nearly invariant in the z-direction (Figure 9a), noting also that azimuthally oriented (toroidal) magnetic fields would not be detectable by spacecraft:

$$\frac{\partial \overline{b_r}}{\partial t} = F_o\frac{\partial \overline{u_r}}{\partial z} - (\overline{\mathbf{u}}\cdot\nabla)\overline{b_r} - \overline{(\mathbf{u}'\cdot\nabla)b_r'} + \eta\nabla^2\overline{b_r} \tag{59}$$

$$\frac{\partial \overline{b_\theta}}{\partial t} = F_o\frac{\partial \overline{u_\theta}}{\partial z} - (\overline{\mathbf{u}}\cdot\nabla)\overline{b_\theta} - \overline{(\mathbf{u}'\cdot\nabla)b_\theta'} + \eta\nabla^2\overline{b_\theta} \tag{60}$$

Using simple scaling arguments, the second and third terms on the right sides are likely small compared to the first term since $|F| \gg |b|$ (assuming similar characteristic flow speeds and length scales) such that

$$\frac{\partial \overline{b_r}}{\partial t} \approx F_o\frac{\partial \overline{u_r}}{\partial z} + \eta\nabla^2\overline{b_r} \tag{61}$$

$$\frac{\partial \overline{b_\theta}}{\partial t} \approx F_o\frac{\partial \overline{u_\theta}}{\partial z} + \eta\nabla^2\overline{b_\theta}. \tag{62}$$

In the steady state limit and approximating the gradient length scales as $D$ and flow speeds as $U_r$ and $U_\theta$, the magnetic fields induced by ocean currents can be estimated as:

$$\frac{F_oU_r}{D} \sim \frac{\eta b_r}{D^2} \text{ such that } b_r \sim \frac{F_oU_rD}{\eta} = \mu_o\sigma DU_rF_o \tag{63}$$

$$\frac{F_oU_\theta}{D} \sim \frac{\eta b_\theta}{D^2} \text{ such that } b_\theta \sim \frac{F_oU_\theta D}{\eta} = \mu_o\sigma DU_\theta F_o. \tag{64}$$

The resulting induced magnetic fields are then stronger for larger electrical conductivities, ocean thicknesses, flow velocities, and satellites closer to the host planet, since $F_o$ decreases with distance.

Table 4 summarizes the ambient Jovian conditions at Europa, Ganymede, and Callisto as well as the relevant characteristics of their oceans, and the computed upper bounds on the induced magnetic field strengths. Here, we assume flow speeds typical of the global, steady overturning cells due to their temporal persistence and large spatial scale, which we hypothesize will produce the strongest induced magnetic signature that would be detectable at spacecraft altitudes. We find that the theta magnetic field components are larger than the radial components by roughly a factor of five, reaching

$\sim 200$ nT for both Europa and Ganymede (higher salt content, thinner ice shell models); estimates can be an order of magnitude weaker in the lower salt content, thicker ice shell models). The radial variations correspond to signals up to 33% (Ganymede) and 8% (Europa) of the ambient Jovian field, which could be detectable with future missions. The signature at Callisto is small ($\lesssim 1$ nT). In addition, we predict the fields to be strongest near the equator where large vertical gradients in the convective flows exist (Figure 9b-c).

| | $\sigma$ [S/m] | $D$ [km] | $U_r$ [m/s] | $U_\theta$ [m/s] | $F_o$ [nT] | $b_r$ [nT] | $b_\theta$ [nT] |
|---|---|---|---|---|---|---|---|
| Europa | | | | | | | |
| $MgSO_4$ 1 Wt%, Thicker ice shell | 0.4 | 120 | 0.08 | 0.38 | 420 | 2 | 10 |
| $MgSO_4$ 1 Wt%, Thinner ice shell | 0.5 | 147 | 0.09 | 0.46 | 420 | 3 | 18 |
| $MgSO_4$ 10 Wt%, Thicker ice shell | 3.4 | 127 | 0.08 | 0.40 | 420 | 18 | 91 |
| $MgSO_4$ 10 Wt%, Thinner ice shell | 3.9 | 154 | 0.10 | 0.49 | 420 | 32 | 155 |
| Seawater 0.35 Wt%, Thicker ice shell | 0.4 | 120 | 0.08 | 0.38 | 420 | 2 | 10 |
| Seawater 0.35 Wt%, Thinner ice shell | 0.4 | 146 | 0.09 | 0.46 | 420 | 3 | 14 |
| Seawater 3.5 Wt%, Thicker ice shell | 3.0 | 122 | 0.08 | 0.38 | 420 | 15 | 73 |
| Seawater 3.5 Wt%, Thinner ice shell | 3.1 | 148 | 0.09 | 0.47 | 420 | 22 | 114 |
| Ganymede | | | | | | | |
| $MgSO_4$ 1 Wt%, Thicker ice shell | 0.3 | 272 | 0.08 | 0.41 | 120 | 1 | 5 |
| $MgSO_4$ 1 Wt%, Thinner ice shell | 0.5 | 442 | 0.13 | 0.66 | 120 | 4 | 22 |
| $MgSO_4$ 10 Wt%, Thicker ice shell | 2.3 | 282 | 0.08 | 0.42 | 120 | 8 | 41 |
| $MgSO_4$ 10 Wt%, Thinner ice shell | 4.1 | 455 | 0.14 | 0.68 | 120 | 39 | 191 |
| Callisto | | | | | | | |
| $MgSO_4$ 1 Wt%, Thicker ice shell | 0.09 | 21 | 0.003 | 0.01 | 35 | $\ll 1$ | $\ll 1$ |
| $MgSO_4$ 1 Wt%, Thinner ice shell | 0.2 | 132 | 0.02 | 0.09 | 35 | 0.02 | 0.1 |
| $MgSO_4$ 10 Wt%, Thicker ice shell | 0.6 | 18 | 0.002 | 0.01 | 35 | $\ll 1$ | $\ll 1$ |
| $MgSO_4$ 10 Wt%, Thinner ice shell | 1.5 | 130 | 0.02 | 0.09 | 35 | 0.2 | 0.8 |

Table 4: Assumed properties and resulting calculated upper bounds on the strengths of the magnetic fields induced by oceanic fluid flows. Ambient magnetic field strengths, $F_o$, from Showman and Malhotra (1999); radial and theta flow speeds, $U_r$ and $U_\theta$ with $U = \Omega D Ro$, from Figure 9; ocean thicknesses, $D$, from Vance et al. (2018); and electrical conductivity, $\sigma$, from Figure 4. These signals are anticipated to be largest near the equator where $U_\theta$ and $U_r$ are strongest, as indicated in Figure 9b-c.

The simplified approach shown above gives an order of magnitude estimate of the maximum induced field. Future work will assess the implications of these assumptions through more detailed calculations. For example, we have assumed a homogeneous and constant Jovian field; however, the magnetic environment throughout the orbit close in to Jupiter may be highly variable and the external field is affected by the presence of heavy ions and a variable magnetosphere dynamics throughout a single orbit (e.g., Schilling, Neubauer, & Saur, 2008). The temporal and spatial variation of the ambient field is expected to be significant and the influence of these variations on ocean flow-driven magnetic field signatures remains to be explored. Kinematic models that directly solve the coupled momentum and induction equations are also an exciting avenue to refine these estimates.

## 5 Discussion and Conclusions

The inverse problem of reconstructing the full induction response is complex and is discussed in detail in Cochrane, Murphy, and Raymond (2020). Here, we focus instead on how the adiababic conductivity profile of the ocean affects the induction response relative to the mean case that is usually considered in space physics analyses (e.g., Kivelson et al., 2000), and relative to the isothermal case often considered in analyses of interior structure (e.g., Schubert, Anderson, Spohn, & McKinnon, 2004).

Differences between the adiabatic and mean conductivity cases have less dependence on frequency (Tables 1-3 and Figures S1, S3, and S5). For Europa, the nominal oceans with ice shells 5- and 30-km thick have errors of about 6% and 3%, respectively, and amount to nearly a 1 nT difference for the largest signals that exceed 20 nT. For Ganymede, the nominal oceans with ice shells $\sim$25- and $\sim$100-km thick have errors of about 7% and 3%, and are also nearly 1 nT for the largest signals that exceed 10 nT. For Callisto, the induction response of the mean conductivity ocean for ice shells of $\sim$100- and $\sim$130-km thickness is within about 2% of the response for the adiabatic ocean, less than 0.3 nT for the largest signals that approach 10 nT.

The induction response of the adiabatic ocean differs from that of the equivalent ocean with the conductivity of fluid at the ice-ocean interface. The greater mismatch of conductivities of the lower part of the ocean causes large differences in amplitude and phase at lower frequencies (i.e. for larger skin depths). For Europa, this means that the lower-frequency mean-motion signal ($3.2\times10^{-6}$ Hz; Table 1) differs by more than 15% for the warmer lower-salinity oceans, or about 0.1 nT. For Ganymede, the differences at the mean-motion frequency ($1.62\times10^{-6}$ Hz; Table 2) can approach 25%, which amounts to 0.04 nT. For Callisto, the differences at the mean-motion frequency ($6.9\times10^{-7}$ Hz; Table 3) approach 20%, which amounts to only 2 pT for the small predicted residual field based on the mean field. By contrast, the higher-frequency diurnal signals differ by less than 5%.

Based on the circulation models and upper bound induced magnetic field estimates described in Section 4, flow-induced fields may be a prominent component of the magnetic fields measured in the low latitudes for Europa and Ganymede. The peak flow-induced magnitude is 30-40 nT (Table 4) compared with Jovian-induced residual fields of less than 20 nT for both Europa (Table 1) and Ganymede (Table 2).

### 5.1 Implications for future missions

The Europa Clipper mission will conduct multiple (>40) flybys of Europa, and will investigate its induction response with the goal of constraining the ocean conductivity to within $\pm0.5$ S m$^{-1}$ and ice thickness to within $\pm2$ km (Buffington et al., 2017). The flybys at high latitudes will allow the Europa Clipper investigation to isolate flow-induced fields from the diffusive response, and possibly to derive constraints on currents in the ocean. With independent constraints on ice thickness obtained from the Radar for Europa Assessment and Sounding: Ocean to Near-surface (REASON) and Europa Imaging System (EIS) investigations (Steinbrügge et al., 2018), it may be possible to constrain the ocean's temperature and thus the adiabatic structure for the best-fit ocean composition inferred from compositional investigations. The analyses provided here (Figure 6 and Table 1) indicate that a sensitivity of 1.5 nT is probably insufficient to distinguish between end-member $MgSO_4$ and NaCl oceans, but might be sufficient to distinguish between order-of-magnitude differences in salinity.

The JUpiter ICy moons Explorer (JUICE) will execute two Europa flybys and nine Callisto flybys, and will orbit Ganymede (Grasset et al., 2013). The magnetic field investigation seeks to determine the induction response to better than 0.1 nT. The Europa flybys might aid the Europa Clipper investigation in constraining the composition of the ocean. At Ganymede, the magnetic field investigation will not be sufficient to discern the presence of a basal liquid layer at the ice VI-rock interface. Although the ability to discern between ocean compositions could not be assessed owing to insufficient electrical conductivity data at high pressures, it seems likely that useful constraints could be derived based on the signal strengths at Ganymede, if laboratory-derived electrical conductivity data for relevant solutions under pressure became available. At Callisto, 0.1 nT accuracy may only allow sensing of the induction response to Jupiter's synodic field, which might be sufficient to infer the thickness and salinity of an ocean if adequate temporal coverage is obtained to confirm the phase of the response.

## Acknowledgments

Work by JPL co-authors was partially supported by the Jet Propulsion Laboratory, Caltech, and by the Icy Worlds node of NASA's Astrobiology Institute (13-13NAI7_2-0024). This work was partially supported by NASA's Europa Clipper project. Work by MJS was supported by the NASA Earth and Space Science Fellowship Program - Grant 80NSSC18K1236. Work by KMS was also supported by NASA Grant NNX14AR28G.

The Matlab scripts and associated data needed to compute the results shown here are currently being archived. The data and scripts for radial structure models and diffusive induction will be placed on github (https://github.com/vancesteven/PlanetProfile) and Zenodo.

The MagIC code is publicly available at the https://magic-sph.github.io/contents.html website. All global convection model data were first published in Soderlund et al. (2019) and are available therein.



## References

Acuna, M. H., & Ness, N. F. (1976, Jun). The main magnetic field of jupiter. *Journal of Geophysical Research*, *81*(16), 2917–2922. Retrieved from `http://dx.doi.org/10.1029/JA081i016p02917` doi: 10.1029/ja081i016p02917

Buffington, B., Lam, T., Campagnola, S., Ludwinski, J., Ferguson, E., Bradley, B., ... Siddique, F. (2017). Evolution of trajectory design requirements on NASA's planned Europa Clipper mission. *Proceedings of the 68th International Astronautical Congress (IAC)*(IAC-17-C1.7.8).

Calvert, R., Cornelius, J. A., Griffiths, V. S., & Stock, D. I. (1958). The determination of the electrical conductivities of some concentrated electrolyte solutions using a transformer bridge. *The Journal of Physical Chemistry*, *62*(1), 47–53.

Chave, A. D. (1983). On the theory of electromagnetic induction in the Earth by ocean currents. *J. Geophys. Res.*, *88*, 3531–3542.

Choblet, G., Tobie, G., Sotin, C., Kalousová, K., & Grasset, O. (2017, Mar). Heat transport in the high-pressure ice mantle of large icy moons. *Icarus*, *285*, 252–262. Retrieved from `http://dx.doi.org/10.1016/j.icarus.2016.12.002` doi: 10.1016/j.icarus.2016.12.002

Cochrane, C. J., Murphy, N., & Raymond, C. (2020). Multi-frequency amplitude and phase extraction of induced magnetic dipoles of icy planetary bodies: Application to Europa Clipper. *Journal of Geophysical Research-Planets*, *submitted*.

Connerney, J., Acuna, M., Ness, N., & Satoh, T. (1998). New models of Jupiter's magnetic field constrained by the Io flux tube footprint. *Journal of Geophysical Research: Space Physics*, *103*(A6), 11929–11939.

Connerney, J. E. P., Kotsiaros, S., Oliversen, R. J., Espley, J. R., Joergensen, J. L., Joergensen, P. S., ... et al. (2018, Mar). A new model of Jupiter's magnetic field from Juno's first nine orbits. *Geophysical Research Letters*, *45*(6), 2590–2596. Retrieved from http://dx.doi.org/10.1002/2018GL077312 doi: 10.1002/2018gl077312

Constable, S., & Constable, C. G. (2004). Observing geomagnetic induction in magnetic satellite measurements and associated implications for mantle conductivity. *Geochem. Geophys. Geosys.*, *5*, Q01006.

Gissinger, C., & Petitdemange, L. (2019). A magnetically driven equatorial jet in Europa's ocean. *Nature Astron.*, *1*.

Grasset, O., Dougherty, M., Coustenis, A., Bunce, E., Erd, C., Titov, D., ... others (2013). Jupiter icy moons explorer (juice): An esa mission to orbit ganymede and to characterise the jupiter system. *Planetary and Space Science*, *78*, 1–21.

Grayver, A. V., Schnepf, N. R., Kuvshinov, A. V., Sabaka, T. J., Manoj, C., & Olsen, N. (2016). Satellite tidal magnetic signals constrain oceanic lithosphere-asthenosphere boundary. *Science Adv.*, *2*(9), e1600798.

Hand, K., & Chyba, C. (2007). Empirical constraints on the salinity of the europan ocean and implications for a thin ice shell. *Icarus*, *189*(2), 424–438.

Hartkorn, O., & Saur, J. (2017, Nov). Induction signals from Callisto's ionosphere and their implications on a possible subsurface ocean. *Journal of Geophysical Research: Space Physics*, *122*(11), 11,677–11,697. Retrieved from http://dx.doi.org/10.1002/2017JA024269 doi: 10.1002/2017ja024269

Hogenboom, D. L., Kargel, J. S., Ganasan, J. P., & Lee, L. (1995, June). Magnesium sulfate-water to 400 MPa using a novel piezometer: Densities, phase equilibria, and planetological implications. *Icarus*, *115*(2), 258–277. Retrieved from http://www.Sciencedirect.com/Science/article/B6WGF-45NJJ40-14/2/5f176b700065df4efb2e1eba3abd3224

Journaux, B., Daniel, I., Caracas, R., Montagnac, G., & Cardon, H. (2013, Sep). Influence of NaCl on ice VI and ice VII melting curves up to 6GPa, implications for large icy moons. *Icarus*, *226*(1), 355–363. Retrieved from http://dx.doi.org/10.1016/j.icarus.2013.05.039 doi: 10.1016/j.icarus.2013.05.039

Journaux, B., Daniel, I., Petitgirard, S., Cardon, H., Perrillat, J.-P., Caracas, R., & Mezouar, M. (2017, Apr). Salt partitioning between water and high-pressure ices. implication for the dynamics and habitability of icy moons and water-rich planetary bodies. *Earth and Planetary Science Letters*, *463*, 36–47. Retrieved from http://dx.doi.org/10.1016/j.epsl.2017.01.017 doi: 10.1016/j.epsl.2017.01.017

Khurana, K., Kivelson, M., Hand, K., & Russell, C. (2009). Electromagnetic induction from Europa's ocean and the deep interior. *Europa, Edited by Robert T. Pappalardo, William B. McKinnon, Krishan K. Khurana; with the assistance of René Dotson with 85 collaborating authors. University of Arizona Press, Tucson, 2009. The University of Arizona space science series ISBN: 9780816528448, p. 571*, *1*, 571.

Khurana, K., Kivelson, M., Stevenson, D., Schubert, G., Russell, C., Walker, R., & Polanskey, C. (1998). Induced magnetic fields as evidence for subsurface oceans in Europa and Callisto. *Nature*, *395*(6704), 777–780.

Khurana, K. K. (1997, Jun). Euler potential models of Jupiter's magnetospheric field. *Journal of Geophysical Research: Space Physics*, *102*(A6), 11295–11306. Retrieved from http://dx.doi.org/10.1029/97JA00563 doi: 10.1029/97ja00563

Kivelson, M., Khurana, K., Russell, C., Volwerk, M., Walker, R., & Zimmer, C. (2000). Galileo magnetometer measurements: A stronger case for a subsurface ocean at Europa. *Science*, *289*, 1340–1343.

Lainey, V., Duriez, L., & Vienne, A. (2006). Synthetic representation of the Galilean satellites' orbital motions from L1 ephemerides. *A&A*, *456*, 783–788.

Lemasquerier, D., Grannan, A. M., Vidal, J., Cébron, D., Favier, B., Le Bars, M., & Aurnou, J. M. (2017). Libration-driven flows in ellipsoidal shells. *J. Geophys. Res. Planets*, *122*(9), 1926–1950.

Lieske, J. (1998). Galilean satellite ephemerides E5. *Astronomy and Astrophysics Supplement Series*, *129*(2), 205–217.

Liuzzo, L., Feyerabend, M., Simon, S., & Motschmann, U. (2015, Nov). The impact of Callisto's atmosphere on its plasma interaction with the jovian magnetosphere. *Journal of Geophysical Research: Space Physics*, *120*(11), 9401–9427. Retrieved from `http://dx.doi.org/10.1002/2015JA021792` doi: 10.1002/2015ja021792

McDougall, T. J., & Barker, P. M. (2011). Getting started with TEOS-10 and the Gibbs Seawater (GSW) oceanographic toolbox. *SCOR/IAPSO WG*, *127*, 1–28.

Minami, T. (2017). Motional induction by tsunamis and ocean tides: 10 years of progress. *Surv. Geophys.*, *38*, 1097–1132.

Pasek, M. A., & Greenberg, R. (2012). Acidification of Europa's subsurface ocean as a consequence of oxidant delivery. *Astrobiology*, *12*(2), 151–159.

Rovira-Navarro, M., Rieutord, M., Gerkema, T., Maas, L. R., van der Wal, W., & Vermeersen, B. (2019). Do tidally-generated inertial waves heat the subsurface oceans of Europa and Enceladus? *Icarus*, *321*, 126–140.

Saur, J., Neubauer, F. M., & Glassmeier, K.-H. (2009, Dec). Induced magnetic fields in solar system bodies. *Space Science Reviews*, *152*(1-4), 391–421. Retrieved from `http://dx.doi.org/10.1007/s11214-009-9581-y` doi: 10.1007/s11214-009-9581-y

Saur, J., Strobel, D. F., & Neubauer, F. M. (1998, Aug). Interaction of the jovian magnetosphere with europa: Constraints on the neutral atmosphere. *Journal of Geophysical Research: Planets*, *103*(E9), 19947–19962. Retrieved from `http://dx.doi.org/10.1029/97JE03556` doi: 10.1029/97je03556

Schaeffer, N. (2013). Efficient spherical harmonic transforms aimed at pseudospectral numerical simulations. *Geochem. Geophys. Geosy.*, *14*(3), 751–758.

Schilling, N., Neubauer, F., & Saur, J. (2008). Influence of the internally induced magnetic field on the plasma interaction of europa. *Journal of Geophysical Research: Space Physics*, *113*(A3).

Schilling, N., Neubauer, F. M., & Saur, J. (2007). Time-varying interaction of Europa with the jovian magnetosphere: Constraints on the conductivity of Europa's subsurface ocean. *Icarus*, *192*(1), 41–55.

Schmidt, C., & Manning, C. (2017). Pressure-induced ion pairing in $MgSO_4$ solutions: Implications for the oceans of icy worlds. *Geochemical Perspectives Letters*, *3*, 66-74.

Schubert, G., Anderson, J., Spohn, T., & McKinnon, W. (2004). Interior composition, structure and dynamics of the Galilean satellites. *Jupiter: The Planet, Satellites and Magnetosphere*, 281–306.

Seidelmann, P., & Divine, N. (1977). Evaluation of jupiter longitudes in system iii (1965). *Geophysical Research Letters*, *4*(2), 65–68.

Seufert, M., Saur, J., & Neubauer, F. M. (2011). Multi-frequency electromagnetic sounding of the Galilean moons. *Icarus*, *214*(2), 477–494.

Showman, A. P., & Malhotra, R. (1999). The galilean satellites. *Science*, *286*(5437), 77–84.

Soderlund, K., Schmidt, B., Wicht, J., & Blankenship, D. (2014). Ocean-driven heating of Europa's icy shell at low latitudes. *Nature Geoscience*, *7*(1), 16–19.

Soderlund, K. M. (2019). Ocean dynamics of outer solar system satellites. *Geophys. Res. Lett.*, https://doi.org/10.1029/2018GL081880.

Steinbrügge, G., Schroeder, D., Haynes, M., Hussmann, H., Grima, C., & Blankenship, D. (2018, Jan). Assessing the potential for measuring Europa's tidal Love number h2 using radar sounder and topographic imager data. *Earth and*

*Planetary Science Letters*, *482*, 334–341. Retrieved from http://dx.doi.org/10.1016/j.epsl.2017.11.028 doi: 10.1016/j.epsl.2017.11.028

Tyler, R. H. (2011). Magnetic remote sensing of Europa's ocean tides. *Icarus*, *211*, 906–908.

Tyler, R. H., Boyer, T. P., Minami, T., Zweng, M. M., & Reagan, J. R. (2017, Nov). Electrical conductivity of the global ocean. *Earth, Planets and Space*, *69*(1). Retrieved from http://dx.doi.org/10.1186/s40623-017-0739-7 doi: 10.1186/s40623-017-0739-7

Tyler, R. H., Maus, S., & Luhr, H. (2003). Satellite observations of magnetic fields due to ocean tidal flow. *Science*, *299*, 239–241.

Vance, S., Bouffard, M., Choukroun, M., & Sotin, C. (2014, Jun). Ganymedes internal structure including thermodynamics of magnesium sulfate oceans in contact with ice. *Planetary and Space Science*, *96*, 62–70. Retrieved from http://dx.doi.org/10.1016/j.pss.2014.03.011 doi: 10.1016/j.pss.2014.03.011

Vance, S., & Goodman, J. (2009a). Europa. In R. T. P. W. B. M. K. Khurana (Ed.), (p. 459-482). Arizona University Press.

Vance, S., & Goodman, J. C. (2009b). Oceanography of an ice-covered moon. In R. T. Pappalardo, W. B. McKinnon, & K. K. Khurana (Eds.), *Europa* (p. 459-482). Tucson: University of Arizona Press.

Vance, S. D., Hand, K. P., & Pappalardo, R. T. (2016, May). Geophysical controls of chemical disequilibria in Europa. *Geophysical Research Letters*, *43*(10), 4871–4879. Retrieved from http://dx.doi.org/10.1002/2016GL068547 doi: 10.1002/2016gl068547

Vance, S. D., Panning, M. P., Stähler, S., Cammarano, F., Bills, B. G., Tobie, G., ... et al. (2018, Nov). Geophysical investigations of habitability in ice-covered ocean worlds. *Journal of Geophysical Research: Planets*. Retrieved from http://dx.doi.org/10.1002/2017JE005341 doi: 10.1002/2017je005341

Wicht, J. (2002). Inner-core conductivity in numerical dynamo simulations. *Phys. Earth Planet. Int.*, *132*, 281–302.

Zimmer, C., Khurana, K. K., & Kivelson, M. G. (2000). Subsurface oceans on Europa and Callisto: Constraints from Galileo magnetometer observations. *Icarus*, *147*(2), 329–347.

Zolotov, M. (2008). Oceanic composition on europa: Constraints from mineral solubilities. In *Lunar and planetary institute science conference abstracts* (Vol. 39, p. 2349).

Zolotov, M. Y., & Kargel, J. (2009). On the chemical composition of Europa's icy shell, ocean, and underlying rocks. *Europa, edited by RT Pappalardo, WB McKinnon, and K. Khurana, University of Arizona Press, Tucson, AZ*, 431–458.

**Figure 1.**

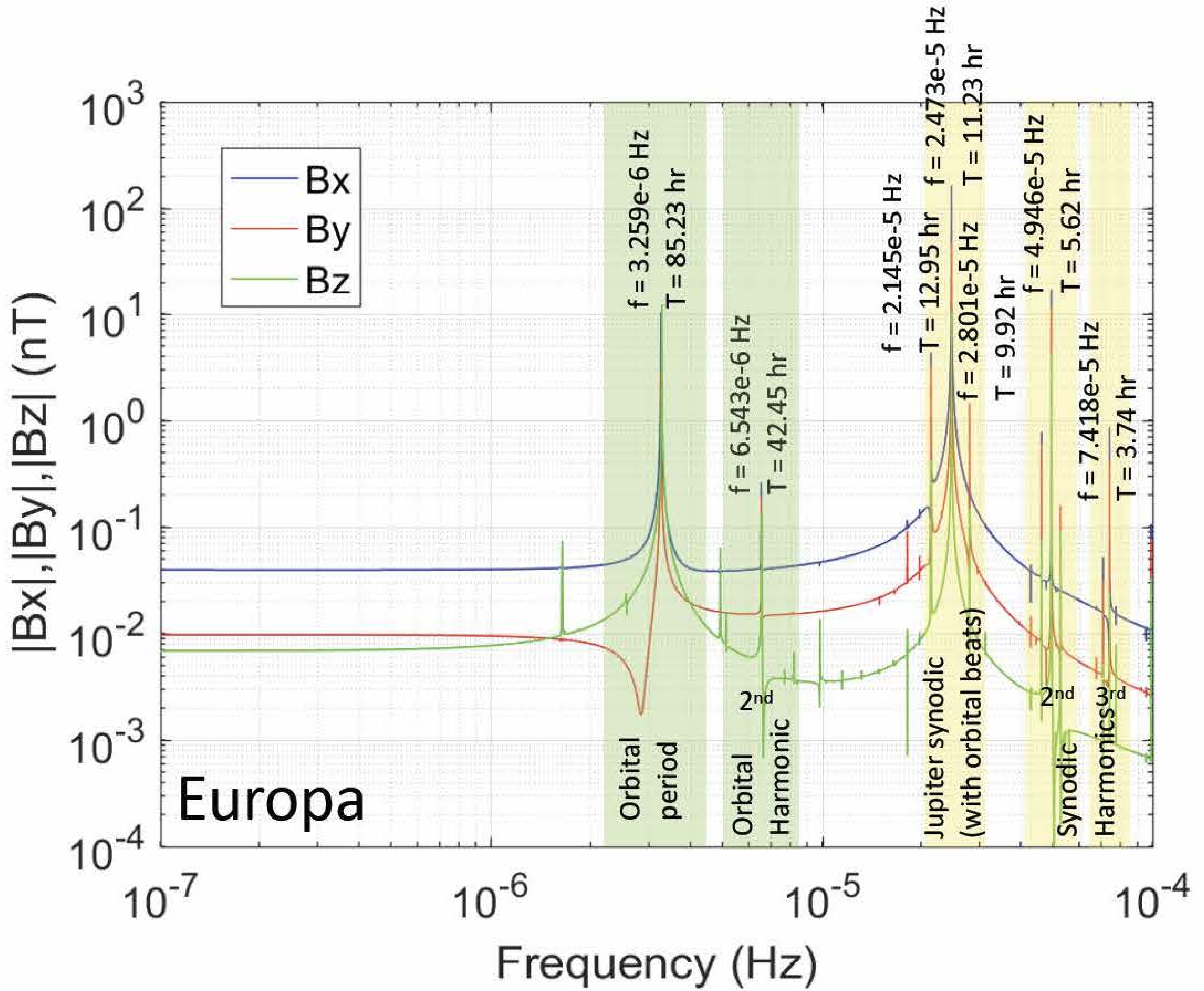
Bx
By
Bz
Europa
|Bx|,|By|,|Bz| (nT)
Frequency (Hz)
f = 3.259e-6 Hz
T = 85.23 hr
Orbital period
f = 6.543e-6 Hz
T = 42.45 hr
2nd
Orbital Harmonic
f = 2.145e-5 Hz
T = 12.95 hr
f = 2.473e-5 Hz
T = 11.23 hr
f = 2.801e-5 Hz
T = 9.92 hr
Jupiter synodic
(with orbital beats)
f = 4.946e-5 Hz
T = 5.62 hr
f = 7.418e-5 Hz
T = 3.74 hr
2nd
3rd
Synodic
Harmonics

**Figure 2.**

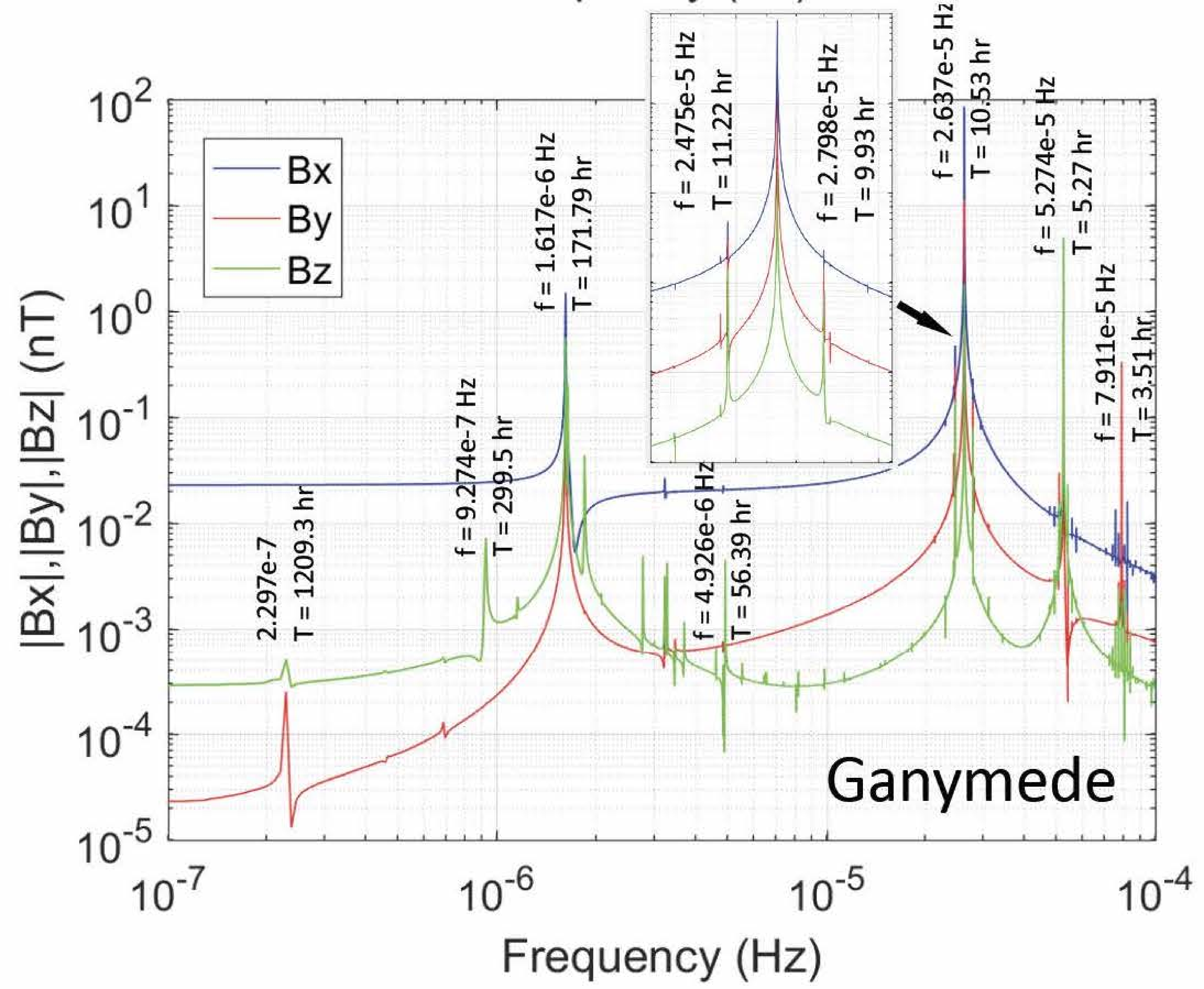

Bx
By
Bz
f = 1.617e-6 Hz
T = 171.79 hr
f = 9.274e-7 Hz
T = 299.5 hr
2.297e-7
T = 1209.3 hr
f = 4.926e-6 Hz
T = 56.39 hr
f = 2.475e-5 Hz
T = 11.22 hr
f = 2.798e-5 Hz
T = 9.93 hr
f = 2.637e-5 Hz
T = 10.53 hr
f = 5.274e-5 Hz
T = 5.27 hr
f = 7.911e-5 Hz
T = 3.51 hr
Ganymede
|Bx|,|By|,|Bz| (nT)
Frequency (Hz)

**Figure 3.**

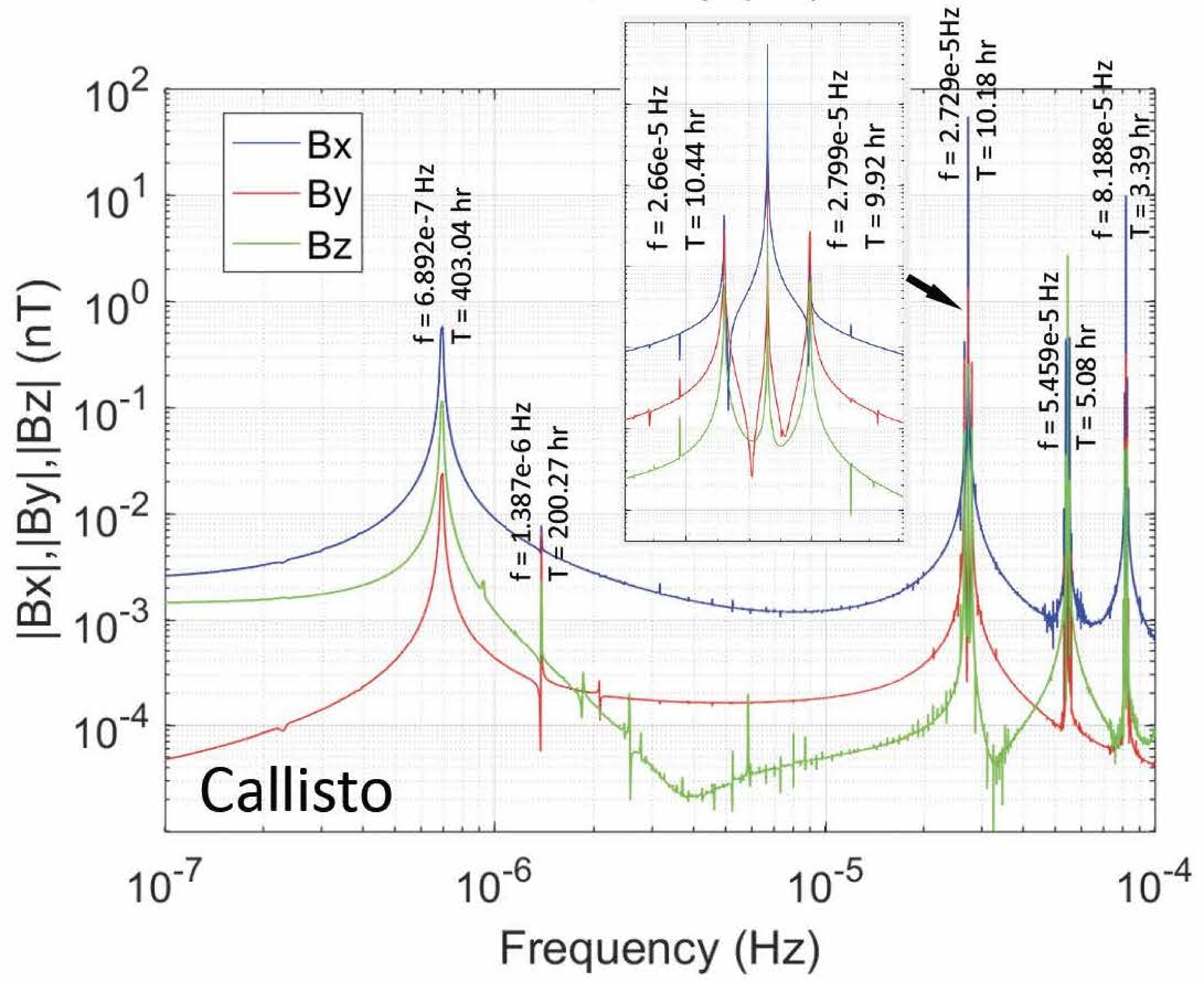

Bx
By
Bz
f = 6.892e-7 Hz
T = 403.04 hr
f = 1.387e-6 Hz
T = 200.27 hr
f = 2.66e-5 Hz
T = 10.44 hr
f = 2.799e-5 Hz
T = 9.92 hr
f = 2.729e-5Hz
T = 10.18 hr
f = 5.459e-5 Hz
T = 5.08 hr
f = 8.188e-5 Hz
T = 3.39 hr
Callisto
|Bx|,|By|,|Bz| (nT)
Frequency (Hz)

**Figure 4.**

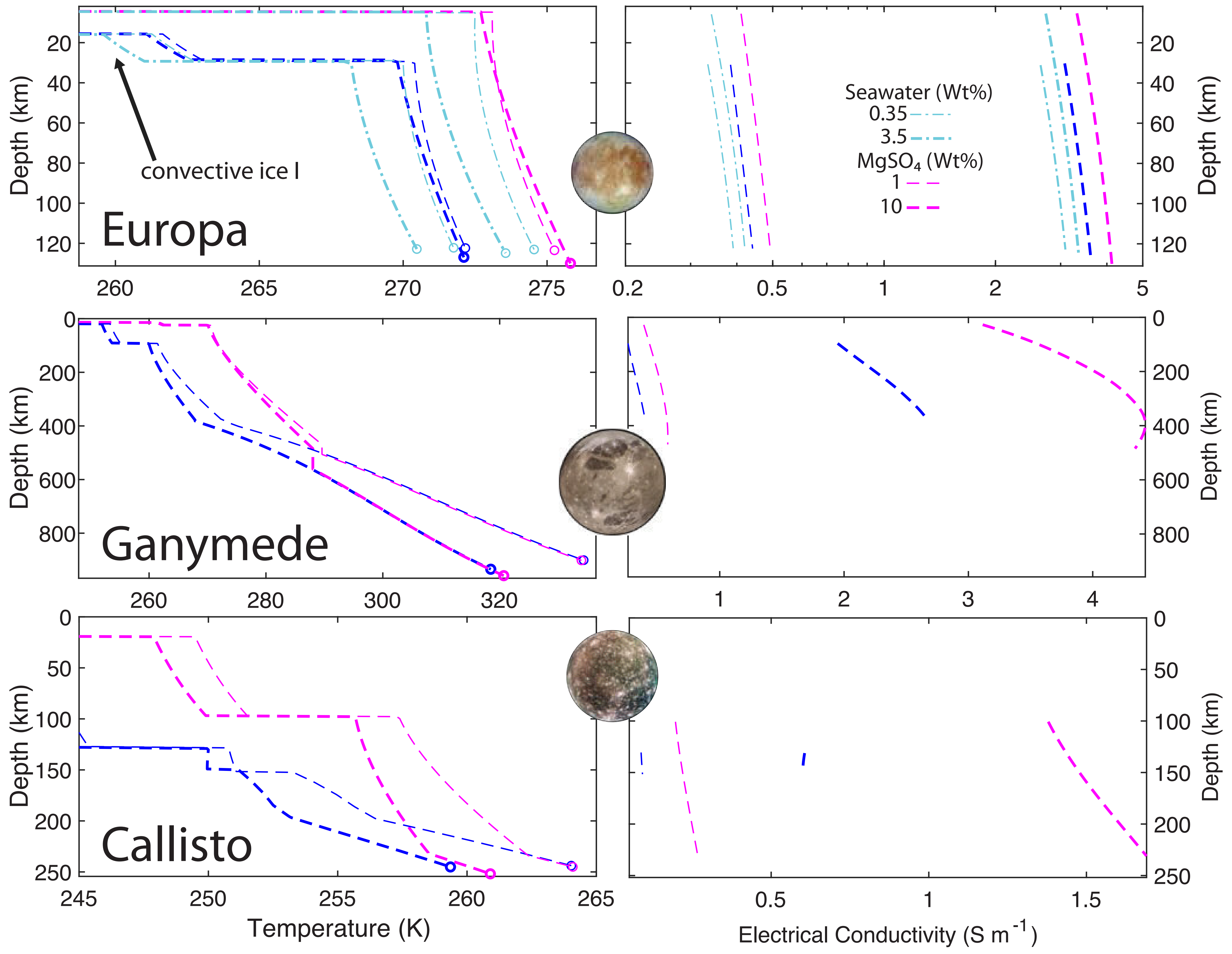

Europa
convective ice I
Seawater (Wt%)
0.35
3.5
$MgSO_4$ (Wt%)
1
10
Ganymede
Callisto
Depth (km)
Temperature (K)
Electrical Conductivity ($S\ m^{-1}$)

**Figure 5.**

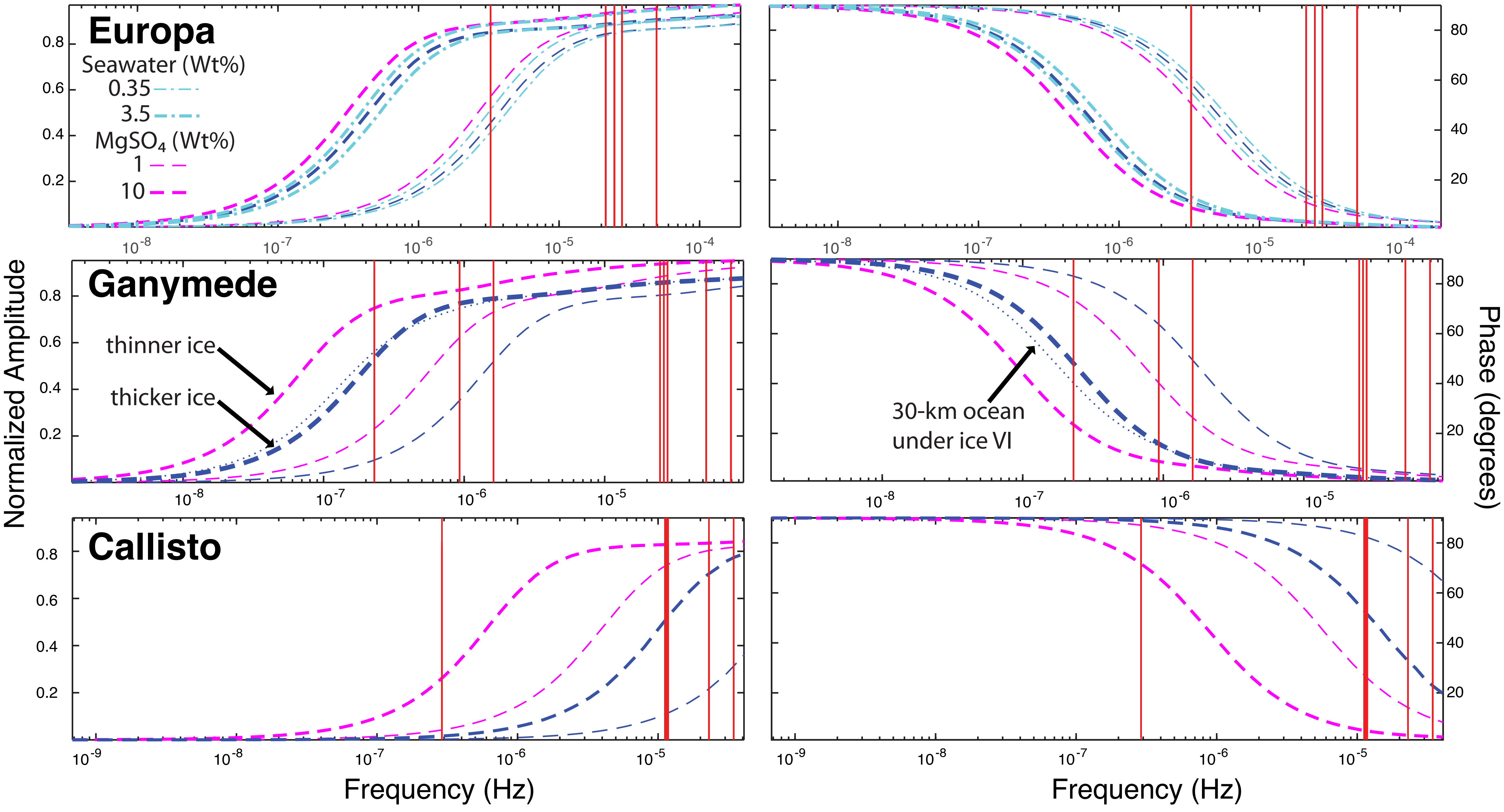

Europa
Seawater (Wt%)
0.35
3.5
MgSO4 (Wt%)
1
10
Ganymede
thinner ice
thicker ice
30-km ocean
under ice VI
Callisto
Normalized Amplitude
Phase (degrees)
Frequency (Hz)
Frequency (Hz)

**Figure 6.**

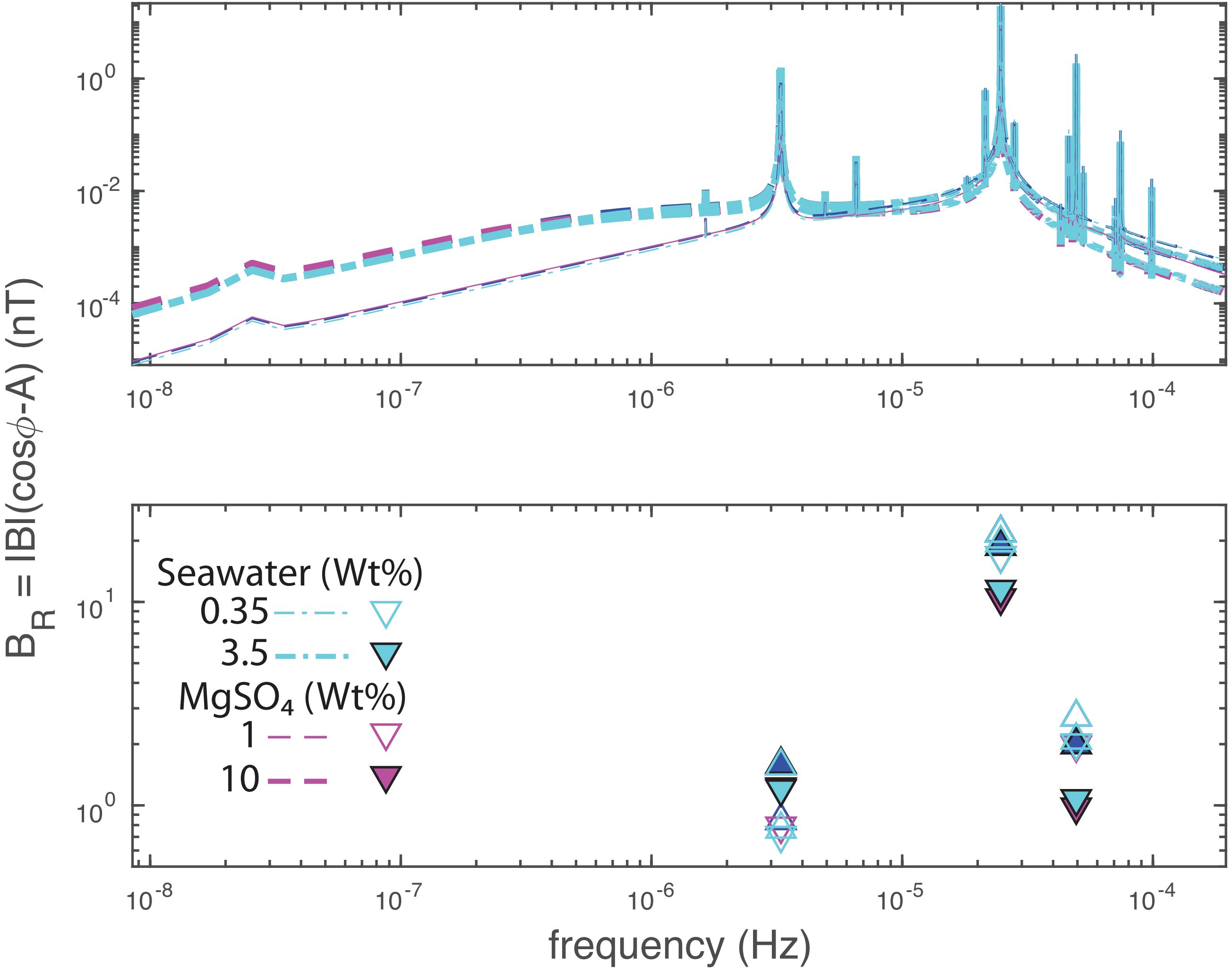

$B_R = |B|(\cos\phi - A)$ (nT)
$10^{0}$
$10^{-2}$
$10^{-4}$
$10^{-8}$
$10^{-7}$
$10^{-6}$
$10^{-5}$
$10^{-4}$
Seawater (Wt%)
0.35
3.5
$MgSO_4$ (Wt%)
1
10
$10^{1}$
$10^{0}$
frequency (Hz)

**Figure 8.**

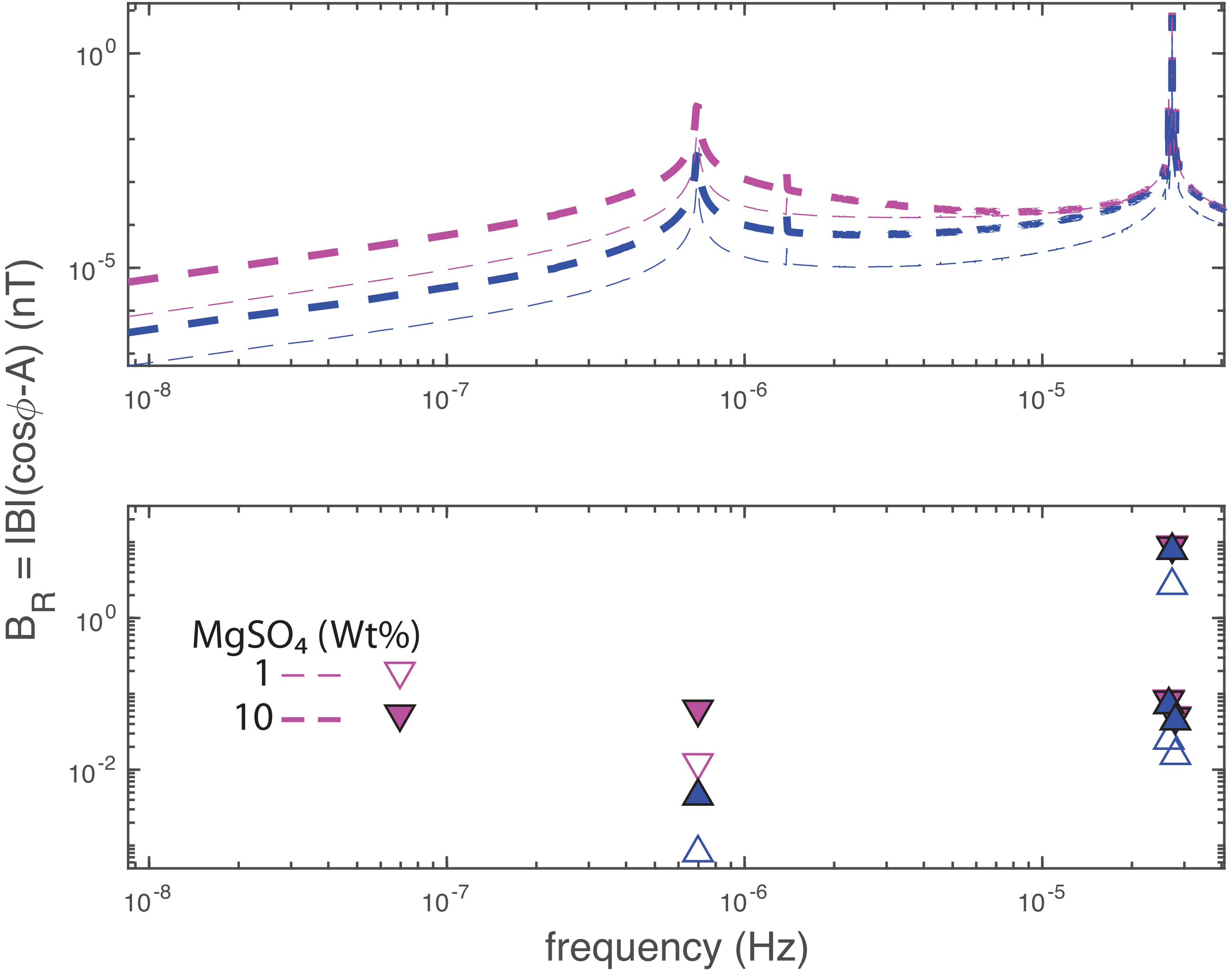

$B_R = |B|(\cos\phi - A)$ (nT)
$10^{0}$
$10^{-5}$
$10^{-8}$
$10^{-7}$
$10^{-6}$
$10^{-5}$
$MgSO_4$ (Wt%)
1
10
$10^{0}$
$10^{-2}$
$10^{-8}$
$10^{-7}$
$10^{-6}$
$10^{-5}$
frequency (Hz)

**Figure 7.**

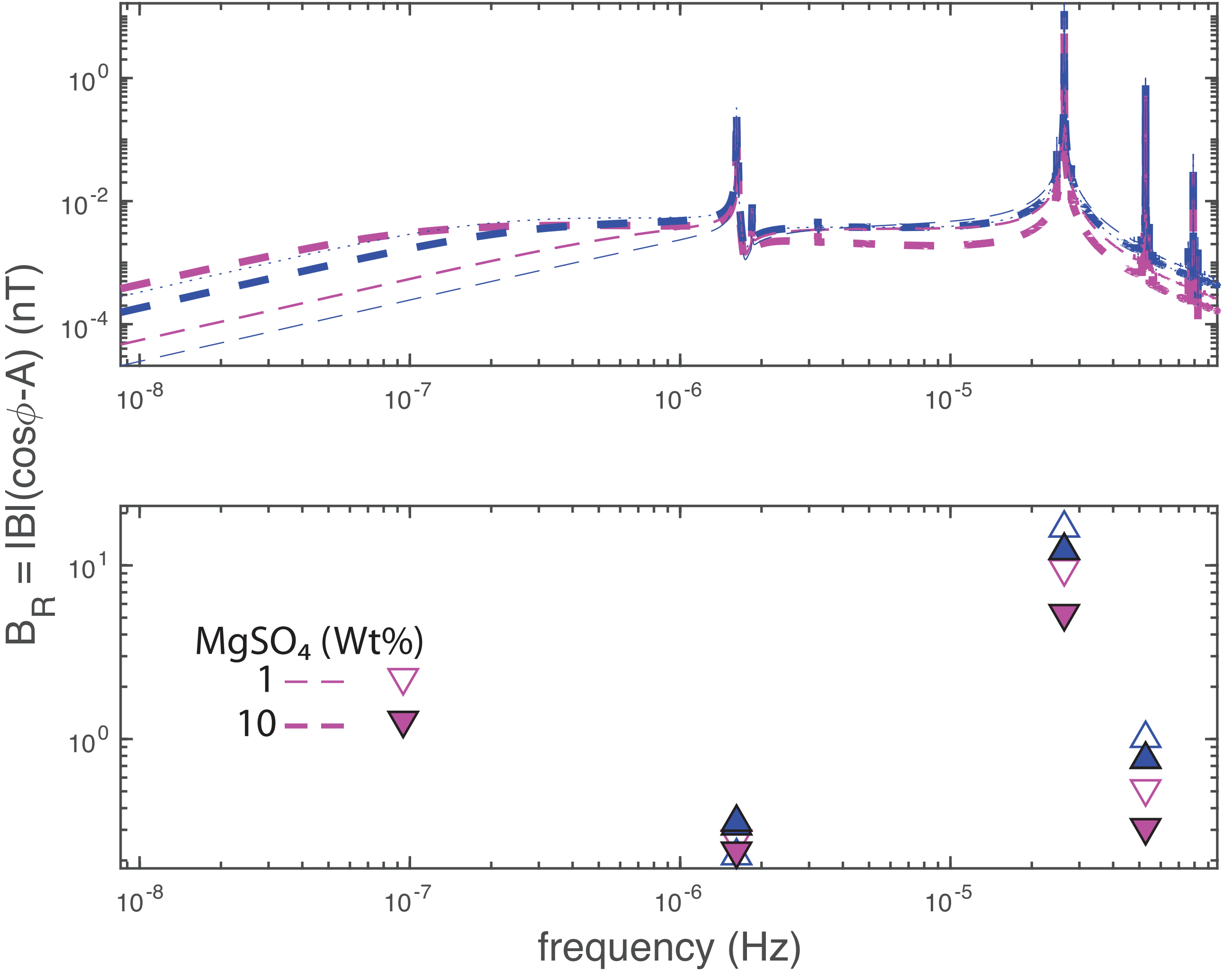

$B_R = |B|(\cos\phi - A)$ (nT)
$10^0$
$10^{-2}$
$10^{-4}$
$10^{-8}$
$10^{-7}$
$10^{-6}$
$10^{-5}$
$10^1$
$10^0$
$MgSO_4$ (Wt%)
1
10
$10^{-8}$
$10^{-7}$
$10^{-6}$
$10^{-5}$
frequency (Hz)

**Figure 8.**

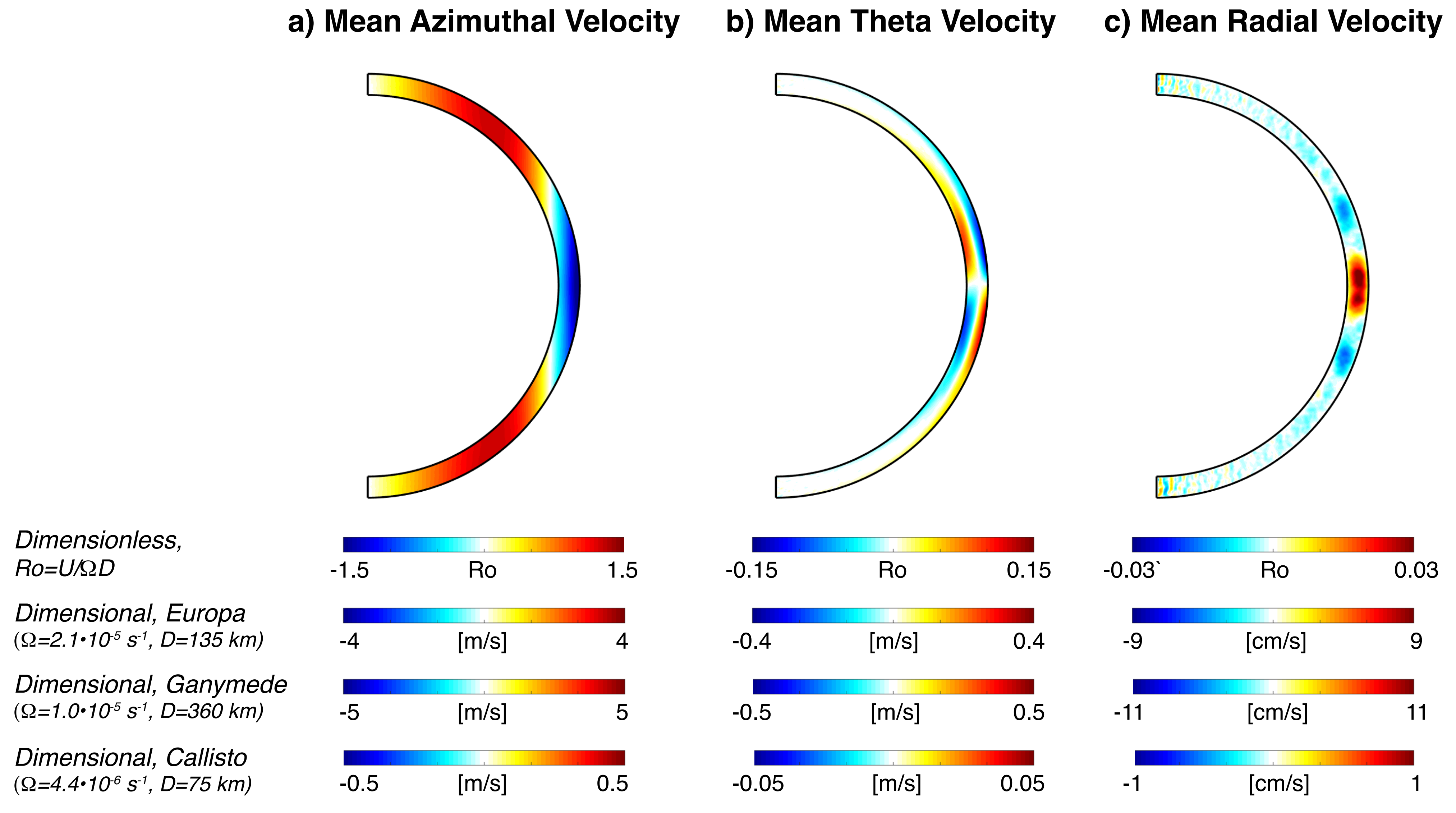
a) Mean Azimuthal Velocity
b) Mean Theta Velocity
c) Mean Radial Velocity
Dimensionless,
Ro=U/ΩD
-1.5 Ro 1.5
-0.15 Ro 0.15
-0.03` Ro 0.03
Dimensional, Europa
(Ω=2.1•10-5 s-1, D=135 km)
-4 [m/s] 4
-0.4 [m/s] 0.4
-9 [cm/s] 9
Dimensional, Ganymede
(Ω=1.0•10-5 s-1, D=360 km)
-5 [m/s] 5
-0.5 [m/s] 0.5
-11 [cm/s] 11
Dimensional, Callisto
(Ω=4.4•10-6 s-1, D=75 km)
-0.5 [m/s] 0.5
-0.05 [m/s] 0.05
-1 [cm/s] 1

# Magnetic Induction Responses of Jupiter's Ocean Moons Including Effects from Adiabatic Convection

**S. D. Vance[1], B. G. Bills[1], C. J. Cochrane[1], K. M. Soderlund[2], N. Gómez-Pérez[3], M. J. Styczinski[4], and C. Paty[5]**

[1]Jet Propulsion Laboratory, California Institute of Technology, Pasadena, USA
[2]Institute for Geophysics, John A. & Katherine G. Jackson School of Geosciences, The University of Texas at Austin, USA
[3]British Geological Survey, Edinburgh, UK
[4]Dept. of Physics, University of Washington, Seattle, USA
[5]Dept. of Earth Sciences, University of Oregon, Eugene, USA

**Key Points:**

- The signal from induction that accounts for adiabatic ocean temperatures is distinct from induction based on uniform conductivity
- Motional induction due to thermal convection in the satellite oceans may be significant
- Material properties and motional induction modeling are needed to obtain ocean composition from magnetic induction

Corresponding author: S. D. Vance, svance@jpl.caltech.edu

**Abstract**

Prior analyses of oceanic magnetic induction within Jupiter's large icy moons have assumed uniform electrical conductivity. However, the phase and amplitude responses of the induced fields will be influenced by the natural depth-dependence of the electrical conductivity. Here, we examine the amplitudes and phase delays for magnetic diffusion in modeled oceans of Europa, Ganymede, and Callisto. For spherically symmetric configurations, we consider thermodynamically consistent interior structures that include realistic electrical conductivity along the oceans' adiabatic temperature profiles. Conductances depend strongly on salinity, especially in the large moons. The induction responses of the adiabatic profiles differ from those of oceans with uniform conductivity set to values at the ice–ocean interface, or to the mean values of the adiabatic profile, by more than 10% for some signals. We also consider motionally induced magnetic fields generated by convective fluid motions within the oceans, which might optimistically be used to infer ocean flows or, pessimistically, act to bias the ocean conductivity inversions. Our upper-bound scaling estimates suggest this effect may be important at Europa and Ganymede, with a negligible contribution at Callisto. Based on end-member ocean compositions, we quantify the magnetic induction signals that might be used to infer the oxidation state of Europa's ocean and to investigate stable liquids under high-pressure ices in Ganymede and Callisto. Fully exploring this parameter space for the sake of planned missions requires thermodynamic and electrical conductivity measurements in fluids at low temperature and to high salinity and pressure as well as modeling of motional induction responses.

## 1 Introduction

The jovian system is of particular interest for studying magnetic induction in icy ocean worlds. Jupiter has a strong magnetic field whose dipole axis is tilted 9.6° with respect to its rotation axis (Acuna & Ness, 1976), while the orbits of the Galilean moons lie very nearly in the equatorial plane of Jupiter. This means that Jupiter's magnetic field varies in time at the orbital positions of the satellites. Also, the outer layers of the satellites themselves are believed to consist mainly of water ice at the surface, underlain by salty oceans. Brines are good conductors, while ice is a significant insulator.

Magnetic induction from Jupiter's diurnal signal sensed by the *Galileo* mission provides the most compelling direct observational evidence for the existence of oceans within Europa and Ganymede (Saur et al., 1998; Khurana et al., 1998; Kivelson et al., 2000; Schilling et al., 2007; Hand & Chyba, 2007; Khurana et al., 2009). The case has also been made for an induction response from an ocean in Callisto (Zimmer et al., 2000), but this interpretation is clouded by ionospheric interaction (Liuzzo et al., 2015; Hartkorn & Saur, 2017).

Longer-period signals penetrate more deeply, as penetration of the magnetic field into the interior is a diffusive process. It is convenient that the skin depths at the dominant periods of variation experienced by Europa, Ganymede, and Callisto are comparable to the expected ocean depths, which makes it possible to probe the properties of their oceans using magnetic induction (Saur et al., 2009). The spectrum of frequencies driving induced magnetic responses includes not just the orbits of the Galilean satellites and the rotation of Jupiter's tilted dipole field, but also their harmonics and natural oscillations (Seufert et al., 2011). Electrical conductivity structure within the subsurface oceans—for example, from convective adiabatic temperature gradients (Vance et al., 2018) and stratification (Vance & Goodman, 2009)—will affect the induction response at these frequencies.

Further variations in the magnetic fields arise from the motion of the moons about Jupiter. Perturbations to the orbits of the moons arise from multiple sources, including the oblate figure of Jupiter, gravitational interactions with the other satellites, and even from Saturn and the Sun (Lieske, 1998; Lainey et al., 2006). These subtle perturbations introduce additional frequencies of oscillation in the magnetic fields the bodies experience. These additional oscillations, in turn, induce magnetic fields that oscillate on the same time scales. A complete understanding of the dominant frequencies of oscillation is vital to a physically consistent interpretation of spacecraft measurements; for our analysis, we use the NAIF-produced SPICE kernels to obtain the most precise ephemeris data available as they include the orbital perturbations responsible for most magnetic oscillation for the bodies we study.

An additional induced magnetic response may occur in the icy Galilean satellites, arising not from Jupiter's changing magnetic field, but from motions of salty water within the oceans themselves. Such motionally induced magnetic fields are typically neglected because they are expected to be relatively weak. On Earth, ocean currents induce fields on the order of 100 nT in a background field of about 40,000 nT; these fields are observable by space-based magnetometers and have been used to monitor ocean currents (Constable & Constable, 2004; Tyler et al., 2003). If there are motional induction signals present in the icy Galilean satellites, and if the spatial or temporal structures of these induction signals allow them to be separated from the contributions driven by variations in the jovian magnetic field, it would permit characterization of the ocean flows themselves as has been done for the oceans of Earth (e.g., Chave, 1983; Tyler et al., 2003; Grayver et al., 2016; Minami, 2017). Conversely, if such induced signals are present but the analysis of spacecraft magnetic field measurements does not accommodate that fact, then the recovered electrical conductivity estimates may be biased and inaccurate.

Here, we examine the amplitudes and phase delays for magnetic diffusion in modeled oceans of Europa, Ganymede, and Callisto. For Europa, we focus on whether these responses might reveal not just the ocean's thickness and electrical conductivity, but also the speciation of dissolved salts in the ocean—–here either $MgSO_4$ or seawater dominated by NaCl. We restrict our analysis to spherically symmetric configurations, treating interior structures based on self-consistent thermodynamics, which account for variations in electrical conductivity with depth in convective oceans (Vance et al., 2018).

In addition, we consider the generation of motionally induced magnetic fields due to oceanic thermal convection and estimate upper-bound field amplitudes using a scaling analysis. Based on end-member ocean compositions (Zolotov, 2008; Zolotov & Kargel, 2009), we demonstrate the possibilities for using magnetic induction to infer the oxidation state of Europa's ocean and to identify stable liquid layers under high-pressure ices in Ganymede and Callisto.

In Section 2, we examine the diffusive induction response of Jupiter's ocean moons. We build on the prior work of Seufert et al. (2011) by including electrical conductivity profiles that follow the adiabatic profiles of pressure and temperature within the ocean of each moon. In Section 3, we describe possible ocean flows due to thermal convection and use a scaling relationship to estimate upper bounds for motionally induced magnetic field strengths. In Section 4, we discuss these results and describe the prospects for detecting signals from each. The Supplemental Material includes detailed derivations of the theoretical techniques we use to model the induced magnetic fields, as well as additional results for field components not covered in Sections 2–4.

## 2 Diffusive Induction in Jupiter's Ocean Moons

The complex response to the excitation field $\mathcal{A}_1^e$ describes the frequency-dependent, normalized amplitude $A = |\mathcal{A}_n^e|$ and phase delay $\phi = -\arg(\mathcal{A}_n^e)$ for a uniform excitation field from Jupiter (degree $n = 1$). We compute the magnetic induction amplitude and phase delay for a spherically symmetric system with multiple conducting layers. This complex response function is the same as employed by, e.g., Zimmer et al. (2000);

Khurana et al. (2002); Seufert et al. (2011), generalized to an arbitrary number of layers and any degree $n$ in the excitation field. A derivation for this solution was first described by Srivastava (1966). Our adapted version from Eckhardt (1963) is provided in the supplement, along with a description of the optimized numerical implementation used in this work. The analytical benchmark described in the supplement builds on recent work by Styczinski et al. (*in progress*) examining perturbations from spherical symmetry.

### 2.1 Spectral Content of the Imposed Magnetic Field Variations

Temporal variations in the magnetic field occur in the reference frames of Jupiter's satellites. Figure 1 shows time series spectra over the range of periods showing the strongest components for each of Europa, Ganymede, and Callisto, arising from their orbital and synodic periods, as well as beats and harmonics of these periods. Table 1 lists the three main periods (in hr) and the corresponding component fields (in nT). For these analyses, we use body-centric $\phi\Omega$ coordinates E$\phi\Omega$, G$\phi\Omega$, and C$\phi\Omega$ (e.g. "E-phi-O"; Khurana et al., 2009). In these coordinate systems, $\hat{x}$ is directed along the corotation direction, approximately along the orbital velocity vector, $\hat{y}$ is directed toward the jovian spin axis, approximately toward Jupiter's center of mass, and $\hat{z}$ is directed along the jovian spin axis in a right-handed sense. These coordinate systems are constantly rotating, and remain fixed to center of each satellite. Seufert et al. (2011) determined the time series spectra for the time-varying magnetic perturbations applied to each of the four Galilean moons based on the VIP4 model of Connerney et al. (1998) combined with the jovian current sheet model of Khurana (1997). In contrast, we use the JRM09 Jupiter field model accounting for Juno measurements (Connerney et al., 2018). Along with this, we use the current sheet model of Connerney et al. (1981) because the JRM09 model is derived using this current sheet model. Together, the latter two match the Juno measurements well. We compute a time series of the field at the orbital positions of the moons using the NAIF SPICE kernels and ten years of data sampled at a ten-minute cadence. To determine the primary periods relevant to the diffusive interaction with the satellites, we compute the Fourier transform of the entire data set.

We note that Seufert et al. (2011) also examined the time series spectra of magnetic perturbations from dynamic migration of the jovian magnetopause based on solar wind data from the Ulysses spacecraft, which we do not consider.

The temporal variations in imposed magnetic field at each satellite depend on the orbits of the satellites and the magnetic field of Jupiter. To find them, we compute Jupiter's magnetic field in a Jupiter-centered coordinate system from a spherical harmonic series representation of the magnetic potential (Parkinson, 1983):

$$\Phi(r,\theta,\phi,t) = R\sum_{n=1}\left(\frac{R}{r}\right)^{n+1}\sum_{m=0}^{n} S_{n,m}(\theta,\varphi)\mathrm{e}^{-i\omega t} \tag{1}$$

for Jupiter's rotation rate $\omega$ and $R$ the outer radius of the body. The internally generated magnetic field vector is the negative gradient of the scalar potential

$$\mathbf{B}_{\text{int,Jup}} = -\nabla\Phi \tag{2}$$

The external field including the current systems is

$$\mathbf{B}_{\text{external}} = \nabla\times\mathbf{A}(\rho',z')\mathrm{e}^{-i\omega t} \tag{3}$$

where $\mathbf{A}(\rho',z')$ is described by the current sheet model of Connerney et al. (1981), $\rho'$ and $z'$ are radial and axial coordinates in the magnetic equatorial cylindrical coordinate system, and $\omega$ is again Jupiter's rotation rate. The magnetic field applied to the Galilean moons is found by taking the sum of these

$$\mathbf{B}_o = \mathbf{B}_{\text{int,Jup}} + \mathbf{B}_{\text{external}} \tag{4}$$

Within the conducting portion of the satellites, the net magnetic field **B** must satisfy the Helmholtz equation

$$\nabla^2 \mathbf{B} = -k^2 \mathbf{B} \tag{5}$$

which is a diffusion equation for **B**. The wavenumber $k$ is a function of the material properties and the angular frequency of oscillation of **B** within the body (see Section S1):

$$k = \sqrt{i\omega_p \mu_0 \sigma} \tag{6}$$

All terms within **B** are proportional to an oscillation factor $e^{-i\omega_p t}$, where $\omega_p$ is the angular frequency of oscillation. Only the largest oscillation amplitudes induce significant diffusive responses.

The diffusive response may be expressed in terms of the normalized excitation amplitude

$$\mathcal{A}_n^e = \frac{(n+1)}{n}\frac{B_i}{B_e} \tag{7}$$

which is a complex quantity that has the desirable property of ranging from 0 for a non-conducting body to (1+0i) for a perfect conductor. $B_i$ and $B_e$ are magnetic potentials for the induced and excitation fields, respectively, outside the moon (see Section S1.1.2).

The magnetic field $\mathbf{B}_o$ applied to the Galilean moons is close to uniform across the body of each satellite, so it is customary to choose $n = 1$ in the excitation field. In this case, the potential $B_e$ is equal to the amplitude of oscillation of the applied field for a particular angular frequency $\omega_p$ and has units of nT. On the surface of the body, at the poles, the diffusive response field is directed opposite the applied field. It oscillates as

$$B_{\mathrm{dif},p}(t) = B_e \mathcal{A}_1^e e^{-i\omega_p t} \tag{8}$$

and it has the form of a dipole (see Section S1.3). The measured magnetic field is then the real part of the net field outside the moon

$$\mathbf{B}_{\mathrm{net}} = \mathbf{B}_o + \mathbf{B}_{\mathrm{dif}} \tag{9}$$

which includes sums over all $n$, $m$, and $p$. The motionally induced fields discussed in Section 3 add another term to Equation 9. For our full mathematical derivation, see Section S1.

Unique among the satellites in our solar system, Ganymede has an internally generated dynamo field (Kivelson et al., 2002). In the case of this satellite, the analysis of the diffusive field is no different because this intrinsic field does not vary with time in the frame of the body. As with the mean background field applied by Jupiter, the dynamo field from Ganymede simply presents a static offset to magnetometer measurements near the body, and does not appear in the Fourier analysis. The magnitude of this net background field, around 800 nT at Ganymede's surface, is about a factor of two larger than that experienced by Europa (Zimmer et al., 2000) and thus does not present significant additional challenges to measurement precision scaling.

### 2.2 Parameter Space of the Diffusive Induction Response

A continuous parameter space of ocean thickness and conductivity has been explored previously for three-layer models consisting of a non-conducting mantle (and core), salty ocean, and non-conducting ice (Zimmer et al., 2000; Khurana et al., 2002) and for a five-layer model that adds an ionosphere and metallic core (Schilling, 2006). More recent work by Seufert et al. (2011) has further examined the influence of a metallic core and an ionosphere. No prior work has required the self-consistency among the ocean temperature and density, composition, ice and ocean thickness, etc., that are the focus of this paper. Prior work exploring the parameter space of ocean thickness and conductivity is useful

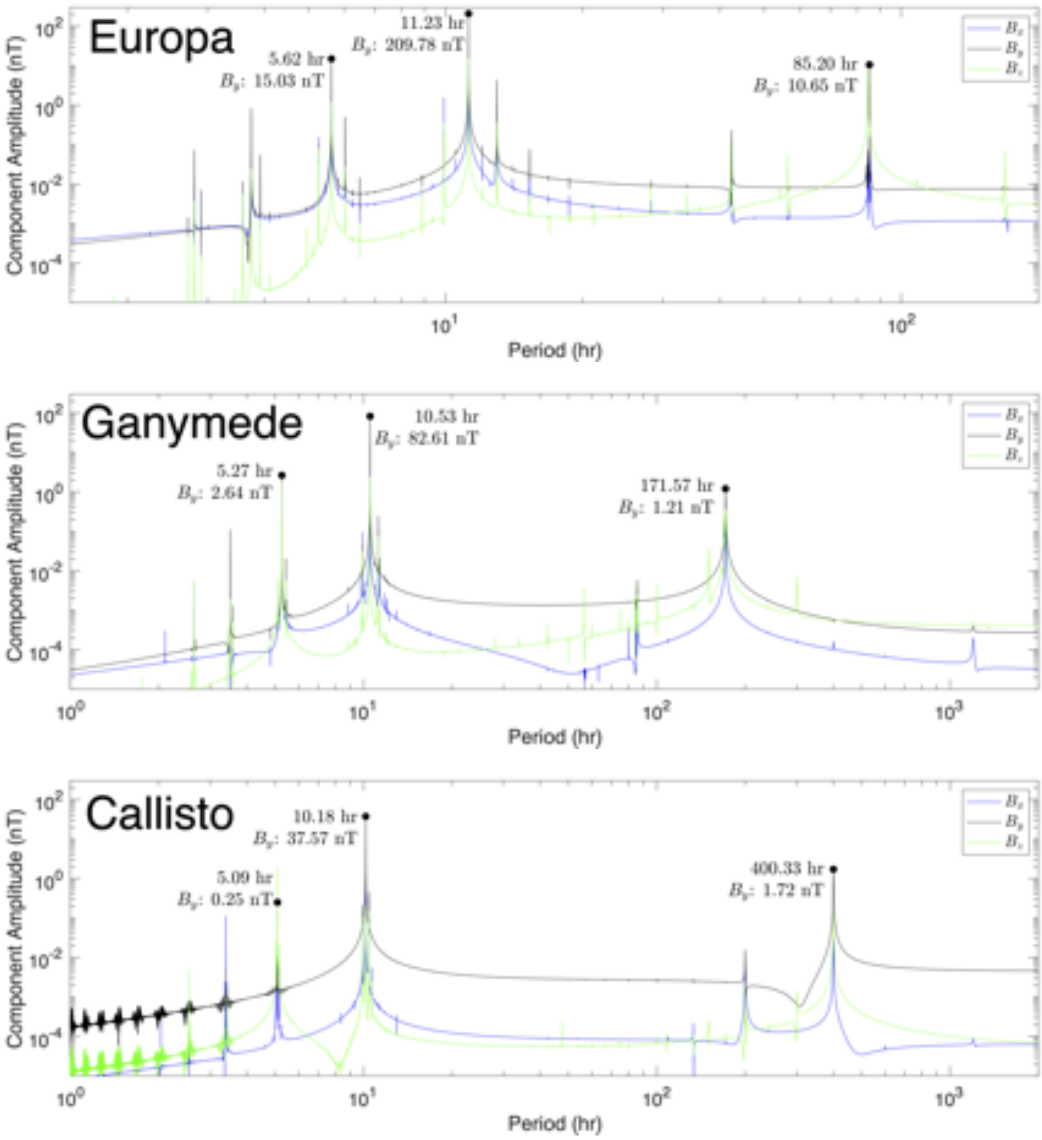


Figure 1: Time series spectra (in hr) for the largest magnetic field oscillations (in nT) experienced by the Galilean moons. Variations in orbital parameters over time introduce magnetic fluctuations at multiple periods in addition to Jupiter's synodic rotation and the satellites' orbits. The coordinate axes are detailed in Section 2.1. Peak values for the main three periods for each moon are provided in Table 1. The input time series is ten years long; the spectra are sampled with about 500,000 data points in uniform, ten-minute increments.

| | **Period (hr)** | | |
|---|---|---|---|
| | $B_{x,y,z}$ (nT) | $B_{x,y,z}$ (nT) | $B_{x,y,z}$ (nT) |
| **Europa** | **5.62** | **11.23** | **85.20** |
| | 10.03 15.03 1.22 | 75.55 209.78 15.24 | 3.17 10.65 11.97 |
| **Ganymede** | **5.27** | **10.53** | **171.57** |
| | 1.76 2.64 1.78 | 16.64 82.61 2.42 | 0.14 1.21 0.38 |
| **Callisto** | **5.09** | **10.18** | **400.33** |
| | 0.17 0.25 1.82 | 1.31 37.57 0.20 | 0.03 1.72 0.14 |

Table 1: Peak periods (in hr) and component field strengths (in nT) for the time series spectra shown in Figure 1.

for assessing the general range of possible responses. We produce comparable plots here for their utility and for ease of comparison to prior work.

Figures 2–4 show contours of the maximum induced magnetic field at the surface as a function of ocean thickness and mean ocean conductivity for each body. These figures show the signals for the three strongest driving periods, which are described in Section 2.1 and shown in Figure 1. Phase delays for the Jupiter synodic frequencies for Europa and Callisto match those described by Zimmer et al. (2000). An ice thickness of 20 km was set for Europa, consistent with previous calculations by Khurana et al. (2002) (we note that these authors did not specify what ice thickness was used). For both Ganymede and Callisto, 50 km ice shells were used. In each case, the fixed ice thickness means the seafloor depth varies to accommodate the range of $D_{\text{ocean}}$.

The amplitudes for Europa's orbital and synodic frequencies (85.23 hr and 11.23 hr) match those described by Khurana et al. (2002, 2009). However, these authors scaled the diffusive induction response to an excitation amplitude of 14 nT and 250 nT for Europa's orbital and synodic periods, respectively; in this work, each contour plot in Figures 2–4 is scaled to the largest relevant peak in the frequency spectrum in Figure 1. When we instead apply a matching scaling along with a 20 km ice shell, we generate matching figures.

By choosing a scaling that matches the applied excitation amplitudes, Figures 2–4 indicate the maximum magnetic field components that a magnetometer on the surface of each body would measure at key locations. For example, the largest variation at Ganymede's synodic period is in its $B_y$ component in $G\phi\Omega$ coordinates, approximately along the direction toward Jupiter. If a lander at the sub- or anti-jovian point on Ganymede's surface measures an induced field amplitude of 75 nT at that period, the matching ocean thickness $D_{\text{ocean}}$ and mean conductivity $\sigma_{\text{ocean}}$ must lie along the 75 nT contour. Ganymede's orbital period also has its largest oscillation in $B_y$, so including the measured amplitude at that period too determines the values for both $D_{\text{ocean}}$ and $\sigma_{\text{ocean}}$, at the crossover point between the two contours. The phase delay for each frequency offers complementary information.

In contrast with the parameter exploration reproduced here and employed in previous work, we allow ice thickness to vary. We consider how the ocean conductivity varies in accordance with the ice thickness: the melting temperature at the base sets the adiabatic temperature of the ocean, and is determined by the ocean's salinity and the pressure at the base of the ice (Vance et al., 2018). Also in contrast with the parameter space exploration depicted in Figure 2–4, we examine a smaller space of $\sigma_{\text{ocean}}$ and $D_{\text{ocean}}$ consistent with previous models of Europa's ocean composition, as described in the next section and summarized in Tables 2–4.

In this work, we do not consider the effect on the diffusive induction signal from a possible highly conductive metallic core or moderately conductive, hydrated rocky mantle in any of the satellites. One past study of Europa by Schilling (2006) determined that for even modest ocean conductivities ($\gtrsim 0.06$ S/m), the presence of a core would be all but undetectable. A mantle would similarly be easily screened by a moderately conductive ocean. Seufert et al. (2011), however, found that for some combinations of $D_{\text{ocean}}$ and $\sigma_{\text{ocean}}$, a metallic core would change the amplitude of the diffusive response by several percent and decrease the phase delay by 10° or more. A conductive core will have the most dramatic effect for the thinnest and least conductive ocean layers, at the bottom-left of Figures 2–4. For an ocean that fails to entirely screen a highly conductive core, new contours with a smaller phase delay appear in this corner of the plot. Modeling the wide parameter space of possible interior configurations that also include a core or mantle is beyond the scope of this work.

We also add to the rich set of previous analyses the exploration of a third, shorter-period signal of intermediate strength to the orbital and synodic signals. We do not consider the longer-period solar oscillation studied by Seufert et al. (2011).

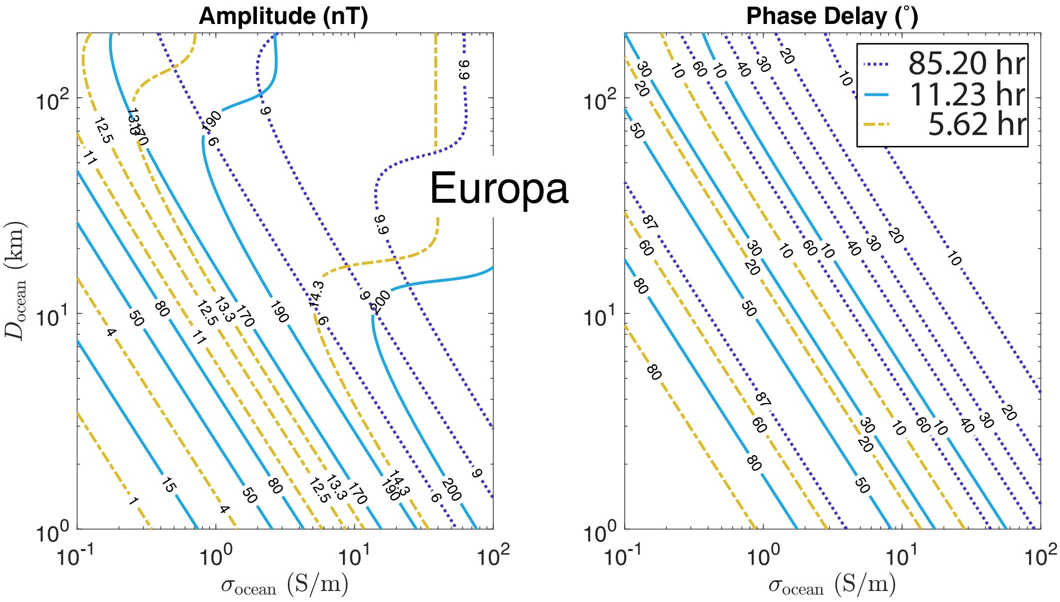


Figure 2: Europa: Contours of the maximum induced field $B_y$ components (in nT) and phase delays (in °) at the strongest inducing periods—orbital (85.20 hr; dotted), Jupiter synodic (11.23 hr; solid), and 2nd synodic harmonic (5.62 hr; dot–dash)—shown in Figure 1. The assumed, fixed ice thickness of 20 km and variable seafloor depth yield normalized amplitudes consistent with the previous calculations by Khurana et al. (2002), and phase delays for the synodic frequency matching those described by Zimmer et al. (2000). Unlike in previous work, we scale the amplitudes to the maximum component of the magnetic oscillation the satellite actually experiences at each frequency, which are the largest peaks in Figure 1.

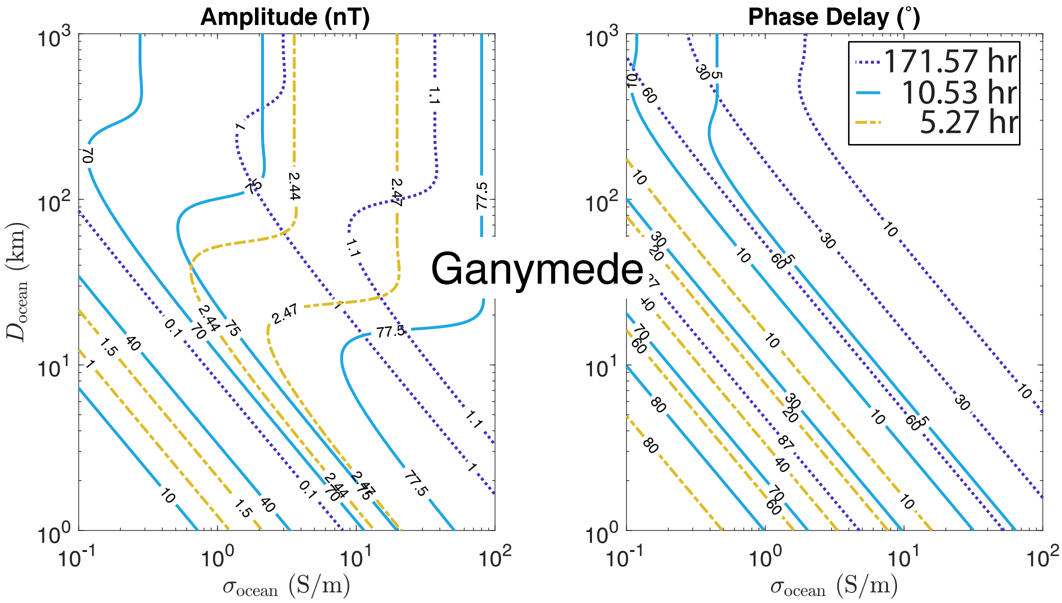


Figure 3: Ganymede: Contours of the maximum induced field $B_y$ components (in nT) and phase delays (in °) at the strongest inducing periods—orbital (171.57 hr; dotted), Jupiter synodic (10.53 hr; solid), and 2nd synodic harmonic (5.27 hr; dot–dash)—shown in Figure 1. The amplitudes and phases for the synodic and orbital periods are comparable to those described by Seufert et al. (2011) for greater ocean conductivities and thicknesses, but these authors model a highly conducting core, which we do not consider. A 50 km ice shell is assumed at the surface, implying that the seafloor depth varies to accommodate the range of $D_{\text{ocean}}$.

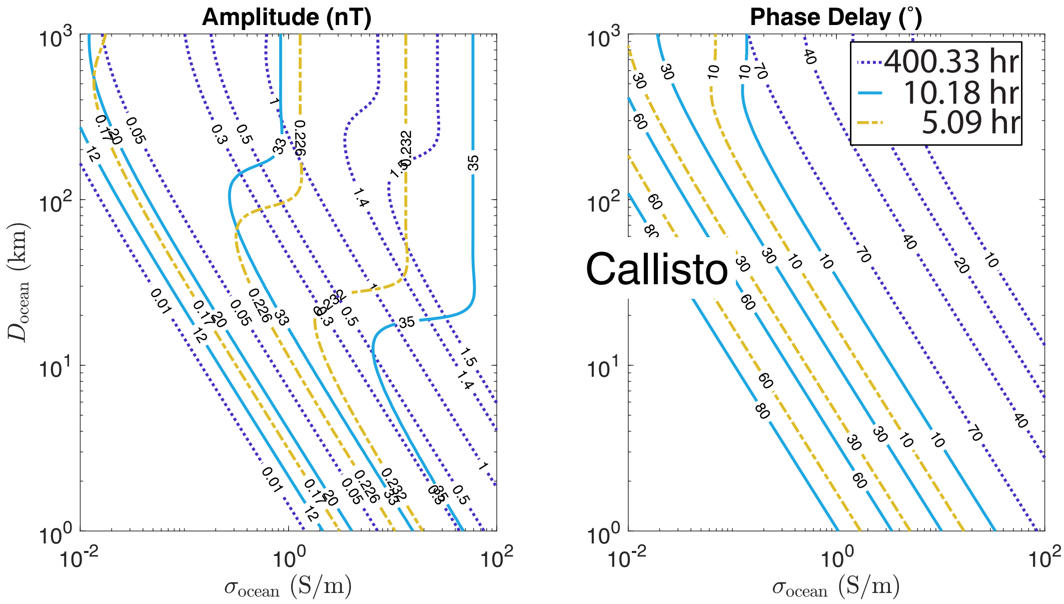


Figure 4: Callisto: Contours of the maximum induced field $B_y$ components (in nT) and phase delays (in °) at the strongest inducing periods—orbital (400.33 hr; dotted), Jupiter synodic (10.18 hr; solid), and 2nd synodic harmonic (5.09 hr; dot–dash)—shown in Figure 1. Additional harmonic short-period components will be advantageous for investigating Callisto's interior structure. The normalized amplitudes and phases for the synodic frequencies are consistent with those described by Zimmer et al. (2000). The amplitudes and phases for the synodic and orbital periods are similar to those described by Seufert et al. (2011), but these authors model a moderately conducting silicate interior, which we do not consider. A 50 km ice shell is assumed at the surface, implying that the seafloor depth varies to accommodate the range of $D_{\mathrm{ocean}}$.

### 2.3 Depth-Dependent Electrical Conductivity in Adiabatic Oceans

Fluid temperature, pressure, and salt content determine the electrical conductivity of an aqueous solution, and thus dictate the magnetic induction responses of the Galilean oceans. With sufficient prior knowledge of the ice thickness and the ocean's composition—for example, from geological and compositional measurements by the planned Europa Clipper mission (Buffington et al., 2017)—magnetic induction studies can provide information on the amounts and compositions of the salts that link to global thermal and geochemical processes.

Depth-dependence in the ocean's electrical conductivity can arise from stratification in the ocean due to melting or freezing at the ice–ocean interface, and dissolution and precipitation within the ocean or at the water–rock interface (Vance & Brown, 2005; Travis et al., 2012). Even for oceans with uniform salinity, as is typically assumed, electrical conductivity will increase with depth along the ocean's convective adiabatic profile because the greater temperature and pressure increase the electrical conductivity. Figure 5 depicts this variation for Europa, Ganymede, and Callisto, based on the forward models of Vance et al. (2018) that use available thermodynamic and geophysical data to explore the influences of the ocean, rock layer, and any metallic core on the radial structures of known icy ocean worlds. As noted by Hand and Chyba (2007), the adiabatic gradient for Europa is rather small, albeit non-zero. A more significant influence on the ocean's temperature is the influence of pressure on the melting temperature of the ice, which in turn depends on the ocean's salinity. For Ganymede and Callisto, the adiabatic gradients are large, with temperatures at the base of the thickest Ganymede ocean reaching 290 K.

As detailed in Section 2.2, we examine the magnetic induction signals from the small set of self-consistent adiabatic ocean models, taken primarily from those described in detail by Vance et al. (2018). Minor changes to the PlanetProfile software used to generate the models (Melwani Daswani et al., under review, S3) do not significantly change the ocean thicknesses and electrical conductivities reported in the previous work. We do not consider significant induction from rocky or metallic layers. For each ocean, we consider a nominal 10 wt% $MgSO_4$ salinity, as investigated in previous work. The published equation of state and electrical conductivity data are adequate for the pressures in the largest moon, Ganymede, up to 1.6 GPa, with the caveat that both have been extrapolated in pressure above about 0.7 GPa, and the laboratory data for electrical conductivity have been extrapolated below 298 K and above 1 wt% (Vance et al., 2018). The pressure conditions in Europa's ocean are low enough ($< 200$ MPa) to be in the range covered by the TEOS-10 package (McDougall & Barker, 2011), which provides plausible values of conductivity for concentrations of seawater equivalent to that of Earth's ocean (3.5 wt% NaCl) or less. For this work, we created additional lower-conductivity models for the same ice thickness, but with salinities reduced by a factor of 10 from the nominal cases.

On Europa, the flux of surface-generated oxygen to the ocean may have created oxidizing (acidic) conditions (Hand & Chyba, 2007; Pasek & Greenberg, 2012; Vance et al., 2016), permitting the presence of dissolved $MgSO_4$ in addition to NaCl (Zolotov, 2008; Zolotov & Kargel, 2009). The respective radial models of electrical conductivity for oceans containing seawater and $MgSO_4$ are consistent with compositions linked to the thermal evolution scenarios cited above (Zolotov & Kargel, 2009). In one scenario, Europa's ocean remains relatively reducing and high pH, with a composition dominated by NaCl. In the other, the flux into the ocean of oxidants generated by radiolysis of Europa's ice causes the ocean to become more oxidized and low pH, containing quantities of $MgSO_4$ exceeding the amount of NaCl. Thus the ocean's salinity and composition that might be constrained by magnetic induction measurements relate to the thermal history of Europa. The salinity measurement is also a key indicator of the types of life that might be able

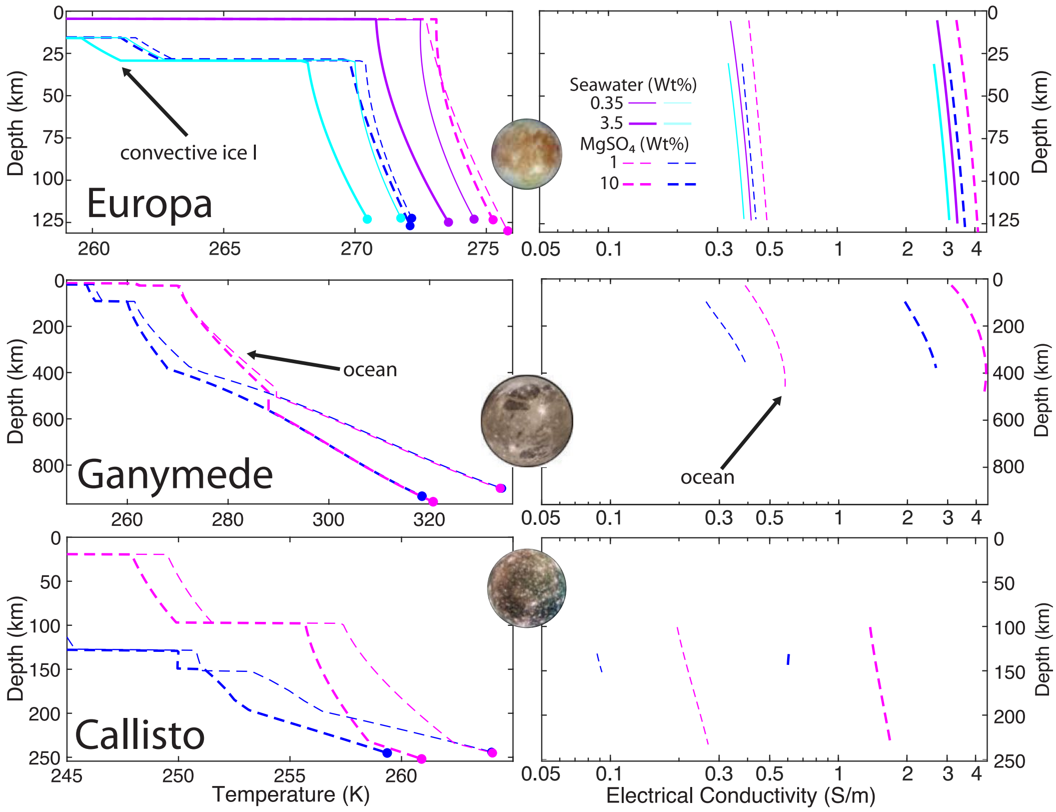


Figure 5: Adiabatic ocean temperature (left) and electrical conductivity (right). Convecting oceans with $MgSO_4$ (dashed lines) are warmer. Standard seawater (mostly NaCl; dot–dashed lines) creates colder oceans and lower electrical conductivities. Thicker ice (blue), corresponds to colder adiabatic profiles in the underlying oceans, which also lowers electrical conductivity. Filled circles show the inferred depth to the upper boundary of the silicate layer for the saline and pure water oceans, respectively. Conductivities in the liquid regions are several orders of magnitude larger than in the ice and rock, and are set to zero for this study. Adapted from Vance et al. (2018).

to live in the ocean because the chemical affinity—or energy in excess of equilibrium—for different metabolic reactions depends on the ocean's pH (Glein et al., 2019).

Radial conductivity profiles for Europa (Figure 5; top) illustrate the coupling to temperature and composition. We consider ice thicknesses of 5 and 30 km (magenta and blue curves, respectively) as representative extremes. Because we consider only the mean inferred value of the gravitational moment of inertia ($C/MR^2 = 0.346 \pm 0.005$ Schubert et al., 2004a), the hydrosphere thickness is fixed at about 125 km. Seawater (solid and dot–dashed lines), though less concentrated than the modeled composition of $MgSO_4$ (dashed lines), has a stronger melting point suppression, leading to an overall colder ocean for the same thickness of ice. The lower temperature for seawater combines with the different electrical conductivity for the different dissolved ions to create distinct profiles unique to ocean composition and ice thickness (upper right). As a result, our conductivity values differ from the summary predictions in Figure 1 of Hand and Chyba (2007) for $T = 0$ °C and 1 atm. This discrepancy from previously published values of electrical conductivity is further evident in the larger moons Ganymede and Callisto, where ocean temperatures vary farther from the freezing point at standard temperature and pressure.

Although we also fix the moments of inertia for Ganymede and Callisto to their mean published values, the depths of the ocean vary due to the presence of high pressure ices (as further discussed in Section S3). Because the melting of high pressure ices also depends on pressure (e.g., Hogenboom et al., 1995) the presence of ices above and below the ocean increases the sensitivity of the ocean's conductance to the composition and abundance of dissolved salts.

Larger Ganymede (Figure 5; middle) has distinct conductivity profiles for both ice thickness and ocean composition. Although electrical conductivity generally increases with depth, it begins to decrease at the greatest depths for the warm Ganymede ocean (right-most curve). This inflection occurs because the ocean achieves GPa+ pressures, at which the packing of water molecules begins to inhibit the charge exchange of the dissolved ions (Schmidt & Manning, 2017).

Dense brines may also reside at the base of the high-pressure ices on Ganymede, and even between them (Journaux et al., 2013, 2017; Vance et al., 2014, 2018). Although more detailed modeling of the coupled geochemical and geodynamic regimes is needed, this scenario seems consistent with recent simulations of two-phase convection in high-pressure ices (Choblet et al., 2017; Kalousová et al., 2018). These simulations show that even without the effects of dissolved salts, meltwater should form at the water–rock interface as part of the geodynamic evolution of the ice. If such a stable fluid layer exists under the high-pressure ice within Ganymede, it will create an induction response at longer periods, as discussed below.

For Callisto, there is a small range of ice I thicknesses and ocean salinities for which oceans may be present. Salty oceans considered by Vance et al. (2018) have thicknesses of 20 and 132 km. For the thinner ocean, a 96 km layer of high-pressure ice underlies the ocean. The depicted state is likely transient, as ice III is buoyant in the modeled 10 wt% $MgSO_4$ composition, and an upward snow effect should hasten the transfer of heat from the interior. Simulating a subsequent stage with ice III above the ocean awaits improved thermodynamic data that couples recently improved ice thermodynamics (Journaux et al., 2020) to the thermodynamics of aqueous phases (Bollengier et al., 2019), and is left for future work. Because of the thicker ice considered for Callisto and the consequentially lower temperature at the upper ice-ocean interface, the electrical conductivities in all Callisto models are lower than for the corresponding concentrations in Ganymede. In terms of the magnetic induction response, as shown in Section2.6, these lower conductivity values compound the lower overall conductance resulting from the thinner ocean, and also the smaller driving magnetic oscillations at more distant Callisto.

### 2.4 Accounting for the Ionospheres

For each of the above models, we add an overlying ionospheric layer based on recent analyses by Hartkorn and Saur (2017). We adopt their simplified ionospheric models, while also noting that the detailed radial and asymmetric structures of the ionospheres will affect the complex induction response and should be considered in future work. For each satellite, we consider a 100-km-thick layer extending from the surface, with Pedersen conductances of {30,2,800} S for Europa, Ganymede, and Callisto, respectively. For Callisto, we also consider a higher value of 6850 S corresponding to a Cowling channel enhancement near the equator arising from anisotropy in the current sheet, consistent with Hartkorn and Saur (2017). We use this value as an extreme case to inform the analysis of measurements near the equator. In reality, the non-spherical character of the ionosphere will influence the induction response from the one computed here, perhaps up to the order of nT (Styczinski & Harnett, 2021). The enhancement of the Cowling effect is expected to create an effective conductance only twice that of the Pedersen value at higher latitudes. For clarity in presenting the results, the effects of the ionosphere are included only in the tabulated results (Tables 2–4). Amplitudes are normalized to the moons' surface radii $R$: $A_{\mathrm{surf}} = (R_{\mathrm{top}}/R)^3 A$, where $R_{\mathrm{top}} = R + 100\mathrm{km}$, so they can be larger than unity.

### 2.5 Amplitude and Phase Delay of the Diffusive Response

Figure 6 shows the normalized surface induction responses for Europa, Ganymede, and Callisto based on the adiabatic ocean electrical conductivity profiles shown in Figure 5. Some general characteristics of the induction response may be discerned. Warmer and thus thicker oceans (magenta curves for $MgSO_4$ compositions) have larger amplitude responses, corresponding to overall higher values of the conductance. For longer periods, the influence of salinity on the amplitude responses dominate, while the thickness of the ocean dominates at shorter periods. Amplitudes approach zero around periods of $10^4$ hr. Less saline oceans have more significant phase delays at longer periods.

For Europa, the induction characteristics for modeled oxidized (10 wt% $MgSO_4$) and reduced (seawater) oceans are nearly identical in their amplitude responses. However, the two ocean models show a separation in phase delay of a few degrees at the orbital period of 85.20 hr. The combination of these features that constitutes the complex induction waveform will be key to separating them, as shown in Section 2.6.

Regional enhancements in the ocean conductivity can have a significant induction response. For Ganymede, we simulate a second ocean layer at the water–rock interface at a depth of 900 km. Lying under 530 km of ice VI (Vance et al., 2018), this layer is modeled as a 30-km-thick high-conductivity region (20 S/m) corresponding to a nearly saturated $MgSO_4$ solution, consistent with (Hogenboom et al., 1995) and (Calvert et al., 1958). The influence of such a layer (dotted lines in Figure 6) is a $\sim$1% decrease in amplitude at the orbital period of 171.57 hr. The amplitude decrease results from mutual induction between the conducting layers at this period.

For Callisto, the present simulations illustrate the influence of the thicker and deeper oceans in terms of a higher amplitude response at lower frequencies and a phase delay curve also shifted in the direction of lower frequencies.

### 2.6 Distinguishing Diffusive Responses for Different Model Oceans

We examine the possible separability of different model oceans by plotting the real and imaginary components of the induced waveforms for the peak values of Jupiter's inducing field vectors. Figure 7 shows the real and imaginary parts of the complex diffusive induction response. The normalized complex response $\mathcal{A}_n^e$ is multiplied by the strength of the excitation field $B_y$ at the driving periods shown in Figure 1, in accordance with Equation 8. $\mathcal{A}_1^e$ is equal to $Ae^{-i\phi}$, with the normalized amplitude $A$ and phase delay $\phi$ equal to those used in past studies such as Zimmer et al. (2000, see Section S1). Previous authors (including Zimmer et al. (2000)) have defined the complex response as $Ae^{i\phi}$, but they obtain a result equal to the complex conjugate of $\mathcal{A}_1^e$ because they rely on a derivation in Parkinson (1983) that contains an error (see Section S1). Relating $\mathcal{A}_1^e$ to $A$ and $\phi$ as we do enables us to use the same representation as past authors in comparing the induced magnetic field to that which would result from a perfectly conducting ocean $\mathbf{B}_{\mathrm{dif},\infty}$ at an earlier time $t - \phi/\omega$:

$$\mathbf{B}_{\mathrm{dif}}(t) = A\mathbf{B}_{\mathrm{dif},\infty}(t - \phi/\omega) \tag{10}$$

If we were to instead define $\mathcal{A}_1^e$ as equal to $Ae^{i\phi_{\mathrm{conj}}}$, $-90° \leq \phi_{\mathrm{conj}} < 0°$ and Equation 10 would then become

$$\mathbf{B}_{\mathrm{dif}}(t) = A\mathbf{B}_{\mathrm{dif},\infty}(t + \phi_{\mathrm{conj}}/\omega) \tag{11}$$

Both definitions represent the same physical result.

The quantities $B_y|\{\mathrm{Re},\mathrm{Im}\}(\mathcal{A}_1^e)|$, equivalent to $B_y A\cos\phi$ and $B_y A\sin\phi$, describe the strengths of the responses that are in phase with the excitation field—an instanta-

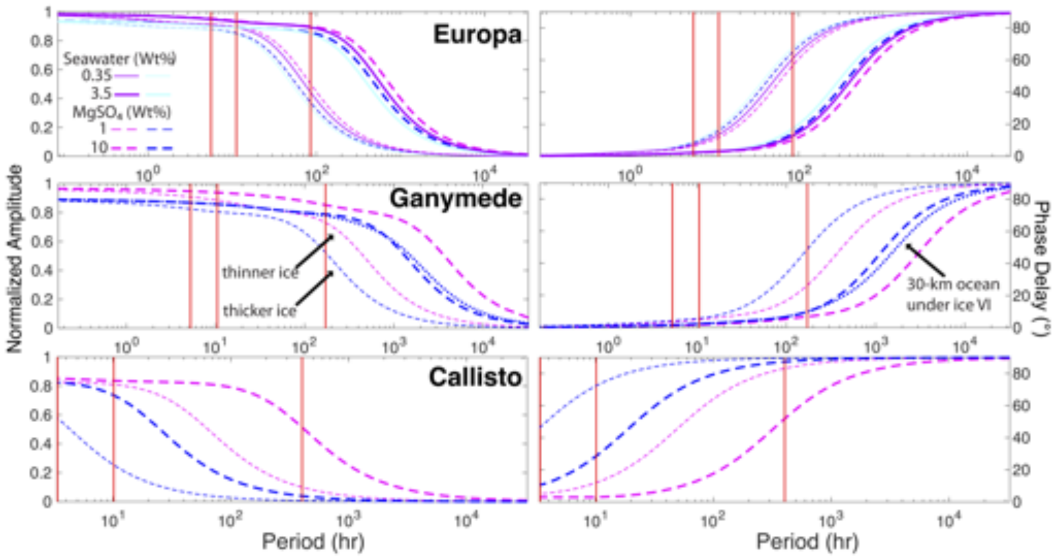


Figure 6: Normalized magnetic induction amplitudes ($A = |\mathcal{A}_1^e|$; left) and phase delays ($\phi = -\arg(\mathcal{A}_1^e)$; right) for Europa, Ganymede, and Callisto at periods including the induction peaks noted in Figure 1 (vertical red lines). As in Figure 5, dashed lines are for oceans containing $MgSO_4$. Solid and dot–dashed lines are for oceans containing seawater. Thicker lines have higher concentrations of {10,3.5} wt%, respectively, and thinner lines correspond to oceans diluted by a factor of 10. For the $MgSO_4$-bearing oceans, thinner ice corresponding to warmer oceans is denoted with magenta and thicker ice is dark blue. The trends with ice thickness/ocean temperature are the same for seawater oceans: larger amplitude and lower phase delay for thinner ice/warmer oceans. For Ganymede, the dotted line indicates the effect of introducing a 30-km-thick, 20 S/m layer at the seafloor for the thick-ice and high-salinity ocean, which is the thicker blue dashed line.

neous response that opposes the external field—and the component that is exactly 90° out of phase, respectively. Thus, the two components together describe the full range of the induction response. Tables 2–4 include the corresponding data; absolute values are implied on the out-of-phase components, consistent with considering spectral information and required by the choice of positive phase delay as in Equation 10. These tables also provide the computed values that include the modeled ionospheres, and the values computed for the equivalent oceans with the conductivity set to the mean of the adiabat and to the value at the top of the ocean. For convenience, Figures S6–S7 and Tables S1–S6 provide the corresponding data for $B_x$ and $B_z$; these corresponding values may also be obtained by substituting the field strengths in Table 1 in the data and tables for $B_y$.

#### *2.6.1 Europa*

The different phase delays and amplitudes at the orbital and synodic harmonic periods described in Section 2.5 create differences in the induction responses for different models of as much as 25 nT, comparing the in-phase synodic component of the more saline and thick ocean with the less-saline, thin ocean. The imaginary component of the induced field ($B_y A \sin\phi$) reveals the influence of the stronger phase delay for the lower-salinity oceans (Figure 7, empty symbols). The out-of-phase synodic signal in particular separates the $MgSO_4$ and seawater models of constant ice thickness by 6 nT for the lower-salinity models. For the 5 and 30 km ice thickness models, for fixed ocean composition, the separation of the stronger in-phase synodic components is 9 and 13 nT for the nominal and lower-salinity models. The synodic harmonic components differ with salinity by as much as 1.5 nT in the out-of-phase response, and by at most 0.7 nT with ice thickness in the in-phase component.

The modeled Pedersen ionosphere has a maximum induction response of about 0.7 nT in the out-of-phase synodic component Table 2. This is significant relative to the numerical precision of the calculation of about 0.001% (Figure S2). Including the ionosphere with the modeled adiabatic ocean conductivity profiles changes $B_y\{\mathrm{Re,Im}\}(\mathcal{A}_n^e)$ less than 0.05 nT. Distinguishing such signal differences in spacecraft measurements of the magnetic field requires a very careful accounting of the fields generated by plasma, which is beyond the scope of this work.

Comparing the ocean with uniform conductivity set to the mean of the adiabatic profile $\overline{\sigma}$ with the adiabatic conductivity profile, the differences in the amplitude of the response field at the surface are as much as 0.7 nT (0.4%) and 0.3 nT (0.7%) for the synodic and orbital periods. For the uniform ocean using the conductivity at the ice–ocean interface $\sigma_{\mathrm{top}}$, the orbital-period signal (85.20 hr) differs by up to 20% for the warmer and lower-salinity oceans, or about 0.5 nT.

#### *2.6.2 Ganymede*

The synodic component separates the modeled ice thicknesses of 25 and 90 km ($D_{\mathrm{ocean}} \sim$ 450 and 280 km) by about 7 nT in the in-phase $B_y$ component, and for the nominal- and low-salinity models (10 and 1 wt% $MgSO_4$) by about 4 nT in both the in- the out-of-phase components. The orbital and synodic harmonic components show a similar pattern, with separations of about 0.2 nT and 0.1 nT.

Ganymede's ionospheric conductivity is smaller than Europa's. The resulting induction response is a maximum of about 0.03 nT, which adds small contributions to the oceanic fields that are comparable to the numerical resolution of the calculation.

The uniformly conducting ocean with conductivity set to the mean of the adiabatic profile $\overline{\sigma}$ differs from the adiabatic profile in the amplitude of the response field at the surface by up to 1.2 nT (1%) and 0.03 nT (2%) at the synodic and orbital periods (Table 3 and Figure S4). The uniform ocean using the conductivity at the outermost ice–ocean interface $\sigma_{\mathrm{top}}$ differs from the adiabatic case by up to 0.18 nT (2%) for the orbital period.

#### *2.6.3 Callisto*

The synodic component shows different offsets for the thick/thin ice/ocean (130/20 km) and thinner ice/thicker ocean (100/130 km) for the two examined $MgSO_4$ compositions ({1,10} wt%). For the thinner ice (downward arrows), the in-phase synodic components differ by 1.6 nT, while the out-of-phase components differ by nearly 5 nT. Models with thicker ice (upward arrows) have larger phase delays as well as larger separations in their amplitudes at the synodic period, creating a stronger in-phase separation of 21.4 nT, and a weaker out-of-phase separation of 4.1 nT. The synodic component has a similar configuration for the amplitude and phase responses, being close in period to the synodic period, and thus shows a similar pattern of separations as the synodic signal, albeit with smaller magnitudes on the order of 0.1 nT. The orbital component has stronger separation in both amplitude and phase for the thinner ice models, leading to a proportionally larger differences in the induced field strengths, albeit for small overall magnitudes approaching zero except for the thin ice/thick ocean model that has a high salinity.

Both the Pedersen and Cowling ionospheres have strong induced field strengths and affect the induction in the presence of and ocean. For the thick-ice/thin-ocean case with low salinity the presence of the modeled ionospheres create signals of comparable or much greater magnitude than the signal of the ocean by itself. In the Cowling case the phase responses become reversed, such that the stronger field occurs for the in-phase component. Comparing these different models, the influence of the oceans creates distinct in- and out-of-phase induction responses, such that with sufficient knowledge of the properties of the ionosphere it might be possible to infer the presence of an ocean.

The uniformly conducting ocean with conductivity set to the mean of the adiabatic profile $\overline{\sigma}$ differs from the adiabatic profile in the amplitude of the response field at the surface at the orbital period (400.33 hr) by $\lesssim 2$ pT. The induction responses of the $\sigma_{\mathrm{top}}$ ocean models differ by up to 8 pT (10-20%) for the orbital period.

## 3 Motional Induction Due to Ocean Convection

We next consider motional induction driven by fluid flows within the oceans, which further complicates the interpretation of magnetic measurements. This effect is treated independently of the diffusive response considered above as a first approximation. Future work should consider the coupled induction response. Previous work by Tyler (2011) considered the possibility of magnetic remote sensing to detect resonant ocean tides on Europa in the limits of shallow water equations and thin-shell electrodynamics. Here, we focus instead on global fluid motions that may be driven by thermal convection within the oceans of Europa, Ganymede, and Callisto in the low-magnetic-Reynolds-number approximation in order to estimate upper bounds for motionally induced magnetic field amplitudes.

Thermal convection in icy satellite oceans is expected in order to efficiently transport heat from the deeper interior that arises primarily from radiogenic and tidal heating in the mantle (e.g., Soderlund et al., 2020). Using a combination of global convection models in combination with rotating convection theory, Soderlund et al. (2014) and Soderlund (2019) predicted the ocean of Europa to have large-scale flows organized into three zonal jets with retrograde (westward) flow at low latitudes and prograde (eastward) flow at high latitudes (Figure 8a). Upwelling at the equator and downwelling at mid to high latitudes effectively forms an overturning Hadley-like cell in each hemisphere (Figure 8b-c). Non-axisymmetric convective motions are quasi-three-dimensional, due to rotational and inertial timescales of the flow being comparable. Predictions for Ganymede are significantly more uncertain, but a similar configuration may be expected (Soderlund, 2019). Convection in a possible Callisto ocean may be in the double-diffusive regime (Vance & Brown, 2005; Vance & Goodman, 2009) if the ocean's salt concentration is nearly saturated (Vance et al., 2018). However, considering thermal convection as an upper bound, application of the scaling arguments in Soderlund (2019) to Callisto suggest similar ocean flows here as well. The nominal ocean model shown in Figure 8 will, therefore, be assumed for all three ocean worlds considered here, noting that the use of non-dimensional units permits different physical properties to be assumed for each satellite.

Because the modeled velocity field is given in units of the dimensionless Rossby number $Ro = U/\Omega D$ (the ratio of rotational to inertial timescales), the results can be scaled to the different satellites with assumptions about ocean thickness $D$ and rotation rate $\Omega$. A range of different ocean compositions, and therefore ocean thicknesses, are considered for velocity estimates that are given in Table 5. Intermediate ocean thicknesses across the model ranges are assumed in Figure 8. Flows are fastest for Ganymede and Europa, where the zonal jets can reach m/s speeds, the mean latitudinal flows have peak speeds of tens of cm/s, and the mean radial flows are $\sim 10$ cm/s. At Callisto, flow speeds tend to be roughly an order of magnitude weaker.

Characteristic flow speeds $U$, in combination with the physical ocean properties $\sigma$ and $D$, allow the ratio of magnetic induction to magnetic diffusion to be estimated via

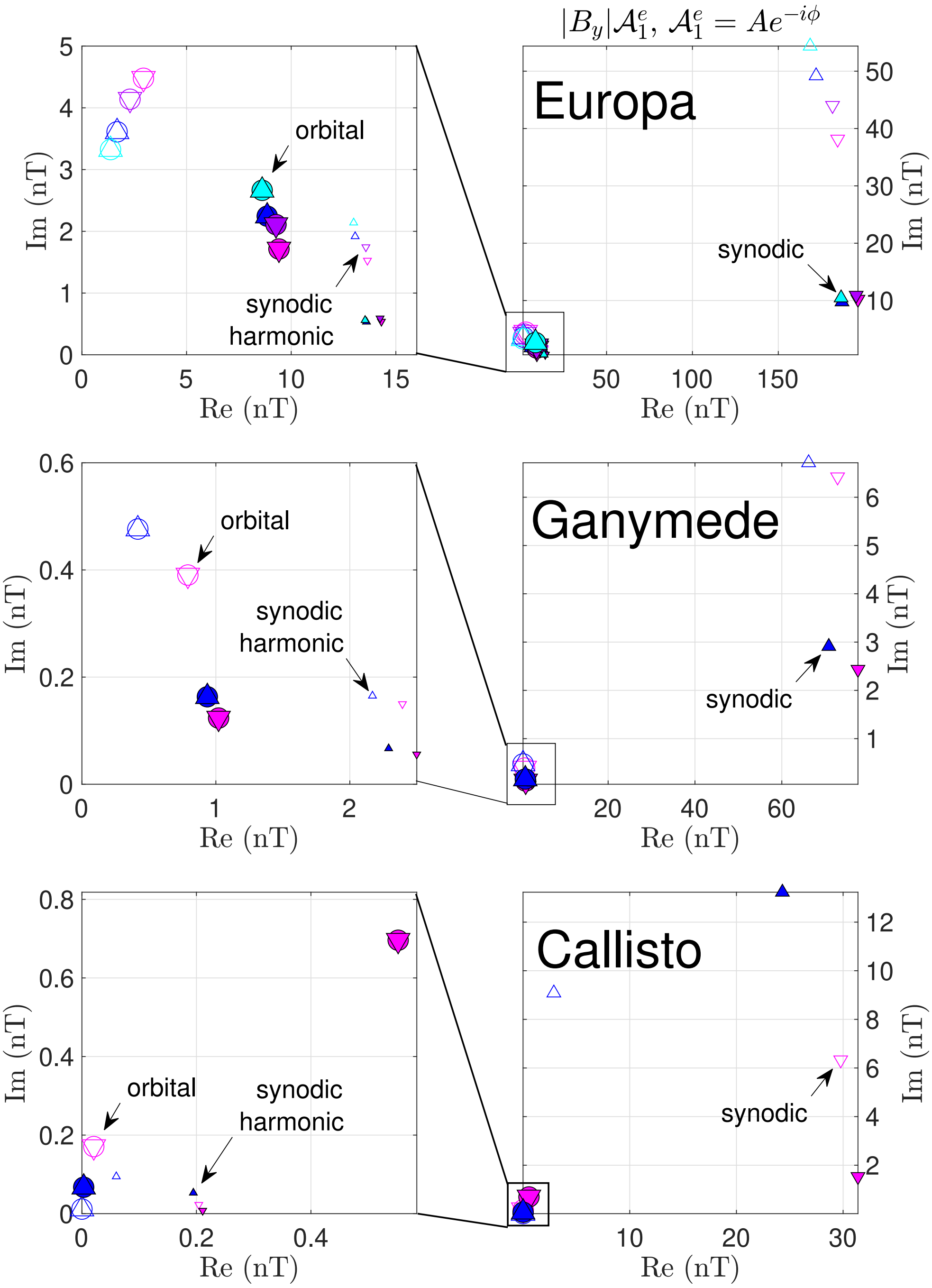


Figure 7: Real and imaginary components of the diffusive induction response to the changing $B_y$ component of Jupiter's magnetic field at the main driving periods (Figure 1) for {Europa,Ganymede,Callisto}. The real component (on the $x$-axis) is in phase with the excitation field, and the imaginary component (on the $y$-axis) is 90° out of phase, as detailed in Section 2.6. Subpanels on the left side show the lower-magnitude signals of panels on the right. Filled symbols are for the higher concentrations. Upward and downward triangles are for thicker ice ({30,95,130} km) and thinner ice ({5,26,100} km), respectively. Symbol sizes scale with the period of the oscillation, denoting the orbital (largest), the synodic (intermediate), and the synodic harmonic (smallest). Circles are added to the orbital periods to guide the eye.

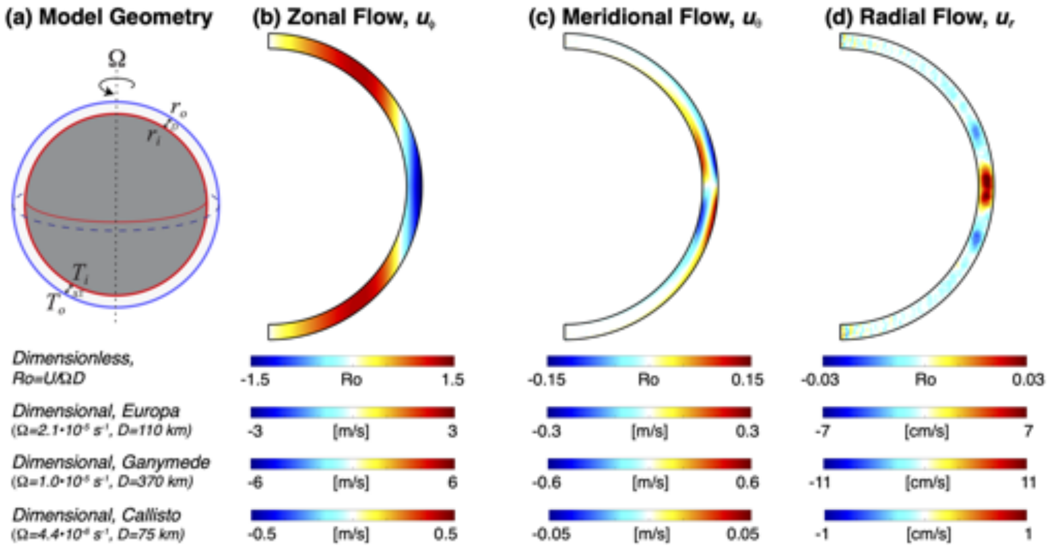


Figure 8: Mean flow fields in our nominal global ocean model from Soderlund (2019), averaged over 18 planetary rotations and all longitudes. **(a)** Geometry of the 3D ocean model. **(b)** Zonal (east–west) velocity field where red denotes prograde flows and blue denotes retrograde flows. **(c)** Meridional (latitudinal) velocity field where red denotes away from the north pole and blue denotes toward the north pole. **(d)** Radial velocity field where red denotes upwelling flows and blue denotes downwelling flows. The model has the following dimensionless input parameters: shell geometry $\chi = r_i/r_o = 0.9$, Prandtl number $Pr = \nu/\kappa = 1$, Ekman number $E = \nu/\Omega D^2 = 3.0 \times 10^{-4}$, and Rayleigh number $Ra = \alpha g \Delta T D^3/\nu\kappa$, where $r_i$ and $r_o$ are the inner and outer radii of the ocean, $D = r_o - r_i$ is ocean thickness, $\Omega$ is rotation rate, $\nu$ is kinematic viscosity, $\kappa$ is thermal diffusivity, $\alpha$ is thermal expansivity, $g$ is gravitational acceleration, and $\Delta T = T_i - T_o$ is the superadiabatic temperature contrast. The boundaries are impenetrable, stress-free, and isothermal.

the magnetic Reynolds number: $Rm = \mu_0 \sigma U D$. Using the values of these parameters from Table 5, $Rm \lesssim 1$ such that the low-magnetic-Reynolds approximation may be applied (Davidson, 2016). Here, the magnetic field $\mathbf{b}$ associated with induced current $\mathbf{J} \sim \sigma \mathbf{u} \times \mathbf{B}$ (Ohm's Law) due to velocity field $\mathbf{u}$ is small compared to the imposed magnetic field $\mathbf{B}_o$. Using Ampere's Law, the mean motionally induced field strength in the ocean can be estimated as

$$b \sim \mu_0 \sigma D U B_o \sim Rm B_o. \tag{12}$$

The resulting induced magnetic fields are thus stronger for larger electrical conductivities, ocean thicknesses, flow velocities, and satellites closer to the host planet since $B_o$ decreases with distance as $B_o = \{420, 120, 35\}$ nT for {Europa,Ganymede,Callisto} (Showman & Malhotra, 1999). Ganymede is a special case because of its intrinsic magnetic field with surface field strength of 720 nT at the equator and approximately twice that near the poles (Kivelson et al., 2002); thus, we assume here $B_o \approx 1000$ nT as a mean value. Note that a more rigorous derivation of this relationship is given in Section S2, which demonstrates that these $b$ estimates should be taken as loose upper bounds.

Table 5 summarizes the assumed ocean flows at Europa, Ganymede, and Callisto as well as estimates of their induced magnetic field strengths at the top of the ocean. Field strengths at the surface will be a factor of $(r_{ocean}/r_{satellite})^{(l+2)}$ times weaker, where $l$ is spherical harmonic degree, so the surface fields will be weaker by $\lesssim$ {6%,10%,15%} at {Europa,Ganymede,Callisto} assuming a dipole $l = 1$ configuration for the most optimistic amplitude. Our analysis focuses on the radial $b_r$ component because boundaryconfined surface currents can cause discontinuities in the tangential induced magnetic components. We also assume flow speeds typical of the steady overturning cells due to their temporal persistence and large spatial scale, which we hypothesize will produce the strongest induced magnetic signatures and would be more easily discernable by spacecraft. We find that $b_r \lesssim 20$ nT for Europa, $b_r \lesssim 300$ nT for Ganymede, and $b_r \lesssim 1$ nT for Callisto. Implications of these field estimates on magnetic measurements and future work needed for their refinement are discussed in the next section.

## 4 Discussion and Conclusions

The inverse problem of reconstructing the full induction response from spacecraft data is beyond the scope of this work, and is discussed in detail elsewhere (e.g., Khurana et al., 2009, and Cochrane et al. *in progress*). We focus here on the significance and separability of the diffusive induction responses for the physically consistent models described above. We examine the likelihood of being able to detect and separate the signals of motional induction from the diffusive signals. We also discuss the merits of using physically consistent models as inputs to the inverse problem, the future experimental and modeling work that is needed for material properties and motional induction, and the implications for future missions.

### 4.1 Significance and Separability of the Diffusive and Motional Signals

The representative, physically consistent structures of Jupiter's ocean moons that we model have distinct magnetic induction signals when the phase delays are considered. The waveform responses at the three characteristic periods identified for each moon (Figure 7; Tables 2–4) illustrate the possibility for inferring key properties of the moons, possibly by planning missions (Section 4.3). This study demonstrates the existence of magnetic induction responses tracing to the unique melting curves of different ocean compositions, and thus to physical features arising from their coupled thermal and chemical evolution. Lower salinity oceans have larger induced responses that are out of phase with Jupiter's rotating field.

For Europa, models consistent with reducing/oxidizing ($MgSO_4$-/NaCl-dominated) oceans have distinct induction features at all three periods considered here. We find that a motionally induced field of $b_r \lesssim 20$ nT for Europa, or up to 5% of the ambient jovian field. For comparison, the field strength induced by tidal motions (Rossby–Haurwitz response to obliquity tidal forcing) is $\sim 1$ nT (Tyler, 2011) and at Jupiter's synodic period of 11.23 hr is $\lesssim$200 nT (Figure 7; Table 2). Schilling et al. (2004) found an upper limit for an intrinsic magnetic field at Europa to be 25 nT at the surface, implying that an observable signal from motional flows may have gone unnoticed there. A detailed analysis is required to better characterize the potential response and its implications for determining ocean composition, salinity, and convective flows.

For Ganymede, the tabulated results (Table 3) show that a plausible liquid layer at the rock interface beneath the high pressure ice would create an in-phase signal of about 0.01 nT at the orbital period. The ionosphere should not impede sensing the induction response of the ocean. Here, $b_r \lesssim 300$ nT, which approaches half of the equatorial surface strength of the satellite's intrinsic field for the thickest, saltiest ocean considered; magnetic fields induced at Jupiter's synodic period of 10.53 hr are $\lesssim$80 nT (Figure 7; Table 3). As a result, these motionally induced magnetic fields warrant further study as they may allow ocean flows to be inferred, may bias electrical conductivity inversions, and/or may complicate extraction of Ganymede's core dynamo magnetic field component.

For Callisto, strong induction responses ($>$ 10 nT) characteristic of the ocean's conductivity and thickness might exist at the synodic period of Jupiter's rotation, with smaller signals ($>$ nT). However, the modeled Cowling ionosphere without any ocean creates a strong induction response that is not easily distinguished from an oceanic signal. Motional inductions signals of $b_r \lesssim 1$ nT are less significant relative to the peak strength ($\lesssim 30$ nT) of the field induced at Jupiter's synodic period of 10.18 hr (Figure 7; Table 4). Thus, as demonstrated and further discussed by Hartkorn and Saur (2017), magnetic induction measured by the Galileo spacecraft (Kivelson et al., 1999) might be explained as resulting from the response of Callisto's ionosphere and not an ocean.

Structural models of ocean worlds (e.g., Schubert et al., 2004b) often assume a uniform ocean temperature determined by the melting temperature of the ice–ocean interface. Using this temperature as the basis for the ocean's electrical conductivity leads to large differences from the more physically consistent, adiabatic case. The greater mismatch of conductivities of the lower part of the ocean causes large differences in amplitude and phase at longer periods (i.e. for larger skin depths).

Prior analyses of magnetic induction in Jupiter's ocean moons have all assumed a uniform conductivity of the oceans (Kivelson et al., 2000, 2002; Khurana et al., 2002; Schilling et al., 2007; Seufert et al., 2011). For all three moons, we compared the diffusive response for a uniformly conducting ocean with conductivity set to a reference value from the adiabatic conductivity profile. We find that the diffusive induction responses of the oceans with uniform conductivity equal to the mean of the adiabatic profile are, for many interior configurations, a reasonable approximation to the induction response for a more realistic electrical conductivity following the adiabatic profile. The response amplitudes are most distinct between the adiabatic and mean-conductivity oceans for the thin-ice, lower-salinity configurations.

For the mean-conductivity oceans ($\overline{\sigma}$), the in-phase response amplitudes are all larger than for the corresponding adiabatic profiles and the out-of-phase amplitudes mostly decrease slightly (see Tables 2–4).

**For Europa,** the in-phase response amplitudes range from about 0.22% to 0.46% greater for the synodic period and from 0.28% to 1.02% greater for the orbital period; the out-of-phase responses range from 2.87% less to 0.03% greater for the synodic period and from 0.10% less to 0.63% greater for the orbital period. Larger differences are observed for thinner-ice, warmer oceans in all cases.

**For Ganymede,** the in-phase response amplitudes range from about 0.38% to 1.23% greater for the synodic period and from 1.01% to 2.61% greater for the orbital period; the out-of-phase responses range from 9.78% to 2.65% less for the synodic period and from 3.07% less to 1.41% greater for the orbital period. These excesses/deficits in the synodic/orbital component differences arise because the mean conductivity case increases/reduces the conductance contributed by the shallower/deeper parts of the ocean (Figure 5) associated with smaller/larger skin depths of the diffusive response.

**For Callisto,** the in-phase response amplitudes range from 0.00% to 0.53% greater for the synodic period and from 0.00% to 1.45% greater for the orbital period; the out-of-phase responses range from 1.74% less to 0.03% greater for the synodic period and from 0.00% to 0.96% greater for the orbital period. For the thicker oceans, where conductivity changes with depth, the differences are similar to those for Ganymede.

We also considered the diffusive response from uniformly conducting oceans with a conductivity equal to that at the ice–ocean interface ($\sigma_{\text{top}}$) in comparison to the adiabatic profiles (see Tables 2–4). Unlike the mean-conductivity oceans, there is not a consistent pattern of larger or smaller responses when compared to the adiabatic case.

**For Europa,** the in-phase response amplitudes range from about 1.49% less to 0.10% greater for the synodic period and from 16.33% to 0.34% less for the orbital period; the out-of-phase responses range from 2.13% to 10.77% greater for the synodic period and from 5.92% less to 11.33% greater for the orbital period. Differences are consistently large in this comparison.

**For Ganymede,** the in-phase response amplitudes range from about 0.14% less to 0.45% greater for the synodic period and from 22.82% to 0.11% less for the orbital period; the out-of-phase responses range from 2.51% less to 10.74% greater for the synodic period and from 3.32% less to 17.09% greater for the orbital period. For the lower-salinity ocean we model, the marked difference in phase delay between the thin-ice, warmer profile and the thick-ice, colder profile (Figure 6) is evident in how the in-phase and out-of-phase components change between the two cases.

**For Callisto,** the in-phase response amplitudes range from about 4.12% less to 0.28% greater for the synodic period and from 26.08% less to 1.23% greater for the orbital period; the out-of-phase responses range from 1.87% less to 15.03% greater for the synodic period and from 13.62% less to 0.61% greater for the orbital period. The lower phase lag of the nominal salinity case for the thicker ocean is evident in the differences between the in-phase and out-of-phase components from the other cases.

For larger oceans, where the non-linear pressure behavior of the adiabat introduces curvature to the electrical conductivity profile, slightly larger differences can arise for thicker oceans. The presence of high pressure ice also enhances the sensitivity of the overall ocean thickness to the ocean's salinity.

### 4.2 Future Experimental and Modeling Work

The diffusive induction models described in Section 2.3 make use of thermodynamic and electrical conductivity data developed for applications to ocean worlds (Vance & Brown, 2013; Vance et al., 2018). Future work should explore a broader space of compositions. Constructing models that account for the effects of high concentration and pressure requires updated thermodynamic data (Bollengier et al., 2019; Journaux et al., 2020), as described above, matched with accurate electrical conductivity data. Recent progress in applying electrical conductivity to geochemical systems at Earth's surface (McCleskey et al., 2012) provides a starting point for considering oceanic concentrations with realistic assemblages of salts (Zolotov & Shock, 2001; Kargel et al., 2000). Extending these data to high pressures and concentrations requires further experimental work (e.g., Keppler, 2014; Guo & Keppler, 2019). Future investigations should also examine a fuller parameter space of interior structures, including conductivity in the solid layers. Such future work should examine a broader range of ice and hydrosphere thicknesses, including density structures that explore the full range of constraints based on Galileo gravity data, not just the mean values of the moments of inertia (Schubert et al., 2004a; Vance et al., 2019). Future work should also examine asymmetry in the conducting layers. Recent work by Styczinski and Harnett (2021) permits consideration of small deviations from spherical symmetry, for example due to long-wavelength variations in the thickness of Europa's ice (Nimmo et al., 2007). Ultimately, the ability to consider diffusive magnetic induction from electrically conducting regions with arbitrary geometry would enable accounting for the effects of the Cowling ionosphere at Callisto (Hartkorn & Saur, 2017), meridional variations in salinity at Europa (Zhu et al., 2017), brine lenses in Europa's ice (Schmidt et al., 2011).

The simplified approach to motional induction described in Section 3 gives order-of-magnitude estimates of the maximum induced fields due to ocean convection and shows that these fields may be large enough to impact interpretations of magnetic measurements. Future work will assess the implications of the simplifying assumptions made through more detailed calculations. For example, we have assumed homogeneous and constant jovian and Ganymede background fields; however, the temporal and spatial variation of the ambient fields are expected to be significant and the magnetic environment each satellite experiences throughout its orbit is highly dynamic (e.g., Bagenal et al., 2015). The influence of these variations on ocean-flow-driven magnetic field signatures also remains to be explored (cf. Gissinger & Petitdemange, 2019). Kinematic models that directly solve the coupled momentum and induction equations to determine the motionally induced magnetic fields are an exciting and necessary future venue to refine these estimates. The resulting predictions for field strength and spatial structure may allow the motional and diffusive components of the induced magnetic field to be separated, facilitating better electrical conductivity inversions and ocean flow hypothesis tests.

### 4.3 Implications for Future Missions

The Europa Clipper mission will conduct multiple (>40) flybys of Europa, and will investigate its magnetic induction response with the goal of constraining the ocean salinity and ice thickness, each to within 50%. With independent constraints on ice thickness obtained from the Radar for Europa Assessment and Sounding: Ocean to Near-surface (REASON) and Europa Imaging System (EIS) investigations (Steinbrügge et al., 2018), it may be possible to constrain the ocean's temperature and thus the adiabatic structure for the best-fit ocean composition inferred from compositional investigations. The analyses provided here (Figure 7 and Table 2) indicate that a sensitivity of 1.5 nT is probably sufficient to distinguish between the end-member $MgSO_4$ and NaCl oceans, and the corresponding ice thicknesses considered here.

The JUpiter ICy moons Explorer (JUICE) mission will execute two Europa flybys and nine Callisto flybys, and will orbit Ganymede (Grasset et al., 2013). The magnetic field investigation seeks to determine the induction response to better than 0.1 nT. The Europa flybys might aid the Europa Clipper investigation in constraining the composition of the ocean. We find that at Ganymede, JUICE's magnetic field investigation will not be sufficient to discern the modeled basal liquid layer at the ice VI–rock interface, which would require sensitivity better than 0.01 nT. Although the ability to discern between ocean compositions could not be assessed owing to insufficient thermodynamic and electrical conductivity data at high pressures, it seems likely that useful constraints could be derived based on the signal strengths at Ganymede, if appropriate laboratory-derived data for relevant solutions under pressure became available. Motional induction also appears to be even more important to consider at Ganymede than Europa.

At Callisto, both Europa Clipper and JUICE would be able to investigate the synodic signals that vary by more than 2 nT for the different models considered here, including models with only an ionosphere. JUICE's 0.1 nT sensitivity might be able to obtain useful information at the orbital and first harmonic periods as well. In contrast with Europa and Ganymede, however, good knowledge of the ionospheric structure at Callisto is required for detecting an ocean.

**Acknowledgments**

Work by JPL co-authors was partially supported by the Jet Propulsion Laboratory, Caltech, and by the Icy Worlds node of NASA's Astrobiology Institute (13-13NAI7_2-0024). This work was partially supported by NASA's Europa Clipper project. Work by MJS was supported by the NASA Earth and Space Science Fellowship Program - Grant 80NSSC18K1236. Work by KMS was also supported by NASA Grant NNX14AR28G.

The Matlab scripts and associated data needed to compute the results of this work are archived as a release on github (https://github.com/vancesteven/PlanetProfile) with DOI: 10.5281/zenodo.4052711.

All global ocean convection model data were first published in Soderlund (2019) and are available therein.

## References


Acuna, M. H., & Ness, N. F. (1976). The main magnetic field of jupiter. *Journal of Geophysical Research*, *81*(16), 2917–2922. doi: 10.1029/ja081i016p02917

Bagenal, F., Sidrow, E., Wilson, R. J., Cassidy, T. A., Dols, V., Crary, F. J., ... Paterson, W. R. (2015). Plasma conditions at Europaâs orbit. *Icarus*, *261*, 1–13.

Bollengier, O., Brown, J. M., & Shaw, G. H. (2019). Thermodynamics of pure liquid water: Sound speed measurements to 700 MPa down to the freezing point, and an equation of state to 2300 MPa from 240 to 500 K. *The Journal of Chemical Physics*, *151*(5), 054501. doi: 10.1063/1.5097179

Buffington, B., Lam, T., Campagnola, S., Ludwinski, J., Ferguson, E., Bradley, B., ... Siddique, F. (2017). Evolution of trajectory design requirements on NASA's planned Europa Clipper mission. *Proceedings of the 68th International Astronautical Congress (IAC)*(IAC-17-C1.7.8).

Calvert, R., Cornelius, J. A., Griffiths, V. S., & Stock, D. I. (1958). The determination of the electrical conductivities of some concentrated electrolyte solutions using a transformer bridge. *The Journal of Physical Chemistry*, *62*(1), 47–53.

Chave, A. D. (1983). On the theory of electromagnetic induction in the Earth by ocean currents. *J. Geophys. Res.*, *88*, 3531–3542.

Choblet, G., Tobie, G., Sotin, C., Kalousová, K., & Grasset, O. (2017). Heat transport in the high-pressure ice mantle of large icy moons. *Icarus*, *285*, 252–262. doi: 10.1016/j.icarus.2016.12.002

Connerney, J., Acuna, M., & Ness, N. (1981). Modeling the Jovian current sheet and inner magnetosphere. *Journal of Geophysical Research: Space Physics*, *86*(A10), 8370–8384.

Connerney, et al. (1998). New models of Jupiter's magnetic field constrained by the Io flux tube footprint. *Journal of Geophysical Research: Space Physics*, *103*(A6), 11929–11939.

Connerney, J. E. P., Kotsiaros, S., Oliversen, R. J., Espley, J. R., Joergensen, J. L., Joergensen, P. S., Merayo, J. M. G., Herceg, M., Bloxham, J., Moore, K. M., and et al. (2018). A new model of Jupiter's magnetic field from Juno's first nine orbits. *Geophysical Research Letters*, *45*(6), 2590–2596. doi: 10.1002/2018gl077312

Constable, S., & Constable, C. G. (2004). Observing geomagnetic induction in magnetic satellite measurements and associated implications for mantle conductivity. *Geochem. Geophys. Geosys.*, *5*, Q01006.

Davidson, P. A. (2016). *Introduction to magnetohydrodynamics* (2nd ed.). Cambridge University Press. doi: 10.1017/9781316672853

Eckhardt, D. H. (1963). Geomagnetic induction in a concentrically stratified earth. *Journal of Geophysical Research*, *68*(23), 6273–6278. doi: 10.1029/jz068i023p06273

Gissinger, C., & Petitdemange, L. (2019). A magnetically driven equatorial jet in Europa's ocean. *Nature Astron.*, *1*.

Glein, C., Postberg, F., & Vance, S. (2019). The geochemistry of Enceladus: Composition and controls. In (p. 39-56). University of Arizona Press.

Grasset, O., Dougherty, M., Coustenis, A., Bunce, E., Erd, C., Titov, D., ... others (2013). Jupiter icy moons explorer (juice): An esa mission to orbit ganymede and to characterise the jupiter system. *Planetary and Space Science*, *78*, 1–21.

Grayver, A. V., Schnepf, N. R., Kuvshinov, A. V., Sabaka, T. J., Manoj, C., & Olsen, N. (2016). Satellite tidal magnetic signals constrain oceanic lithosphere-asthenosphere boundary. *Science Adv.*, *2*(9), e1600798.

Guo, H., & Keppler, H. (2019). Electrical conductivity of NaCl-bearing aqueous fluids to 900 °C and 5 GPa. *Journal of Geophysical Research: Solid Earth*, *124*(2), 1397–1411. doi: 10.1029/2018jb016658

Hand, K., & Chyba, C. (2007). Empirical constraints on the salinity of the europan ocean and implications for a thin ice shell. *Icarus*, *189*(2), 424–438.

Hartkorn, O., & Saur, J. (2017). Induction signals from Callisto's ionosphere and their implications on a possible subsurface ocean. *Journal of Geophysical Research: Space Physics*, *122*(11), 11,677–11,697. doi: 10.1002/2017ja024269

Hogenboom, D. L., Kargel, J. S., Ganasan, J. P., & Lee, L. (1995). Magnesium sulfate-water to 400 MPa using a novel piezometer: Densities, phase equilibria, and planetological implications. *Icarus*, *115*(2), 258–277.

Jones, C. A., & Kuzanyan, K. M. (2009). Compressible convection in the deep atmospheres of giant planets. *Icarus*, *358*, 873–897.

Journaux, B., Brown, J., Pakhomova, A., Collings, I., Petitgirard, S., Espinoza, P., ... et al. (2020, Dec). Holistic approach for studying planetary hydrospheres: Gibbs representation of ices thermodynamics, elasticity and the water phase diagram to 2300 MPa. *Journal of Geophysical Research: Planets*, *125*, e2019JE006176. doi: 10.1029/2019je006176

Journaux, B., Daniel, I., Caracas, R., Montagnac, G., & Cardon, H. (2013). Influence of NaCl on ice VI and ice VII melting curves up to 6GPa, implications for large icy moons. *Icarus*, *226*(1), 355–363. doi: 10.1016/j.icarus.2013.05.039

Journaux, B., Daniel, I., Petitgirard, S., Cardon, H., Perrillat, J.-P., Caracas, R., & Mezouar, M. (2017). Salt partitioning between water and high-pressure ices. implication for the dynamics and habitability of icy moons and water-rich planetary bodies. *Earth and Planetary Science Letters*, *463*, 36–47. doi: 10.1016/j.epsl.2017.01.017

Kalousová, K., Sotin, C., Choblet, G., Tobie, G., & Grasset, O. (2018). Two-phase convection in Ganymede's high-pressure ice layer — implications for its geological evolution. *Icarus*, *299*, 133–147. doi: 10.1016/j.icarus.2017.07.018

Kargel, J. S., Kaye, J. Z., Head, J. W., III, Marion, G. M., Sassen, R., Crowley, J. K., ... Hogenboom, D. L. (2000). Europa's crust and ocean: Origin, composition, and the prospects for life. *Icarus*, *148*(1), 226–265.

Keppler, H. (2014). Electrical conductivity measurements of aqueous fluids under pressure with a hydrothermal diamond anvil cell. *Review of Scientific Instruments*, *85*(11), 115107. doi: 10.1063/1.4902152

Khurana, K., Kivelson, M., Hand, K., & Russell, C. (2009). Electromagnetic induction from europa's ocean and the deep interior. *Europa, Edited by Robert T. Pappalardo, William B. McKinnon, Krishan K. Khurana; with the assistance of René Dotson with 85 collaborating authors. University of Arizona Press, Tucson, 2009. The University of Arizona space science series ISBN: 9780816528448, p. 571*, *1*, 571.

Khurana, K.et al. (2002). Searching for liquid water in Europa by using surface observatories. *Astrobiology*, *2*(1), 93–103.

Khurana, K., Kivelson, M., Stevenson, D., Schubert, G., Russell, C., Walker, R., & Polanskey, C. (1998). Induced magnetic fields as evidence for subsurface oceans in Europa and Callisto. *Nature*, *395*(6704), 777–780.

Khurana, K. K. (1997). Euler potential models of Jupiter's magnetospheric field. *Journal of Geophysical Research: Space Physics*, *102*(A6), 11295–11306. doi: 10.1029/97ja00563

Kivelson, M., Khurana, K., Russell, C., Volwerk, M., Walker, R., & Zimmer, C. (2000). Galileo magnetometer measurements: A stronger case for a subsurface ocean at Europa. *Science*, *289*, 1340–1343.

Kivelson, M., Khurana, K., Stevenson, D., Bennett, L., Joy, S., Russell, C., ... Polanskey, C. (1999). Europa and Callisto: Induced or intrinsic fields in a periodically varying plasma environment. *Journal of Geophysical Research*, *104*(A3), 4609–4625.

Kivelson, M., Khurana, K., & Volwerk, M. (2002). The permanent and inductive magnetic moments of Ganymede. *Icarus*, *157*(2), 507–522.

Lainey, V., Duriez, L., & Vienne, A. (2006). Synthetic representation of the Galilean satellites' orbital motions from L1 ephemerides. *A&A*, *456*, 783–788.

Le Bars, M., Cebron, D., & Le Gal, P. (2015). Flows driven by libration, precession, and tides. *Annu. Rev. Fluid Mech.*, *47*, 163–193.

Lieske, J. (1998). Galilean satellite ephemerides E5. *Astronomy and Astrophysics Supplement Series*, *129*(2), 205–217.

Liuzzo, L., Feyerabend, M., Simon, S., & Motschmann, U. (2015). The impact of Callisto's atmosphere on its plasma interaction with the jovian magnetosphere. *Journal of Geophysical Research: Space Physics*, *120*(11), 9401–9427. doi: 10.1002/2015ja021792

McCleskey, R. B., Nordstrom, D. K., Ryan, J. N., & Ball, J. W. (2012). A new method of calculating electrical conductivity with applications to natural waters. *Geochimica et Cosmochimica Acta*, *77*, 369–382. doi: 10.1016/j.gca.2011.10.031

McDougall, T. J., & Barker, P. M. (2011). Getting started with TEOS-10 and the Gibbs Seawater (GSW) oceanographic toolbox. *SCOR/IAPSO WG*, *127*, 1–28.

Melwani Daswani, M., Vance, S. D., Mayne, M. J., & Glein, C. R. (under review). A metamorphic origin for europa's ocean. *Geophysical Research Letters*.

Minami, T. (2017). Motional induction by tsunamis and ocean tides: 10 years of progress. *Surv. Geophys.*, *38*, 1097–1132.

Nimmo, F., Thomas, P., Pappalardo, R., & Moore, W. (2007). The global shape of Europa: Constraints on lateral shell thickness variations. *Icarus*, *191*(1), 183–192.

Parkinson, W. (1983). *Introduction to geomagnetism.* Scottish Academic Press (Edinburgh).

Pasek, M. A., & Greenberg, R. (2012). Acidification of Europa's subsurface ocean as a consequence of oxidant delivery. *Astrobiology*, *12*(2), 151–159.

Saur, J., Neubauer, F. M., & Glassmeier, K.-H. (2009). Induced magnetic fields in solar system bodies. *Space Science Reviews*, *152*(1-4), 391–421. doi: 10.1007/s11214-009-9581-y

Saur, J., Strobel, D. F., & Neubauer, F. M. (1998). Interaction of the jovian magnetosphere with europa: Constraints on the neutral atmosphere. *Journal of Geophysical Research: Planets*, *103*(E9), 19947–19962. doi: 10.1029/97je03556

Schilling, N. (2006). *Time varying interaction of Europa's atmosphere-ionosphere and its conducting ocean with the Jovian magnetosphere* (Unpublished doctoral dissertation). Universität zu Köln.

Schilling, N., Khurana, K., & Kivelson, M. (2004). Limits on an intrinsic dipole moment in Europa. *Journal of Geophysical Research: Planets*, *109*(E5).

Schilling, N., Neubauer, F. M., & Saur, J. (2007). Time-varying interaction of europa with the jovian magnetosphere: Constraints on the conductivity of Europa's subsurface ocean. *Icarus*, *192*(1), 41–55.

Schmidt, B., Blankenship, D., Patterson, G., & Schenk, P. (2011). Active formation of chaos terrain over shallow subsurface water on Europa. *Nature*, *479*(7374), 502–505.

Schmidt, C., & Manning, C. (2017). Pressure-induced ion pairing in $MgSO_4$ solutions: Implications for the oceans of icy worlds. *Geochemical Perspectives Letters*, *3*, 66-74.

Schubert, G., Anderson, J., Spohn, T., & McKinnon, W. (2004). Interior composition, structure and dynamics of the Galilean satellites. *Jupiter: The Planet, Satellites and Magnetosphere*, 281–306.

Schubert, G., Anderson, J. D., Spohn, T., & McKinnon, W. B. (2004). Interior composition, structure and dynamics of the Galilean satellites. *Jupiter: The Planet, Satellites and Magnetosphere*, 281–306.

Seufert, M., Saur, J., & Neubauer, F. M. (2011). Multi-frequency electromagnetic sounding of the Galilean moons. *Icarus*, *214*(2), 477–494.

Showman, A. P., & Malhotra, R. (1999). The galilean satellites. *Science*, *286*(5437), 77–84.

Soderlund, K. M. (2019). Ocean dynamics of outer solar system satellites. *Geophys. Res. Lett.*, https://doi.org/10.1029/2018GL081880.

Soderlund, K. M., Kalousová, K., Buffo, J. J., Glein, C. R., Goodman, J. C., Mitri, G., ... others (2020). Ice-ocean exchange processes in the jovian and saturnian satellites. *Space Science Reviews*, *216*(5), 1–57.

Soderlund, K. M., Schmidt, B. E., Wicht, J., & Blankenship, D. D. (2014). Ocean-driven heating of Europa's icy shell at low latitudes. *Nature Geosci.*, *7*, 16-19.

Srivastava, S. P. (1966). Theory of the magnetotelluric method for a spherical conductor. *Geophysical Journal International*, *11*(4), 373–387. doi: 10.1111/j.1365-246x.1966.tb03090.x

Steinbrügge, G., Schroeder, D., Haynes, M., Hussmann, H., Grima, C., & Blankenship, D. (2018). Assessing the potential for measuring Europa's tidal Love number h2 using radar sounder and topographic imager data. *Earth and Planetary Science Letters*, *482*, 334–341. doi: 10.1016/j.epsl.2017.11.028

Styczinski, M. J., & Harnett, E. M. (2021). Induced magnetic moments from a nearly spherical ocean. *Icarus*, *354*, 114020. doi: 10.1016/j.icarus.2020.114020

Travis, B., Palguta, J., & Schubert, G. (2012). A whole-moon thermal history model of Europa: Impact of hydrothermal circulation and salt transport. *Icarus*, *218*, 1006-1019.

Tyler, R. H. (2011). Magnetic remote sensing of Europa's ocean tides. *Icarus*, *211*, 906–908.

Tyler, R. H., Maus, S., & Luhr, H. (2003). Satellite observations of magnetic fields due to ocean tidal flow. *Science*, *299*, 239–241.

Vance, S., Bouffard, M., Choukroun, M., & Sotin, C. (2014). Ganymedes internal structure including thermodynamics of magnesium sulfate oceans in contact with ice. *Planetary and Space Science*, *96*, 62–70. doi: 10.1016/j.pss.2014.03.011

Vance, S., & Brown, J. (2005). Layering and double-diffusion style convection in Europa's ocean. *Icarus*, *177*(2), 506–514.

Vance, S., & Brown, J. (2013). Thermodynamic properties of aqueous $MgSO_4$ to 800 MPa at temperatures from -20 to 100 $^o$C and concentrations to 2.5 mol kg$^{-1}$ from sound speeds, with applications to icy world oceans. *Geochimica et Cosmochimica Acta*, *110*, 176-189.

Vance, S., & Goodman, J. (2009). Europa. In R. T. P. W. B. M. Khurana (Ed.), (p. 459-482). Arizona University Press.

Vance, S. D., Hand, K. P., & Pappalardo, R. T. (2016). Geophysical controls of chemical disequilibria in Europa. *Geophysical Research Letters*, *43*(10), 4871–4879. doi: 10.1002/2016gl068547

Vance, S. D., Panning, M. P., Stähler, S., Cammarano, F., Bills, B. G., Tobie, G., ... et al. (2018). Geophysical investigations of habitability in ice-covered ocean worlds. *Journal of Geophysical Research: Planets*. doi: 10.1002/2017je005341

Vance, S. D., Tobie, G., Daswani, M. M., & Choblet, G. (2019). Tidal signatures of geochemically rigorous interior structure for Ganymede. *EPSC Abstracts*, *3*(EPSC-DPS2019), 1149-1.

Zhu, P., Manucharyan, G. E., Thompson, A. F., Goodman, J. C., & Vance, S. D. (2017). The influence of meridional ice transport on Europa's ocean stratification and heat content. *Geophysical Research Letters*, *44*(12), 5969–5977. doi: 10.1002/2017gl072996

Zimmer, C., Khurana, K. K., & Kivelson, M. G. (2000). Subsurface oceans on Europa and Callisto: Constraints from Galileo magnetometer observations. *Icarus*, *147*(2), 329–347.

Zolotov, M. (2008). Oceanic composition on europa: Constraints from mineral solubilities. In *Lunar and planetary institute science conference abstracts* (Vol. 39, p. 2349).

Zolotov, M., & Shock, E. (2001). Composition and stability of salts on the surface of Europa and their oceanic origin. *Journal of Geophysical Research*, *106*(E12), 32815–32828.

Zolotov, M. Y., & Kargel, J. (2009). On the chemical composition of Europa's icy shell, ocean, and underlying rocks. *Europa, edited by RT Pappalardo, WB McKinnon, and K. Khurana, University of Arizona Press, Tucson, AZ*, 431–458.

| **Europa** | | | Period (hr): | **5.62** | **11.23** | **85.20** |
|---|---|---|---|---|---|---|
| | | | $B_y$ (nT): | **15.03** | **209.78** | **10.65** |
| $T_b$ (K) | $\overline{T}$ (K) | $D_{\mathrm{I}}$ (km) | $D_{\mathrm{ocean}}$ (km) | | $B_y \mathcal{A}_1^e$ (nT) | |
| **Ionosphere Only** | | | | **Re Im** | **Re Im** | **Re Im** |
| Pedersen | | | | 0.001 0.104 | 0.002 0.727 | 0.000 0.005 |
| **$MgSO_4$ 1 wt%** | | | | **Re Im** | **Re Im** | **Re Im** |
| 273.1 | 273.9 | 5 | 117 | 13.641 1.527 | 184.568 38.142 | 2.942 4.479 |
| Pedersen | | | $\Delta\mathcal{A}_1^e$ (%) | 0.02 0.17 | 0.03 0.03 | 0.10 0.05 |
| $\overline{\sigma}$ = 0.4533 S/m | | | $\Delta\mathcal{A}_1^e$ (%) | 0.36 -0.41 | 0.39 -0.08 | 0.85 0.50 |
| $\sigma_{\mathrm{top}}$ = 0.4107 S/m | | | $\Delta\mathcal{A}_1^e$ (%) | 0.10 7.75 | -0.45 8.80 | -12.31 -3.57 |
| 270.4 | 271.1 | 30 | 91 | 13.054 1.917 | 172.021 49.195 | 1.680 3.611 |
| Pedersen | | | $\Delta\mathcal{A}_1^e$ (%) | 0.04 0.18 | 0.05 0.03 | 0.15 0.09 |
| $\overline{\sigma}$ = 0.4132 S/m | | | $\Delta\mathcal{A}_1^e$ (%) | 0.22 -0.10 | 0.24 0.01 | 0.55 0.34 |
| $\sigma_{\mathrm{top}}$ = 0.3847 S/m | | | $\Delta\mathcal{A}_1^e$ (%) | -0.09 6.49 | -0.88 6.09 | -10.65 -4.23 |
| **$MgSO_4$ 10 wt%** | | | | **Re Im** | **Re Im** | **Re Im** |
| 272.7 | 274.1 | 5 | 124 | 14.309 0.539 | 196.395 10.221 | 9.414 1.714 |
| Pedersen | | | $\Delta\mathcal{A}_1^e$ (%) | 0.01 0.38 | 0.00 0.16 | 0.00 0.01 |
| $\overline{\sigma}$ = 3.7646 S/m | | | $\Delta\mathcal{A}_1^e$ (%) | 0.23 -3.83 | 0.33 -2.87 | 0.49 -0.10 |
| $\sigma_{\mathrm{top}}$ = 3.3197 S/m | | | $\Delta\mathcal{A}_1^e$ (%) | -0.01 2.28 | -0.01 2.13 | -0.34 11.33 |
| 269.8 | 270.8 | 30 | 96 | 13.595 0.534 | 187.098 9.765 | 8.853 2.245 |
| Pedersen | | | $\Delta\mathcal{A}_1^e$ (%) | 0.01 0.64 | 0.01 0.27 | 0.01 0.01 |
| $\overline{\sigma}$ = 3.3661 S/m | | | $\Delta\mathcal{A}_1^e$ (%) | 0.18 -2.30 | 0.23 -1.35 | 0.30 0.02 |
| $\sigma_{\mathrm{top}}$ = 3.0763 S/m | | | $\Delta\mathcal{A}_1^e$ (%) | -0.01 1.41 | 0.08 2.77 | -0.81 7.99 |
| **Seawater 0.35165 wt%** | | | | **Re Im** | **Re Im** | **Re Im** |
| 272.5 | 273.2 | 5 | 117 | 13.567 1.744 | 181.600 44.022 | 2.299 4.139 |
| Pedersen | | | $\Delta\mathcal{A}_1^e$ (%) | 0.03 0.14 | 0.03 0.02 | 0.12 0.06 |
| $\overline{\sigma}$ = 0.3855 S/m | | | $\Delta\mathcal{A}_1^e$ (%) | 0.43 -0.30 | 0.46 -0.02 | 1.02 0.63 |
| $\sigma_{\mathrm{top}}$ = 0.3415 S/m | | | $\Delta\mathcal{A}_1^e$ (%) | 0.01 10.36 | -0.98 10.77 | -16.33 -5.92 |
| 270.0 | 270.7 | 30 | 91 | 12.983 2.139 | 168.558 54.379 | 1.368 3.324 |
| Pedersen | | | $\Delta\mathcal{A}_1^e$ (%) | 0.04 0.15 | 0.05 0.03 | 0.18 0.10 |
| $\overline{\sigma}$ = 0.3651 S/m | | | $\Delta\mathcal{A}_1^e$ (%) | 0.26 -0.07 | 0.29 0.03 | 0.65 0.42 |
| $\sigma_{\mathrm{top}}$ = 0.3339 S/m | | | $\Delta\mathcal{A}_1^e$ (%) | -0.23 8.27 | -1.49 7.33 | -13.72 -5.87 |
| **Seawater 3.5165 wt%** | | | | **Re Im** | **Re Im** | **Re Im** |
| 270.8 | 271.9 | 5 | 119 | 14.245 0.590 | 195.352 10.912 | 9.274 2.109 |
| Pedersen | | | $\Delta\mathcal{A}_1^e$ (%) | 0.01 0.36 | 0.01 0.16 | 0.00 0.00 |
| $\overline{\sigma}$ = 3.0760 S/m | | | $\Delta\mathcal{A}_1^e$ (%) | 0.24 -3.32 | 0.33 -2.24 | 0.46 -0.03 |
| $\sigma_{\mathrm{top}}$ = 2.7347 S/m | | | $\Delta\mathcal{A}_1^e$ (%) | -0.02 2.08 | 0.04 2.37 | -0.74 10.53 |
| 268.2 | 269.1 | 30 | 91 | 13.530 0.560 | 186.582 10.460 | 8.612 2.664 |
| Pedersen | | | $\Delta\mathcal{A}_1^e$ (%) | 0.01 0.63 | 0.01 0.26 | 0.01 0.00 |
| $\overline{\sigma}$ = 2.8862 S/m | | | $\Delta\mathcal{A}_1^e$ (%) | 0.18 -1.89 | 0.22 -0.95 | 0.28 0.03 |
| $\sigma_{\mathrm{top}}$ = 2.6476 S/m | | | $\Delta\mathcal{A}_1^e$ (%) | 0.01 1.46 | 0.10 3.88 | -1.26 7.23 |

Table 2: Europa: Magnetic induction field strengths {Re,Im}$(B_y\mathcal{A}_1^e)$, in nT, at the main inducing periods in Figure 1. For the different ocean compositions and thicknesses of the upper ice I lithosphere/ocean ($D_{\mathrm{I}}/D_{\mathrm{ocean}}$; Figure 5), the adiabatic response is listed first. These values are also shown in Figure 7. Following these are the deviations from the adiabatic response (in %) when including a 100 km ionosphere with Pedersen conductance of 30 S (Hartkorn & Saur, 2017), then for the ocean with uniform conductivity set to the mean of the adiabatic ocean ($\overline{\sigma}$), and then for the case with uniform conductivity set to

| **Ganymede** | | | Period (hr): | **5.27** | **10.53** | **171.57** |
|---|---|---|---|---|---|---|
| | | | $B_y$ (nT): | **2.64** | **82.61** | **1.21** |
| $T_b$ (K) | $\overline{T}$ (K) | $D_{\mathrm{I}}$ (km) | $D_{\mathrm{ocean}}$ (km) | | $B_y \mathcal{A}_1^e$ (nT) | |
| **Ionosphere Only** | | | | **Re Im** | **Re Im** | **Re Im** |
| Pedersen | | | | 0.000 0.002 | 0.000 0.033 | 0.000 0.000 |
| **$MgSO_4$ 1 wt%** | | | | **Re Im** | **Re Im** | **Re Im** |
| 270.7 | 279.0 | 25 | 442 | 2.393 0.150 | 72.835 6.420 | 0.791 0.390 |
| Pedersen | | $\Delta\mathcal{A}_1^e$ (%) | | 0.00 0.03 | 0.00 0.01 | 0.00 0.00 |
| $\overline{\sigma} = 0.5166$ S/m | | $\Delta\mathcal{A}_1^e$ (%) | | 0.87 -8.82 | 1.23 -7.04 | 2.61 1.01 |
| $\sigma_{\mathrm{top}} = 0.3890$ S/m | | $\Delta\mathcal{A}_1^e$ (%) | | -0.03 4.54 | -0.14 5.86 | -9.33 17.09 |
| 261.6 | 266.2 | 92 | 276 | 2.169 0.165 | 66.167 6.714 | 0.417 0.476 |
| Pedersen | | $\Delta\mathcal{A}_1^e$ (%) | | 0.00 0.06 | 0.00 0.03 | 0.00 0.00 |
| $\overline{\sigma} = 0.3322$ S/m | | $\Delta\mathcal{A}_1^e$ (%) | | 0.95 -5.29 | 1.18 -2.65 | 2.44 1.41 |
| $\sigma_{\mathrm{top}} = 0.2623$ S/m | | $\Delta\mathcal{A}_1^e$ (%) | | 0.08 3.83 | 0.45 10.74 | -22.82 -3.32 |
| **$MgSO_4$ 10 wt%** | | | | **Re Im** | **Re Im** | **Re Im** |
| 270.2 | 278.3 | 25 | 458 | 2.499 0.056 | 77.528 2.435 | 1.020 0.124 |
| Pedersen | | $\Delta\mathcal{A}_1^e$ (%) | | 0.00 0.04 | 0.00 0.02 | 0.00 0.00 |
| $\overline{\sigma} = 4.0699$ S/m | | $\Delta\mathcal{A}_1^e$ (%) | | 0.29 -10.57 | 0.41 -9.78 | 1.48 -3.07 |
| $\sigma_{\mathrm{top}} = 3.1150$ S/m | | $\Delta\mathcal{A}_1^e$ (%) | | -0.00 2.03 | -0.01 2.84 | -0.18 7.55 |
| 260.0 | 263.5 | 93 | 282 | 2.290 0.067 | 70.816 2.910 | 0.936 0.163 |
| Pedersen | | $\Delta\mathcal{A}_1^e$ (%) | | 0.00 0.10 | 0.00 0.04 | 0.00 0.00 |
| $\overline{\sigma} = 2.3476$ S/m | | $\Delta\mathcal{A}_1^e$ (%) | | 0.27 -7.17 | 0.38 -6.43 | 1.01 -0.28 |
| $\sigma_{\mathrm{top}} = 1.9483$ S/m | | $\Delta\mathcal{A}_1^e$ (%) | | 0.00 1.71 | -0.00 2.51 | -0.11 15.65 |
| **bottom layer: 30 km 20 S/m** | | $\Delta\mathcal{A}_1^e$ (%) | | 0.00 -0.00 | 0.00 -0.00 | -1.20 0.20 |
| Pedersen | | $\Delta\mathcal{A}_1^e$ (%) | | 0.00 0.10 | 0.00 0.04 | -1.20 0.20 |

Table 3: Ganymede: Magnetic induction field strengths {Re,Im}$(B_y \mathcal{A}_1^e)$, in nT, at the main inducing periods in Figure 1. For the different ocean compositions and thicknesses of the upper ice I lithosphere ($D_{\mathrm{I}}$; Figure 5), the adiabatic response is listed first. These values are also shown in Figure 7. Following these are deviations from the adiabatic response (in %) when including a 100 km ionosphere with Pedersen conductance of 2 S (Hartkorn & Saur, 2017), then for the ocean with uniform conductivity set to the mean of the adiabatic ocean ($\overline{\sigma}$), and then for the case with uniform conductivity set to the value at the ice–ocean interface ($\sigma_{\mathrm{top}}$). The surface responses of the ionosphere in the absence of an ocean are listed at the top of the table.

| **Callisto** | | | Period (hr): $B_y$ (nT): | **5.09** **0.25** | **10.18** **37.57** | **400.33** **1.72** |
|---|---|---|---|---|---|---|
| $T_b$ (K) | $\overline{T}$ (K) | $D_\mathrm{I}$ (km) | $D_\mathrm{ocean}$ (km) | | $B_y\mathcal{A}^e_1$ (nT) | |
| **Ionosphere Only** | | | | **Re Im** | **Re Im** | **Re Im** |
| Pedersen | | | | 0.019 0.070 | 0.769 5.549 | 0.000 0.007 |
| Cowling | | | | 0.230 0.097 | 23.854 20.120 | 0.002 0.056 |
| **$MgSO_4$ 1 wt%** | | | | **Re Im** | **Re Im** | **Re Im** |
| 257.4 | 259.6 | 99 | 132 | 0.204 0.023 | 29.774 6.332 | 0.021 0.171 |
| Pedersen | | | | 0.207 0.026 | 30.227 6.544 | 0.022 0.177 |
| Cowling | | | | 0.231 0.036 | 33.248 7.167 | 0.033 0.225 |
| $\overline{\sigma} = 0.2307$ S/m | | $\Delta\mathcal{A}^e_1$ (%) | | 0.49 -0.44 | 0.53 -0.08 | 1.45 0.96 |
| $\sigma_\mathrm{top} = 0.1965$ S/m | | $\Delta\mathcal{A}^e_1$ (%) | | 0.06 14.62 | -1.03 15.03 | -26.08 -13.62 |
| 250.8 | 250.9 | 128 | 21 | 0.060 0.095 | 2.885 9.085 | 0.000 0.012 |
| Pedersen | | | | 0.102 0.119 | 5.702 13.168 | 0.000 0.018 |
| Cowling | | | | 0.238 0.083 | 27.259 18.811 | 0.003 0.068 |
| $\overline{\sigma} = 0.0895$ S/m | | $\Delta\mathcal{A}^e_1$ (%) | | 0.04 0.02 | 0.04 0.03 | 0.05 0.03 |
| $\sigma_\mathrm{top} = 0.0874$ S/m | | $\Delta\mathcal{A}^e_1$ (%) | | -3.26 -0.99 | -4.12 -1.87 | -4.52 -2.28 |
| **$MgSO_4$ 10 wt%** | | | | **Re Im** | **Re Im** | **Re Im** |
| 255.7 | 256.9 | 99 | 130 | 0.211 0.008 | 31.391 1.533 | 0.552 0.696 |
| Pedersen | | | | 0.212 0.011 | 31.490 1.787 | 0.556 0.698 |
| Cowling | | | | 0.226 0.027 | 32.566 3.378 | 0.582 0.715 |
| $\overline{\sigma} = 1.5256$ S/m | | $\Delta\mathcal{A}^e_1$ (%) | | 0.20 -2.91 | 0.26 -1.74 | 0.69 0.39 |
| $\sigma_\mathrm{top} = 1.3789$ S/m | | $\Delta\mathcal{A}^e_1$ (%) | | 0.01 1.12 | 0.12 3.18 | -10.78 -1.59 |
| 250.8 | 250.9 | 128 | 21 | 0.195 0.053 | 24.308 13.231 | 0.003 0.067 |
| Pedersen | | | | 0.202 0.055 | 25.716 13.402 | 0.004 0.074 |
| Cowling | | | | 0.239 0.049 | 32.873 12.030 | 0.009 0.123 |
| $\overline{\sigma} = 0.6025$ S/m | | $\Delta\mathcal{A}^e_1$ (%) | | -0.00 -0.00 | -0.00 -0.00 | -0.00 -0.00 |
| $\sigma_\mathrm{top} = 0.6062$ S/m | | $\Delta\mathcal{A}^e_1$ (%) | | 0.08 -0.53 | 0.28 -0.34 | 1.23 0.61 |

Table 4: Callisto: Magnetic induction field strengths $\{\mathrm{Re,Im}\}(B_y\mathcal{A}^e_1)$, in nT, at the main inducing periods in Figure 1. For the different ocean compositions and thicknesses of the upper ice I lithosphere/ocean ($D_\mathrm{I}/D_\mathrm{ocean}$; Figure 5), the adiabatic response is listed first. These values are also shown in Figure 7. Following these are the responses (in nT) including a 100 km ionosphere with {Pedersen,Cowling} conductance of {800,6850} S (Hartkorn & Saur, 2017), then the deviations from the adiabatic response (in %) for the ocean with uniform conductivity set to the mean of the adiabatic ocean ($\overline{\sigma}$), and then for the case with uniform conductivity set to the value at the ice–ocean interface ($\sigma_\mathrm{top}$). The surface responses of the ionosphere in the absence of an ocean are listed at the top of the table.

| | $\sigma$ [S/m] | $D$ [km] | $U_r$ [m/s] | $U_\theta$ [m/s] | $U_\phi$ [m/s] | $b_r$ [nT] |
|---|---|---|---|---|---|---|
| Europa | | | | | | |
| $MgSO_4$ 1 wt%, Thicker ice shell | 0.4 | 91 | 0.06 | 0.29 | 2.9 | 1 |
| $MgSO_4$ 1 wt%, Thinner ice shell | 0.5 | 117 | 0.07 | 0.37 | 3.7 | 2 |
| $MgSO_4$ 10 wt%, Thicker ice shell | 3.4 | 96 | 0.06 | 0.30 | 3.0 | 10 |
| $MgSO_4$ 10 wt%, Thinner ice shell | 3.8 | 124 | 0.08 | 0.39 | 3.9 | 20 |
| Seawater 0.35 wt%, Thicker ice shell | 0.4 | 91 | 0.06 | 0.29 | 2.9 | 1 |
| Seawater 0.35 wt%, Thinner ice shell | 0.4 | 117 | 0.07 | 0.37 | 3.7 | 2 |
| Seawater 3.5 wt%, Thicker ice shell | 2.9 | 91 | 0.06 | 0.29 | 2.9 | 8 |
| Seawater 3.5 wt%, Thinner ice shell | 3.1 | 119 | 0.07 | 0.37 | 3.7 | 14 |
| Ganymede | | | | | | |
| $MgSO_4$ 1 wt%, Thicker ice shell | 0.3 | 276 | 0.08 | 0.41 | 4.1 | 8 |
| $MgSO_4$ 1 wt%, Thinner ice shell | 0.5 | 442 | 0.13 | 0.66 | 6.6 | 36 |
| $MgSO_4$ 10 wt%, Thicker ice shell | 2.3 | 282 | 0.08 | 0.42 | 4.2 | 65 |
| $MgSO_4$ 10 wt%, Thinner ice shell | 4.1 | 458 | 0.14 | 0.69 | 6.9 | 330 |
| Callisto | | | | | | |
| $MgSO_4$ 1 wt%, Thicker ice shell | 0.09 | 21 | 0.003 | 0.01 | 0.14 | $\ll 1$ |
| $MgSO_4$ 1 wt%, Thinner ice shell | 0.2 | 132 | 0.02 | 0.09 | 0.87 | 0.02 |
| $MgSO_4$ 10 wt%, Thicker ice shell | 0.6 | 21 | 0.002 | 0.01 | 0.12 | $\ll 1$ |
| $MgSO_4$ 10 wt%, Thinner ice shell | 1.5 | 130 | 0.02 | 0.09 | 0.86 | 0.2 |

Table 5: Ocean characteristics and upper bound estimates of the motionally induced magnetic field strengths from Equation (12) at the top of the oceans. Radial $U_r$, latitudinal $U_\theta$, and zonal $U_\phi$ flow speeds from Figure 8 with $U = \Omega D Ro$; ocean thicknesses $D$ and electrical conductivity $\sigma$ from Tables 2–4.

# Supporting Information for "Magnetic Induction Responses of Jupiter's Ocean Moons Including Effects from Adiabatic Convection"

S. D. Vance[1], B. G. Bills[1], C. J. Cochrane[1], K. M. Soderlund[2],

N. Gómez-Pérez[3], M. J. Styczinski[4], and C. Paty[5]

[1]Jet Propulsion Laboratory, California Institute of Technology, Pasadena, USA

[2]Institute for Geophysics, John A. & Katherine G. Jackson School of Geosciences, The University of Texas at Austin, USA

[3]British Geological Survey, Edinburgh, UK

[4]Dept. of Physics, University of Washington, Seattle, USA

[5]Dept. of Earth Sciences, University of Oregon, Eugene, USA

**Contents of this file**

1. Text S1 to S3
2. Figures S1 to S8
3. Tables S1 to S3

**Text S1. Induction response model**

We are interested in the magnetic fields induced within a spherically symmetric body, in which electrical conductivity is a piece-wise constant function of distance from the center. We thus assume bounding radii for $N$ layers

$$\{r_1, r_2, r_3, \cdots, r_N\} \tag{S1}$$

where

$$r_N = R \tag{S2}$$

is the outer radius of the spherical body.

The corresponding conductivity values are

$$\{\sigma_1, \sigma_2, \sigma_3, \cdots, \sigma_N\} \tag{S3}$$

We also assume that there is an imposed external magnetic potential, represented by a sum of terms, each of which has the form

$$\Phi_{n,m,p}(r,\theta,\varphi,t) = RB_e \left(\frac{r}{R}\right)^n S_{n,m}(\theta,\varphi)\mathrm{e}^{-i\omega_p t} \tag{S4}$$

where $\{r, \theta, \varphi\}$ are spherical coordinates ($r$ is radius, $\theta$ is colatitude, and $\varphi$ is longitude) of the field point, $B_e$ is a scale factor, $S_{n,m}(\theta,\varphi)$ is a surface spherical harmonic function of degree $n$ and order $m$, while $t$ is time and $\omega_p$ is the angular frequency of oscillation of the imposed potential. The same methods apply independently to each frequency $\omega_p$ in the excitation field, and the results sum linearly by superposition. Therefore, we now drop the subscript on this quantity and simply use $\omega$.

Within each layer, the magnetic field vector $\mathbf{B}$ must satisfy the Helmholtz equation

$$\nabla^2\mathbf{B} = -k^2\mathbf{B} \tag{S5}$$

which is a diffusion equation for $\mathbf{B}$. $k$ is a scalar wavenumber given by

$$k^2 = i\omega\mu_0\sigma \tag{S6}$$

where $\omega$ is angular frequency, $\sigma$ is electrical conductivity, and the magnetic constant (permeability of free space) is given by

$$\mu_0 = 4\pi \times 10^{-7} N/A^2 \tag{S7}$$

with units $N$ and $A$ being Newton and Ampere. In defining $k$ in Equation S6, we have assumed $\mu \approx \mu_0$, which holds well even for ferromagnetic materials when they are considered on a global scale (Saur et al., 2009). Note that in Equation S6, we have chosen a different convention from that of Parkinson (1983) and numerous authors relying on their derivation. We make this choice in order to derive the spherical Bessel equation (Equation S11) from the diffusion equation (5). Choosing $k^2 = -i\omega\mu_0\sigma$ results in the *modified* spherical Bessel equation, meaning the derivation in Parkinson (1983) is in error. We prefer to define $k^2$ as in Equation S6 so that we can, in fact, reach the spherical Bessel equation and thereby compare the remaining derivation favorably to that of Parkinson (1983) and other past research using the standard spherical Bessel functions.

Independently from Equation S5, the net poloidal component of the magnetic field inside the body is given by sums over $n$ and $m$ of terms with the forms

$$B_r(r,\theta,\varphi,t) = \frac{C}{r}\Big(F(r)\Big)n(n+1)\ S_{n,m}(\theta,\varphi)\mathrm{e}^{-i\omega t} \tag{S8}$$

$$B_\theta(r,\theta,\varphi,t) = \frac{C}{r}\frac{d}{dr}\Big(rF(r)\Big)\ \frac{d}{d\theta}\Big(S_{n,m}(\theta,\varphi)\Big)\mathrm{e}^{-i\omega t} \tag{S9}$$

$$B_\varphi(r,\theta,\varphi,t) = \frac{C}{r\sin\theta}\frac{d}{dr}\Big(rF(r)\Big)\ \frac{d}{d\varphi}\Big(S_{n,m}(\theta,\varphi)\Big)\mathrm{e}^{-i\omega t} \tag{S10}$$

where $C$ is a constant, and $F(r)$ is a function of radius, which we need to determine.

### S1.1 Analytical model based on Srivastava (1966)

For the purpose of validating our numerical model, we separately derive an analytical solution akin to that of Srivastava (1966) and summarized by Parkinson (1983). As this analytical approach is common throughout the literature, we later compare the analytical (layered) approach to our numerical (ordinary differential equation, ODE) approach in Figures S1 and S2. We find it instructive to compare the point in the derivation where the two approaches differ, so we carry out the full derivation here, in our notation.

Applying separation of variables to the governing differential equation (Equation S5), one finds that the radial factor $F(r)$ in the solution must satisfy the spherical Bessel equation

$$\frac{d^2F}{dr^2} + \left(\frac{2}{r}\right)\frac{dF}{dr} + \left(k^2 - \frac{n(n+1)}{r^2}\right)F = 0 \tag{S11}$$

This is a second-order equation, having two solutions, $j_n(kr)$ and $y_n(kr)$, the spherical Bessel functions of the first and second kind, respectively, of degree $n$ and argument $kr$.

Note that choosing to define $k$ as we did in Equation S6 was a strict requirement to obtain Equation S11. If we instead chose $k^2 = -i\omega\mu_o\sigma$, we would have obtained the *modified* spherical Bessel equation

$$\frac{d^2F}{dr^2} + \left(\frac{2}{r}\right)\frac{dF}{dr} + \left(-k^2 - \frac{n(n+1)}{r^2}\right)F = 0 \tag{S12}$$

with solutions $i_n(kr)$ and $k_n(kr)$, the *modified* spherical Bessel functions, as in Schilling et al. (2007) and ? (?). In effect, our choice of sign convention results in the complex response we later derive $\mathcal{A}_n^e$ (Equation S46) being equal to the complex conjugate of the analogous quantity $Ae^{i\phi}$ appearing in past research (e.g., Zimmer et al., 2000).

It will also be convenient to define another set of related functions

$$F^\star(r) = \frac{d}{dr}\Big(rF(r)\Big) \tag{S13}$$

with

$$\begin{aligned} j_n^\star(kr) &= \frac{d}{dr}\Big(rj_n(kr)\Big) \\ &= (n+1)j_n(kr) - kr\, j_{n+1}(kr) \end{aligned} \tag{S14}$$

and

$$\begin{aligned} y_n^\star(kr) &= \frac{d}{dr}\Big(ry_n(kr)\Big) \\ &= (n+1)y_n(kr) - kr\, y_{n+1}(kr) \end{aligned} \tag{S15}$$

Both $y_n$ and $y_n^\star$ are singular at the origin $r = 0$, so in the innermost spherical layer only $j_n(kr)$ and $j_n^\star(kr)$ may describe physically consistent solutions. In other layers, we use linear combinations of $j_n$ and $y_n$ and linear combinations of $j_n^\star$ and $y_n^\star$.

**Text S1.1.1. Internal boundary conditions**

The resulting piecewise-defined radial functions characterize the radial part of the magnetic field. The radial component has the form

$$F_n(r) = \begin{cases} c_1 j_n(k_1 r) & \text{for} \quad 0 < r \leq r_1 \\ c_2 j_n(k_2 r) \ + d_2 y_n(k_2 r) & \text{for} \quad r_1 < r \leq r_2 \\ c_3 j_n(k_3 r) \ + d_3 y_n(k_3 r) & \text{for} \quad r_2 < r \leq r_3 \\ & \\ c_\mathrm{j} j_n(k_\mathrm{j} r) \ + d_\mathrm{j} y_n(k_\mathrm{j} r) & \text{for} \quad r_{\mathrm{j}-1} < r \leq r_\mathrm{j} \end{cases} \tag{S16}$$

The tangential components yield similar structure, but with all $F_n$, $j_n$, and $y_n$ replaced by their starred counterparts.

The constants $c_\mathrm{j}$ and $d_\mathrm{j}$ are determined by continuity of radial ($r$) and tangential ($\theta, \varphi$) components of the magnetic field across the boundaries. For each internal boundary, it must hold that

$$F_n^{\text{below}}(r_\mathrm{j}) = F_n^{\text{above}}(r_\mathrm{j})$$

$$c_\mathrm{j} j_n(k_\mathrm{j} r_\mathrm{j}) + d_\mathrm{j} y_n(k_\mathrm{j} r_\mathrm{j}) = c_{\mathrm{j}+1} j_n(k_{\mathrm{j}+1} r_\mathrm{j}) + d_{\mathrm{j}+1} y_n(k_{\mathrm{j}+1} r_\mathrm{j}) \tag{S17}$$

to ensure continuity of the radial component of the magnetic field, and likewise for $F_n^\star$ to ensure continuity of the tangential components. These continuity constraints yield two equations at each internal boundary, from which we can determine the layer coefficients.

The internal boundary conditions are only part of the story. In a model with $N$ layers, we have $2N - 1$ coefficients to determine (recall that $d_1 = 0$, to avoid singular behavior at the origin), but only $N - 1$ internal boundaries, and thus only $2N - 2$ constraints. The external boundary condition provides the additional information to make the problem evenly determined.

Using notation similar to that of Parkinson (1983, Ch. 5), we can write a recursion relation that transforms the coefficients in the $\mathrm{j}^{\mathrm{th}}$ layer into those for the layer above it

$$\begin{bmatrix} c_{\mathrm{j}+1} \\ d_{\mathrm{j}+1} \end{bmatrix} = T_{\mathrm{j}}(k_{\mathrm{j}}, k_{\mathrm{j}+1}, r_{\mathrm{j}}) \cdot \begin{bmatrix} c_{\mathrm{j}} \\ d_{\mathrm{j}} \end{bmatrix} \tag{S18}$$

where the transformation matrix $T_{\mathrm{j}}$ has elements

$$T_{\mathrm{j}}(k_{\mathrm{j}}, k_{\mathrm{j}+1}, r_{\mathrm{j}}) = \frac{1}{\alpha_{\mathrm{j}}} \begin{bmatrix} \beta_{\mathrm{j}} & \gamma_{\mathrm{j}} \\ \delta_{\mathrm{j}} & \varepsilon_{\mathrm{j}} \end{bmatrix} \tag{S19}$$

with

$$\alpha_{\mathrm{j}} = j_n(k_{\mathrm{j}+1} r_{\mathrm{j}})\, y_n^{\star}(k_{\mathrm{j}+1} r_{\mathrm{j}}) - y_n(k_{\mathrm{j}+1} r_{\mathrm{j}})\, j_n^{\star}(k_{\mathrm{j}+1} r_{\mathrm{j}}) = \frac{1}{k_{\mathrm{j}+1} r_{\mathrm{j}}} \tag{S20}$$

which is a function of the conductivity in the layer above the boundary only. The other elements depend on the conductivities on both sides of the boundary:

$$\beta_{\mathrm{j}} = j_n(k_{\mathrm{j}} r_{\mathrm{j}})\, y_n^{\star}(k_{\mathrm{j}+1} r_{\mathrm{j}}) - y_n(k_{\mathrm{j}+1} r_{\mathrm{j}})\, j_n^{\star}(k_{\mathrm{j}} r_{\mathrm{j}}) \tag{S21}$$

$$\gamma_{\mathrm{j}} = y_n(k_{\mathrm{j}} r_{\mathrm{j}})\, y_n^{\star}(k_{\mathrm{j}+1} r_{\mathrm{j}}) - y_n(k_{\mathrm{j}+1} r_{\mathrm{j}})\, y_n^{\star}(k_{\mathrm{j}} r_{\mathrm{j}}) \tag{S22}$$

and

$$\delta_{\mathrm{j}} = j_n(k_{\mathrm{j}+1} r_{\mathrm{j}})\, j_n^{\star}(k_{\mathrm{j}} r_{\mathrm{j}}) - j_n(k_{\mathrm{j}} r_{\mathrm{j}})\, j_n^{\star}(k_{\mathrm{j}+1} r_{\mathrm{j}}) \tag{S23}$$

$$\varepsilon_{\mathrm{j}} = j_n(k_{\mathrm{j}+1} r_{\mathrm{j}})\, y_n^{\star}(k_{\mathrm{j}} r_{\mathrm{j}}) - y_n(k_{\mathrm{j}} r_{\mathrm{j}})\, j_n^{\star}(k_{\mathrm{j}+1} r_{\mathrm{j}}) \tag{S24}$$

For computation, it is helpful to note that Equation S18 yields a convenient recursion relation if we define a quantity

$$\Lambda_{\mathrm{j}} = \frac{d_{\mathrm{j}}}{c_{\mathrm{j}}} \tag{S25}$$

We find that $\Lambda_{\mathrm{j}+1}$ relates to $\Lambda_{\mathrm{j}}$ by

$$\Lambda_{\mathrm{j}+1} = \frac{\delta_{\mathrm{j}} + \Lambda_{\mathrm{j}} \varepsilon_{\mathrm{j}}}{\beta_{\mathrm{j}} + \Lambda_{\mathrm{j}} \gamma_{\mathrm{j}}} \tag{S26}$$

As $d_1 = 0$, $\Lambda_1 = 0$ also for that innermost layer. Note that we define this transfer coefficient differently than do Parkinson (1983). They define the reciprocal of $\Lambda$ so that Equations S26 and S40 appear to match. Our notation allows for $\Lambda_1 = 0$, rather than leaving this quantity undefined (Styczinski et al., *in progress*).

We thus start in the central spherical layer, where $\Lambda_1 = 0$, then propagate upward through the stack of layers until we have the coefficient $\Lambda_N$ for the outermost ($N^{\text{th}}$) layer. With a piecewise model interior structure $\sigma(r)$, we compute $k_{\mathrm{j}}$ for the set of $r_{\mathrm{j}}$. Repeated application of Equation S26 then allows us to relate the interior structure to the external boundary conditions.

**Text S1.1.2. External boundary conditions**

The final step is matching the external surface boundary condition. Outside the sphere, the magnetic field is represented by a scalar potential which is the sum of an imposed external contribution and an induced internal contribution. That sum has spatial dependence given by the form

$$\Phi(r,\theta,\varphi) = R\left(B_e\left(\frac{r}{R}\right)^n + B_i\left(\frac{R}{r}\right)^{n+1}\right)S_n(\theta,\varphi) \tag{S27}$$

We have now dropped the subscript $m$ from $S_{n,m}$ because for any $n$, a suitable choice of axes results in $m = 0$ for both external and internal fields for the case of spherical symmetry we consider here. The vector field is obtained from the potential via

$$\mathbf{B} = -\nabla\Phi \tag{S28}$$

The radial component of the vector field, evaluated at the surface ($r = R$), is

$$B_r = -\Big(nB_e - (n+1)B_i\Big)S_n(\theta,\varphi) \tag{S29}$$

and the tangential components are

$$B_\theta = -\Big(B_e + B_i\Big)\frac{\partial S_n(\theta,\varphi)}{\partial\theta} \tag{S30}$$

and

$$B_\varphi = -\Big(B_e + B_i\Big)\frac{1}{\sin\theta}\frac{\partial S_n(\theta,\varphi)}{\partial\varphi} \tag{S31}$$

The $\theta$ and $\varphi$ equations yield redundant information, so we consider only the $\theta$ equation for the tangential components.

Matching these with the corresponding interior components, as given in Equations S8–S10, but evaluated at the top of the uppermost layer, we obtain

$$-\Big(nB_e - (n+1)B_i\Big)R = n(n+1)\Big(c_N j_n(k_N R) + d_N y_n(k_N R)\Big) \tag{S32}$$

and

$$-\Big(B_e + B_i\Big)R = \Big(c_N j_n^\star(k_N R) + d_N y_n^\star(k_N R)\Big) \tag{S33}$$

From these two equations, we can relate the "$Q$ response"

$$Q = \frac{B_i}{B_e} \tag{S34}$$

to the internal field coefficients:

$$Q = \frac{n}{n+1}\,\frac{c_N\beta_n + d_N\gamma_n}{c_N\delta_n + d_N\varepsilon_n} \tag{S35}$$

We define the parameters $\beta_n$, $\gamma_n$, $\delta_n$, and $\varepsilon_n$ by

$$\beta_n \;=\; j_n^\star(k_N R) - (n+1)j_n(k_N R) \tag{S36}$$

$$\gamma_n \;=\; y_n^\star(k_N R) - (n+1)y_n(k_N R) \tag{S37}$$

and

$$\delta_n \;=\; nj_n(k_N R) + j_n^\star(k_N R) \tag{S38}$$

$$\varepsilon_n \;=\; ny_n(k_N R) + j_n^\star(k_N R) \tag{S39}$$

Note that we define these quantities as above for consistency with Parkinson (1983) and for similarity between the definitions of the transfer coefficients $\Lambda_{\mathrm{j}}$ described above and $\mathcal{A}_n^e$ described below. Also note that although they both relate Bessel functions of argument $kr$, Equations S36–S39 differ substantially from Equations S21–S24.

Following the approach of Styczinski et al. (*in progress*), we now define a final recursion quantity, the complex response to the excitation field $\mathcal{A}_n^e$ as

$$\mathcal{A}_n^e = \frac{\beta_n + \Lambda_N \gamma_n}{\delta_n + \Lambda_N \varepsilon_n} \tag{S40}$$

This normalized, complex amplitude has the desirable characteristic that it is asymptotic to $(1+0i)$ for a highly conducting ocean with no ice shell, for any degree $n$ in the excitation field. Therefore, with the recursion relation from Equation S26, $\mathcal{A}_n^e$ is a readily calculable measure of the effectiveness of a body at behaving as a perfect conductor, and can easily be compared to spacecraft data fit to induced magnetic moments of any order $n$.

For the special case of a single, uniform conducting layer representing a saline ocean, the complex response evaluates to

$$\mathcal{A}_n^e = \frac{j_{n+1}(ka)y_{n+1}(ks) - j_{n+1}(ks)y_{n+1}(ka)}{j_{n+1}(ks)y_{n-1}(ka) - j_{n-1}(ka)y_{n+1}(ks)} \tag{S41}$$

with $a$ the radius of the ocean outer boundary, $s$ the radius of the ocean inner boundary, and $k = \sqrt{i\omega\mu_0\sigma}$ with $\sigma$ the conductivity of the ocean layer. $a = R - h$, where $h$ is the ice shell thickness, and $s = a - D$, where $D$ is the ocean thickness. This result is analogous to the three-layer model of Zimmer et al. (2000). All past studies have considered a uniform excitation field, with $n = 1$; comparison with past work is made by evaluating $A = |\mathcal{A}_1^e|$ and $\phi = -\arg(\mathcal{A}_1^e)$.

**Text S1.2 Numerical approximation to external boundary conditions**

We now detail our alternative numerical approach, based on that of Eckhardt (1963). Returning to Equation S11 (the Bessel equation), if instead of solving for the basis functions directly, we make the substitution

$$\frac{dF(r)}{dr} = F(r)G(r) \tag{S42}$$

where $G(r)$ is another arbitrary function of $r$, we obtain a Riccati equation for $G$:

$$\frac{d}{dr}\left(r^2 G\right) + r^2 G^2 + k^2 r^2 - n(n+1) = 0 \tag{S43}$$

Note that we have not made any assumptions about $k(r)$ in reaching Equation S43.

We can now exploit the external boundary conditions to obtain a new equation. In Equations S32 and S33, on the right-hand side we insert the more general expressions from Equations S8–S10 using the above substitution for $F(r)$. Solving for the $Q$ response as in Equation S34, we obtain

$$Q = \frac{n}{n+1}\frac{rG - n}{rG + n + 1} \tag{S44}$$

Taking $dQ/dr$ and making substitutions from Equation S43, we reach an ODE for $Q$ that may be solved numerically:

$$\frac{dQ}{dr} = -\frac{k^2 r(n+1)}{(2n+1)n}\left(Q - \frac{n}{n+1}\right)^2 - \frac{2n+1}{r}Q \tag{S45}$$

$\mathcal{A}_n^e$ may then be found by

$$\mathcal{A}_n^e = \frac{n+1}{n}Q \tag{S46}$$

as can be seen from comparing Equations S35 and S40.

**Text S1.3 Application of induced response functions**

As applied to the Galilean moons, the primary case of interest in the magnetic induction problem is for an imposed field that is effectively uniform, where $n = 1$. The analysis contained in this work makes the approximation that the magnetic field applied to the Galilean moons is entirely spatially uniform, with $n = 1$. The higher-order components applied to the moons are small, mostly deriving from oscillations in the plasma at much higher frequencies than Jupiter's primary field (Schilling et al., 2007). In this case, expressing the complex quantity $\mathcal{A}_1^e$ in terms of a magnitude $A$ and phase delay $\phi$ permits a direct comparison to work by other authors (e.g., Zimmer et al., 2000):

$$\mathcal{A}_1^e = Ae^{-i\phi} \tag{S47}$$

The negative exponent in Equation S47 is ultimately the result of an error in Parkinson (1983) propagated in the many past studies applying the results from that text. Our choice of sign convention for $k$ as the complex conjugate of that chosen by Parkinson (1983), a necessary condition for deriving the spherical Bessel equation, causes our result for the complex amplitude $\mathcal{A}_1^e$ to be equal to the complex conjugate of the analogous quantity from Zimmer et al. (2000), $Ae^{i\phi}$. This merely negates the phase of this quantity, as $A$ and $\phi$ are both real-valued. By defining $A$ and $\phi$ as in Equation S47, we can use them exactly as in past work to evaluate the internally generated, induced magnetic field outside the moon $\mathbf{B}_{\text{int,moon}}$ by

$$\mathbf{B}_{\text{int,moon}} = -Ae^{-i(\omega t - \phi)} \frac{B_e}{2} \frac{3\cos\theta\hat{r} - \hat{z}}{r^3} \tag{S48}$$

where $\hat{z}$ is directed along the instantaneous vector of the time-varying external magnetic field $\mathbf{B}_{\text{ext,moon}}$ applied to the moon, $\theta$ is the angle between $\hat{z}$ and the measurement point at $\mathbf{r} = r\hat{r}$, the origin is centered on the body to which the excitation field is applied, and the factor of 2 in Equation S48 results from inserting $n = 1$ into the factor $n/(n + 1)$ in Equation S35. Note that Equation S48 only applies in the space outside the moon.

Figures 2–4, 6, and 7 in the main text were produced using the Eckhardt (1963)-based numerical technique. Figure 6 plots $A = |\mathcal{A}_1^e|$ and $\phi = -\arg(\mathcal{A}_1^e)$ for Europa, Ganymede, and Callisto. Figures 2–4 plot the same phase delay $\phi$, but scale the amplitude $A$ to the maximum induced magnetic field that would be measured at a surface point. This occurs where the time-varying external field from Jupiter is instantaneously directed vertically into or out of the surface ($\theta = 0$ or $\pi$, $r = R$, and $\hat{r} = \pm\hat{z}$ in Equation S48). These conditions happen at key locations on the bodies' surfaces twice per period (once outward, once inward), and are not in general collocated for the various excitation frequencies. For example, for Europa's synodic period with Jupiter at 11.23 hr, the key points on the surface are the sub- and anti-jovian points, because the maximum oscillation is along the europacentric (E$\phi\Omega$) $\hat{y}$ direction. In contrast, at Europa's orbital period of 85.23 hr, the greatest oscillation is aligned with the E$\phi\Omega$ $\hat{z}$ direction, so the largest induced field will occur at the north and south spin poles. However, all of Figures 2–4, 7 scale to the $B_y$ oscillation for ease of interpretation, and therefore describe the oscillation along the vertical at the surface at the sub- and anti-jovian points for each body.

Figures S1 and S2 show a benchmarking calculation comparing the ODE approach to the stacked layer approach. For sufficiently stringent numerical solution parameters, the two approaches yield effectively identical results. Furthermore, the ODE approach has a distinct advantage in computation time for our implementation. The stacked layer approach requires explicit calculation of many Bessel functions for the layer coefficients at closely spaced points. The results of these functions very nearly cancel, so they must be evaluated at enormously high precision. Sometimes over 200 digits of precision are required to evaluate interior models relevant to the Galilean moons, requiring special computation packages and ample computation time.

The ODE approach, in contrast, converges faster for more closely spaced layers, which create a smoother function to evaluate. Thus, in practice we evaluate a comparable result that takes a small fraction of the time to compute for a highly detailed interior structure model. Use of the ODE approach to reduce computation time for detailed interior models enables massively parallel statistical studies, such as Monte Carlo methods, to explore large parameter spaces in reasonable time scales. In future work, we intend to apply such methods to better constrain the interior structures of the Galilean moons and other moons, with current and future measurements.

**Text S1.6 Comparison of adiabatic ocean profiles to uniformly conducting oceans**

In Section 2 of this work (main text), we focus on the observable signal from depth-dependent effects that shift the conductivity away from a nominal mean value. All past work studying magnetic induction of satellite oceans has assumed the ocean to be a single layer of uniform conductivity and calculated the induced field using the approach of Srivastava (1966). For comparison to this body of literature, we plot the difference in induced field from our approach to the uniform conductivity approach in Figures S3–S5. In each of these figures, the top panels compare our adiabatic ocean approach to a uniform conductivity that is consistent with the mean value from the corresponding adiabatic profile; the bottom panels compare our approach against a uniform conductivity taken to be the value from our model at the uppermost ice–ocean boundary. In most cases, the differences are near a few percent for the longer periods considered (red lines).

**Text S2. Motional Induction Response Model**

The magnetic induction equation can be used to estimate the components of the magnetic field $\mathbf{B}$ induced by ocean currents with velocity $\mathbf{u}$ and those arising from changes in the externally imposed field:

$$\frac{\partial \mathbf{B}}{\partial t} = \nabla \times (\mathbf{u} \times \mathbf{B}) - \nabla \times (\eta \nabla \times \mathbf{B}) \tag{S49}$$

where $\eta = (\mu_0 \sigma)^{-1}$ is the magnetic diffusivity. Here, the first term represents the evolution of the magnetic field, the second term represents magnetic induction, and the third term represents magnetic diffusion.

Neglecting variations in oceanic electrical conductivity with depth and assuming an incompressible fluid, Equation S49 simplifies to

$$\frac{\partial \mathbf{B}}{\partial t} = (\mathbf{B} \cdot \nabla)\mathbf{u} - (\mathbf{u} \cdot \nabla)\mathbf{B} + \eta \nabla^2 \mathbf{B}, \tag{S50}$$

after also expanding the induction term and utilizing $\nabla \cdot \mathbf{B} = 0$ and $\nabla \cdot \mathbf{u} = 0$. Let us decompose the total magnetic field into the background imposed field $\mathbf{B}_o$ and the satellite's induced field $\mathbf{b}$:

$$\mathbf{B} = \mathbf{B}_o + \mathbf{b} \tag{S51}$$

with $|\mathbf{B}_o| \gg |\mathbf{b}|$. The induction equation then becomes

$$\frac{\partial \mathbf{b}}{\partial t} = -\frac{\partial \mathbf{B}_o}{\partial t} + (\mathbf{B}_o \cdot \nabla)\mathbf{u} - (\mathbf{u} \cdot \nabla)(\mathbf{B}_o + \mathbf{b}) + \eta \nabla^2 (\mathbf{B}_o + \mathbf{b}) \tag{S52}$$

Here, the first term is the evolution of the induced magnetic field, the second term is induction due to variations in Jupiter's (or Ganymede's) intrinsic magnetic field, the third term is induction due to oceanic fluid motions, the fourth and fifth terms are advection of the fields by ocean flows, and the sixth and seventh terms are diffusion of the jovian and induced fields.

Let us next assume that the background field can be approximated by $\mathbf{B}_o = B_o\hat{z}$, where $B_o$ is constant and homogeneous and $\hat{z}$ is aligned with the rotation axis, in which case Equation S52 further simplifies to:

$$\frac{\partial \mathbf{b}}{\partial t} = B_o \frac{\partial \mathbf{u}}{\partial z} - (\mathbf{u} \cdot \nabla)\mathbf{b} + \eta \nabla^2 \mathbf{b}. \tag{S53}$$

We will also focus on the quasi-steady induction signal generated by ocean flows rather than the rapidly varying contribution that could be difficult to distinguish from other magnetic field perturbations. Towards this end, the induced magnetic field and velocity fields are decomposed into mean and fluctuating components: $\mathbf{b} = \overline{\mathbf{b}} + \mathbf{b}'$ and $\mathbf{u} = \overline{\mathbf{u}} + \mathbf{u}'$. Inserting this into Equation S53 and using Reynolds averaging yields

$$\frac{\partial \overline{\mathbf{b}}}{\partial t} = B_o \frac{\partial \overline{\mathbf{u}}}{\partial z} - (\overline{\mathbf{u}} \cdot \nabla)\overline{\mathbf{b}} - \overline{(\mathbf{u}' \cdot \nabla)\mathbf{b}'} + \eta \nabla^2 \overline{\mathbf{b}}. \tag{S54}$$

Next, we focus on the radial and latitudinal components because the zonal flow ($\overline{u}_\phi$) is nearly invariant in the $z$-direction (Figure 8a), noting also that azimuthally oriented (toroidal) magnetic fields would not be detectable by spacecraft:

$$\frac{\partial \overline{b}_r}{\partial t} = B_o \frac{\partial \overline{u}_r}{\partial z} - (\overline{\mathbf{u}} \cdot \nabla)\overline{b}_r - \overline{(\mathbf{u}' \cdot \nabla)b'_r} + \eta \nabla^2 \overline{b}_r \tag{S55}$$

$$\frac{\partial \overline{b}_\theta}{\partial t} = B_o \frac{\partial \overline{u}_\theta}{\partial z} - (\overline{\mathbf{u}} \cdot \nabla)\overline{b}_\theta - \overline{(\mathbf{u}' \cdot \nabla)b'_\theta} + \eta \nabla^2 \overline{b}_\theta \tag{S56}$$

Using simple scaling arguments, the second and third terms on the right sides are likely small compared to the first term since $|B_o| \gg |b|$ (assuming similar characteristic flow speeds and length scales) such that

$$\frac{\partial \overline{b}_r}{\partial t} \approx B_o \frac{\partial \overline{u}_r}{\partial z} + \eta \nabla^2 \overline{b}_r \tag{S57}$$

$$\frac{\partial \overline{b}_\theta}{\partial t} \approx B_o \frac{\partial \overline{u}_\theta}{\partial z} + \eta \nabla^2 \overline{b}_\theta. \tag{S58}$$

Considering the poloidal flow components (Figure 8b-c), the induced fields would likely be strongest near the equator where large vertical gradients in the convective flows exist.

In the steady-state limit and approximating the gradient length scales as $D$ and flow speeds as $U_r$ and $U_\theta$, an upper bound on magnetic fields induced by ocean currents can be estimated as:

$$\frac{B_o U_r}{D} \sim \frac{\eta b_r}{D^2}, \text{ such that } b_r \sim \frac{B_o U_r D}{\eta} = \mu_o \sigma D U_r B_o \tag{S59}$$

$$\frac{B_o U_\theta}{D} \sim \frac{\eta b_\theta}{D^2}, \text{ such that } b_\theta \sim \frac{B_o U_\theta D}{\eta} = \mu_o \sigma D U_\theta B_o. \tag{S60}$$

Here, we neglect the coupling between $b_r$ and $b_\theta$ to effectively estimate maximum values for each component.

Several aspects regarding the velocity field should also be mentioned. First, the oceans are assumed to be in a convective regime that is weakly constrained by rotation following Soderlund (2019). Soderlund19 also notes, however, that a stronger rotational influence may be possible, which would lead to slower flow speeds and weaker induced magnetic fields. In addition, it is possible that the models overestimate the meridional circulations relative to the zonal flows compared to what might be expected in the satellites (e.g., Jones & Kuzanyan, 2009). Because our approach focuses on upper bound estimates, the results are still valid if meridional circulations within the oceans are weaker than those modeled. Finally, flows due to libration, precession, tides, and electromagnetic pumping (e.g., Le Bars et al., 2015; Gissinger & Petitdemange, 2019; Soderlund et al., 2020) are neglected here but may interact with the convective flows to change their configurations and/or speeds.

**Text S3. Interior Structure Models**

The interior structures and associated electrical conductivities used in this work are computed with the PlanetProfile package described by Vance et al. (2018). PlanetProfile employs self-consistent thermodynamics for the properties of ice, fluids, rock, and metals to compute the radial structure of an ocean world. Inputs are the surface temperature and bottom melting temperature of the ice, $T_o$ and $T_b$; density of the rocky interior and any metallic core, $\rho_{\mathrm{mantle}}$ and $\rho_{\mathrm{core}}$; salinity of the ocean, $w$; and gravitational moment of inertia, $C/MR^2$. For this work, the values for these properties are substantially the same as those used by Vance et al. (2018), with a few minor changes that do not significantly change the ocean thickness and electrical conductivity that are central to this work.

Properties of ice are now computed using the SeaFreeze package (Journaux et al., 2020), which provides substantial improvements in accuracy for conditions relevant to icy moon interiors. Solid-state convection in the surface ice I layer has been corrected from Vance et al. (2018) to use the thermal upper boundary layer thickness, $e_{\mathrm{th}}$, from Deschamps and Sotin (2001) rather than the mechanical thickness, $e_{\mathrm{mech}}$. Properties of the rocky mantle and metallic core for Europa are based on updated mineralogies described by Vance and Melwani Daswani (2020). The silicate mantle composition is that of the *MC-Scale* model, an aggregate of type CM and CI chondrite compositions, and the composition of comet 67P. The core composition is a Fe–FeS mixture containing 5 wt% sulfur. Sulfur is appropriately partitioned between the mantle and core to preserve bulk planetary distribution of sulfur in the *MC-Scale* model. This approach does not account for the addition of sulfur to the ocean, which makes up 2.6% of the ocean's mass for the 10 wt% $MgSO_4$ case.

The effect of this minor inconsistency on the thickness of the ocean is smaller than the few-km variation in ocean thicknesses between the different ocean compositions (Table 1).

Using the moment of inertia along with supposed core and mantle densities to inform the construction of interior models effectively fixes the hydrosphere thickness. For example, for Europa we use the mean value from Anderson et al. (1998) of $C/MR^2 = 0.346 \pm 0.005$. The error bars in this result, combined with the assumed densities of the different radial layers, provide the canonical range of hydrosphere thicknesses of 80–170 km. Our choice of the fixed value of 0.346, and the fixed core and mantle density, create the ocean+ice hydrosphere thickness of about 125 km. This applies to all interior structures considered for this body. The near-fixed hydrosphere thicknesses are evident in the positions of the filled circles in Figure 5. Note that the interior structures we infer from moments of inertia restrict the realistic parameter space in Figures 2–4 to be a narrow region near the top of each contour plot. This is demonstrated in Figures S8–S10, wherein the studied models are marked on the contours from Figures 2–4.

The discrete layers in PlanetProfile are in sufficient number to provide step transitions between layers that are smaller than 1 km in the hydrospheres and smaller than a few km in the deeper interior. For example, the Europa models used here employ 200 steps in the ice, 350 steps in the ocean, 500 steps in the silicate layer, and 10 steps in the core. Similar scalings are used for Ganymede and Callisto in proportion to their thicker oceans and ice layers.

## References

Anderson, J., Schubert, G., Jacobson, R., Lau, E., Moore, W., & Sjogren, W. (1998). Europa's differentiated internal structure: inferences from four Galileo encounters.

*Science*, *281*(5385), 2019 - 2022.

Deschamps, F., & Sotin, C. (2001). Thermal convection in the outer shell of large icy satellites. *Journal of Geophysical Research: Planets*, *106*(E3), 5107–5121. doi: 10.1029/2000je001253

Eckhardt, D. H. (1963). Geomagnetic induction in a concentrically stratified earth. *Journal of Geophysical Research*, *68*(23), 6273–6278. doi: 10.1029/jz068i023p06273

Gissinger, C., & Petitdemange, L. (2019). A magnetically driven equatorial jet in Europa's ocean. *Nature Astron.*, *1*.

Hartkorn, O., & Saur, J. (2017). Induction signals from Callisto's ionosphere and their implications on a possible subsurface ocean. *Journal of Geophysical Research: Space Physics*, *122*(11), 11,677–11,697. doi: 10.1002/2017ja024269

Jones, C. A., & Kuzanyan, K. M. (2009). Compressible convection in the deep atmospheres of giant planets. *Icarus*, *358*, 873–897.

Journaux, B., Brown, J., Pakhomova, A., Collings, I., Petitgirard, S., Espinoza, P., ... et al. (2020). Holistic approach for studying planetary hydrospheres: Gibbs representation of ices thermodynamics, elasticity and the water phase diagram to 2300 MPa. *Journal of Geophysical Research: Planets*, *125*, e2019JE006176. doi: 10.1029/2019je006176

Le Bars, M., Cebron, D., & Le Gal, P. (2015). Flows driven by libration, precession, and tides. *Annu. Rev. Fluid Mech.*, *47*, 163–193.

Parkinson, W. (1983). *Introduction to geomagnetism.* Scottish Academic Press (Edinburgh).

Saur, J., Neubauer, F. M., & Glassmeier, K.-H. (2009). Induced magnetic fields in solar system bodies. *Space Science Reviews*, *152*(1-4), 391–421. doi: 10.1007/s11214-009-9581-y

Schilling, N., Neubauer, F. M., & Saur, J. (2007). Time-varying interaction of europa with the jovian magnetosphere: Constraints on the conductivity of Europa's subsurface ocean. *Icarus*, *192*(1), 41–55.

Soderlund, K. M. (2019). Ocean dynamics of outer solar system satellites. *Geophys. Res. Lett.*, https://doi.org/10.1029/2018GL081880.

Soderlund, K. M., Kalousová, K., Buffo, J. J., Glein, C. R., Goodman, J. C., Mitri, G., ... others (2020). Ice-ocean exchange processes in the jovian and saturnian satellites. *Space Science Reviews*, *216*(5), 1–57.

Srivastava, S. P. (1966). Theory of the magnetotelluric method for a spherical conductor. *Geophysical Journal International*, *11*(4), 373–387. doi: 10.1111/j.1365-246x.1966.tb03090.x

Vance, S. D., & Melwani Daswani, M. (2020). Serpentinite and the search for life beyond Earth. *Phil. Trans. R. Soc. A*, *378*(2165), 20180421.

Vance, S. D., Panning, M. P., Stähler, S., Cammarano, F., Bills, B. G., Tobie, G., ... et al. (2018). Geophysical investigations of habitability in ice-covered ocean worlds. *Journal of Geophysical Research: Planets*. doi: 10.1002/2017je005341

Zimmer, C., Khurana, K. K., & Kivelson, M. G. (2000). Subsurface oceans on Europa and Callisto: Constraints from Galileo magnetometer observations. *Icarus*, *147*(2), 329–347.

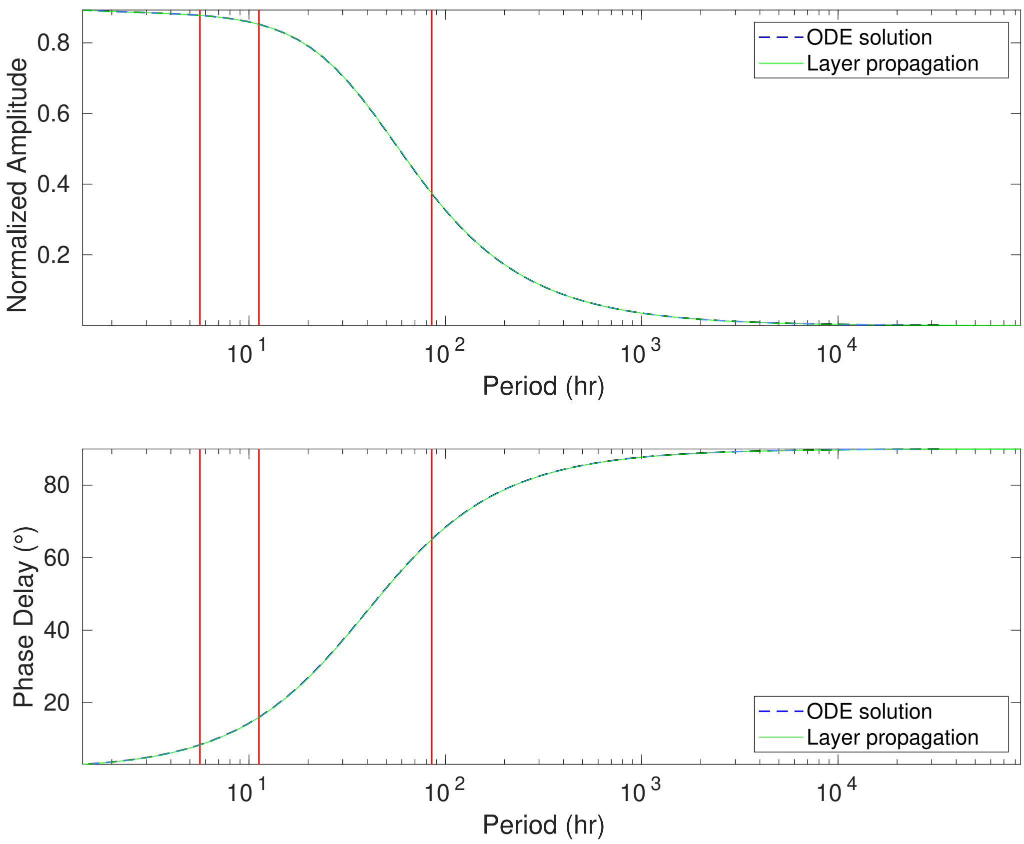


**Figure S1.** Comparison of the complex response $\mathcal{A}_1^e$ for the uniform field case, calculated by two different methods. The amplitude $A = |\mathcal{A}_1^e|$ and phase delay $\phi = -\arg(\mathcal{A}_1^e)$ are plotted separately. The Srivastava (1966) layered conductor approach common in the literature is plotted as a blue dashed line and the Eckhardt (1963) ODE approach we use in our analysis is plotted in as a solid green line. For sufficiently stringent numerical solution parameters, the lines are effectively identical. A numerically challenging example case was selected for this comparison: a Europa model of approx. 150 layers and a 1 wt% $MgSO_4$ ocean.

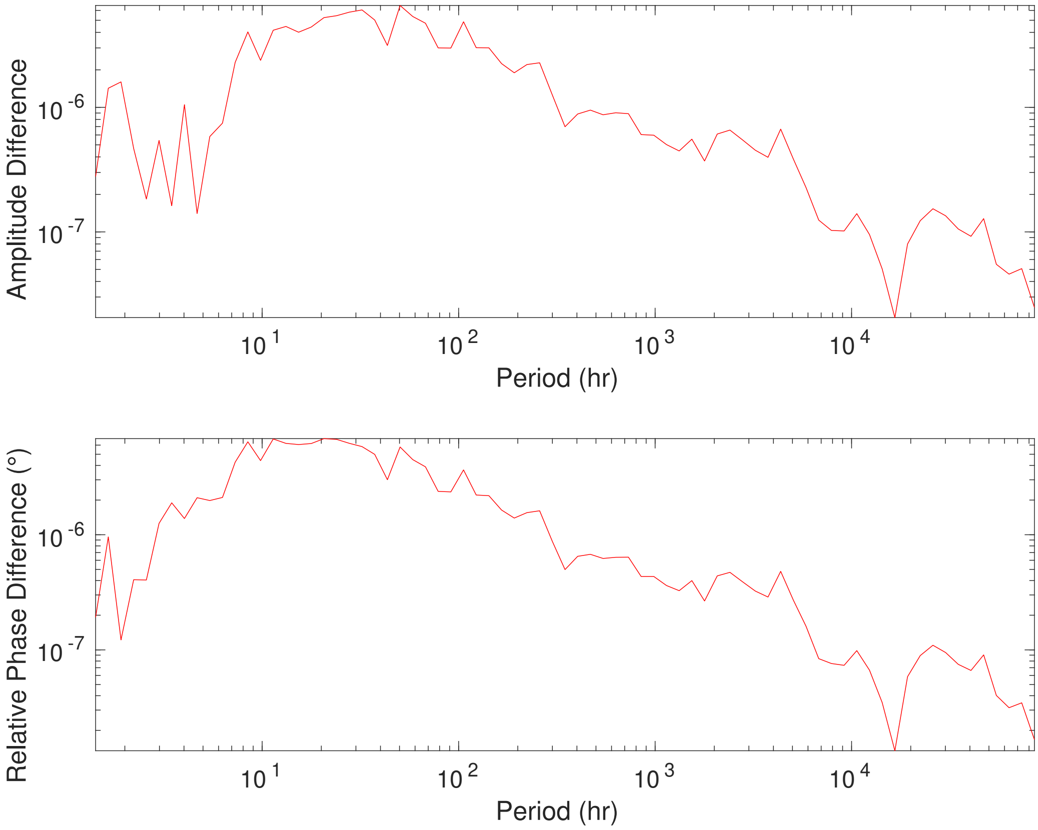


**Figure S2.** Difference of the lines in Figure S1. Absolute values of the difference are plotted so that a log scale may be used to display them. The relative phase difference is shown, i.e. normalized to a maximum of 1. The small differences belie the close overlap of the lines in Figure S1.

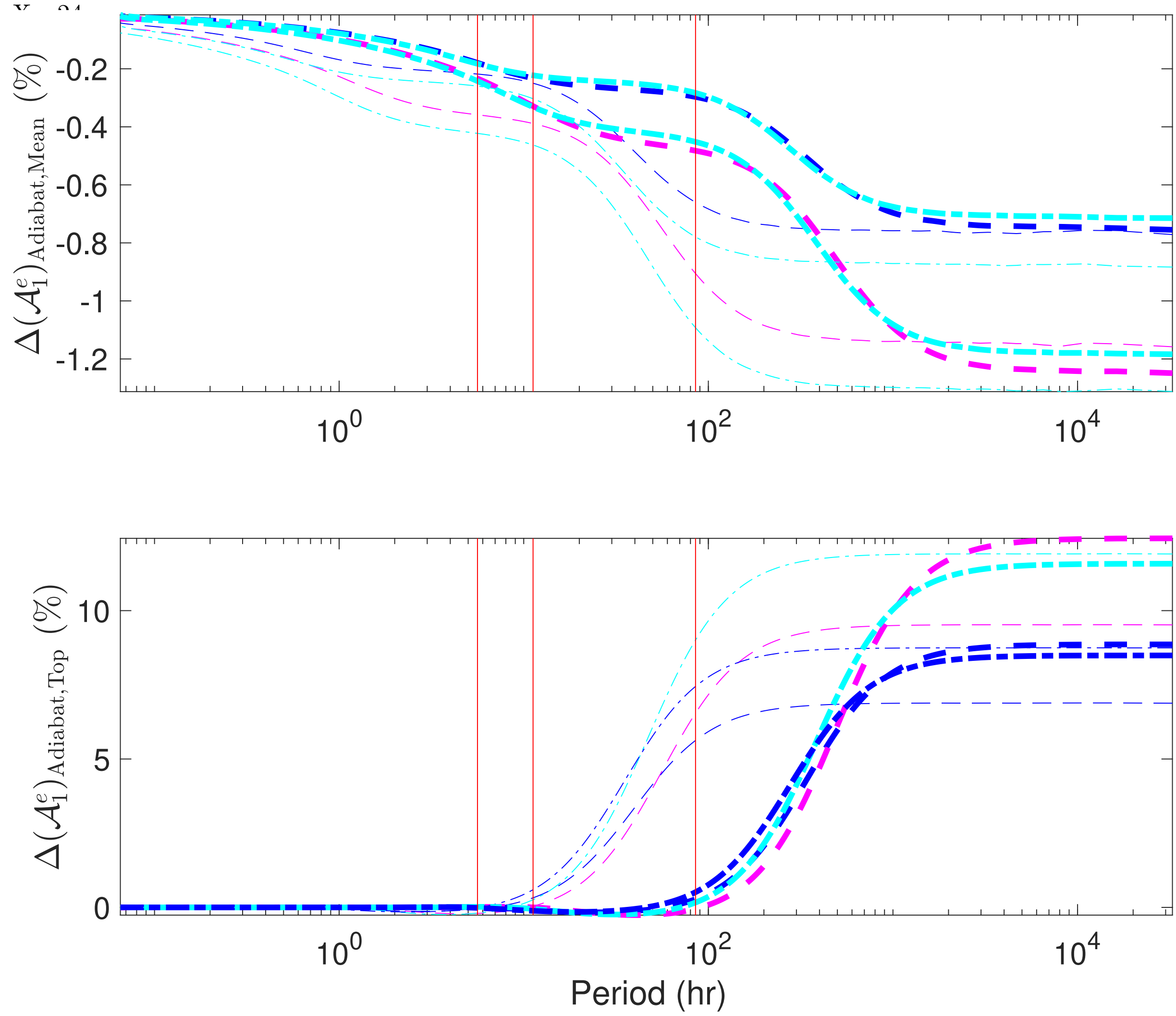


**Figure S3.** Europa: Differences (in %) from the nominal adiabatic case studied here, for uniformly conducting oceans with the equivalent mean conductivity (top panel), and for uniformly conducting oceans with the equivalent conductivity at the ice–ocean interface (bottom panel). Dashed lines (−−) are $MgSO_4$ oceans; dot–dashed lines are seawater oceans (-·-·). Blue curves are for thicker ice (30 km), magenta curves are thinner ice (5 km) $MgSO_4$ oceans, and cyan curves are thinner ice (5 km) seawater oceans. Thick lines are higher salinities (10 wt% and 3.5 Wt%, respectively) for oceans with aqueous $MgSO_4$ and seawater. Thinner lines are for oceans with 10% of those concentrations. Vertical lines are the strongest inducing frequencies shown in Figure 1.

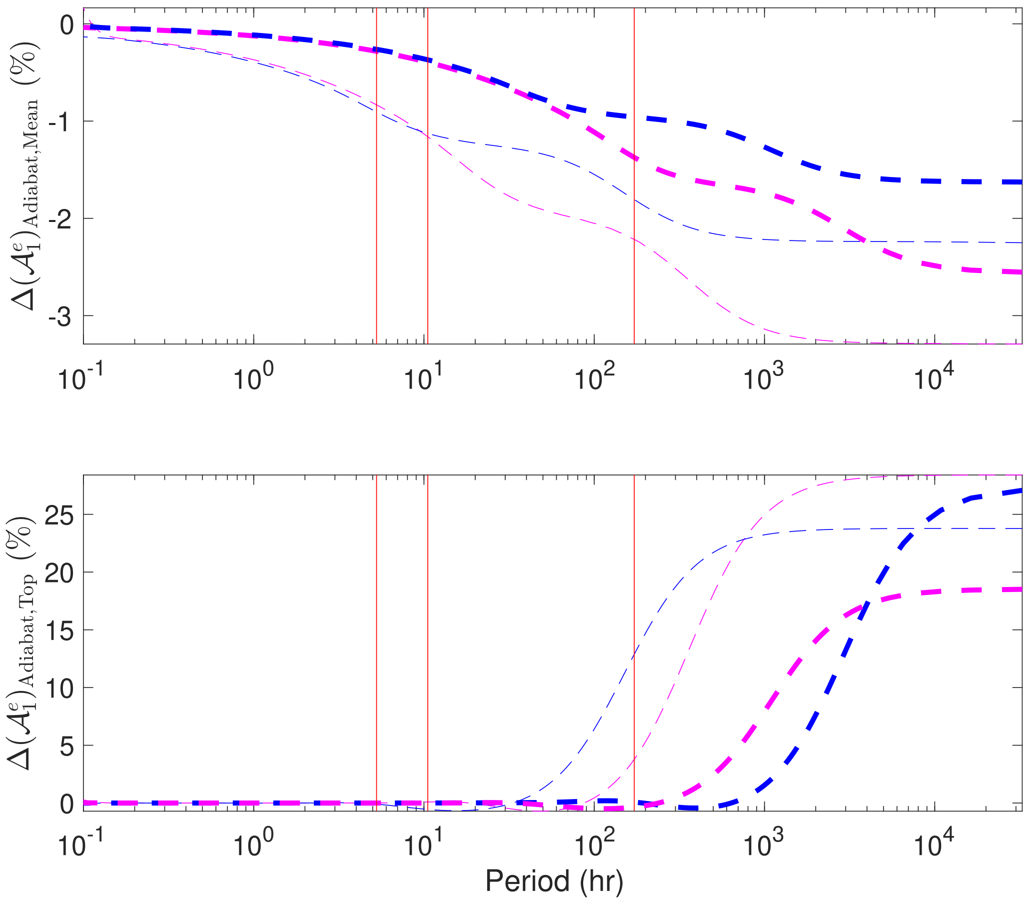


**Figure S4.** Ganymede: Differences (in %) from the nominal adiabatic case studied here for uniformly conducting oceans with the equivalent mean conductivity (top panel), and for uniformly conducting oceans with the equivalent conductivity at the ice–ocean interface (bottom panel). Magenta curves are for thinner ice (∼30 km) and blue curves are for thicker ice (∼100 km). All configurations assume an ocean with aqueous $MgSO_4$. Thick lines are higher salinity (10 wt%) and thinner lines are for oceans with 1 wt%. Vertical lines are the strongest inducing frequencies shown in Figure 1.

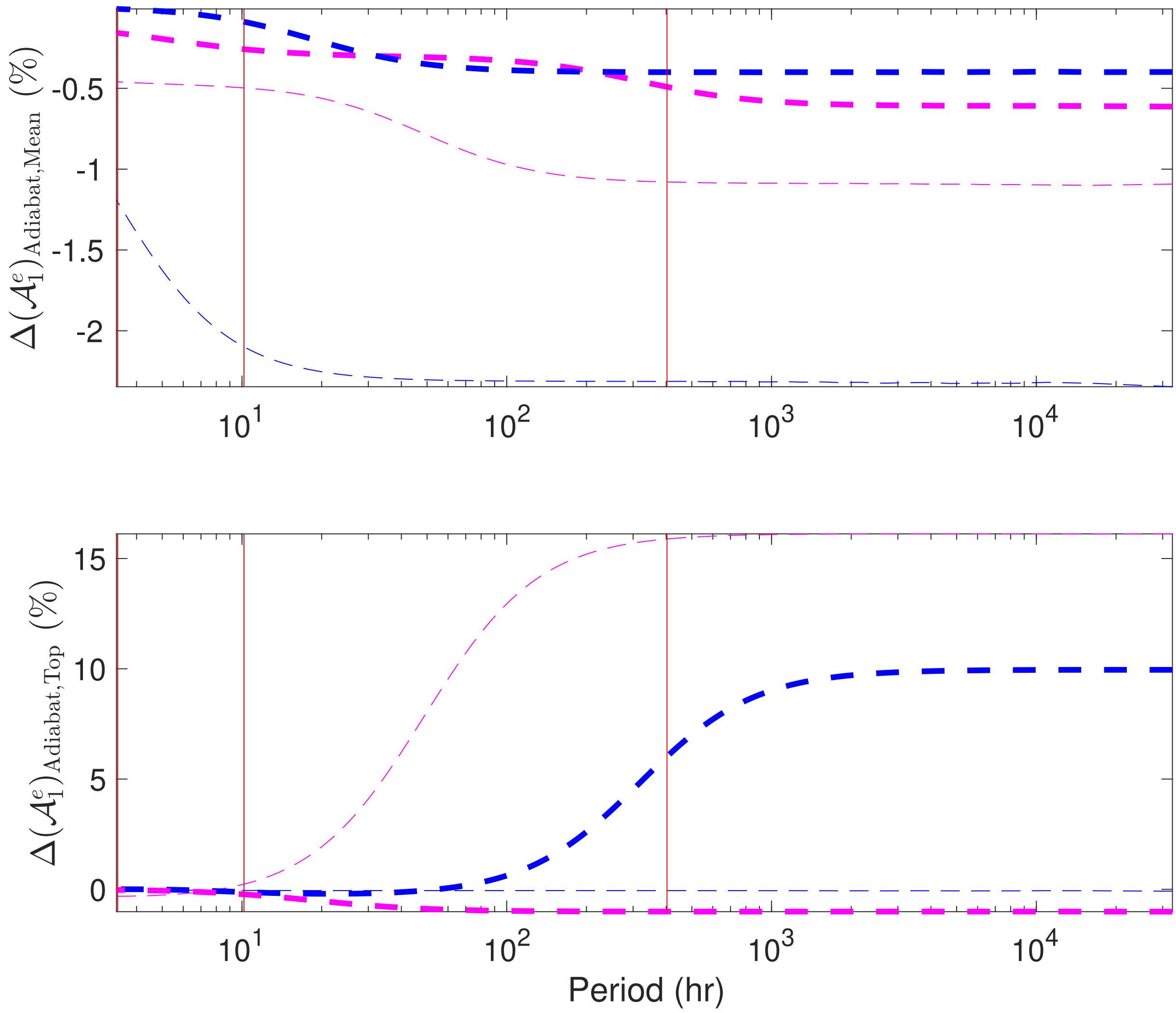


**Figure S5.** Callisto: Differences (in %) from the nominal adiabatic case studied here, for uniformly conducting oceans with the equivalent mean conductivity (top panel) and with for uniformly conducting oceans with the equivalent conductivity at the ice–ocean interface (bottom panel). Magenta curves are for thinner ice (∼30 km) and blue curves are for thicker ice (∼100 km). All configurations assume an ocean with aqueous $MgSO_4$. Thick lines are higher salinity (10 wt%) and thinner lines are for oceans with 1 wt%. Vertical lines are the strongest inducing frequencies shown in Figure 1.

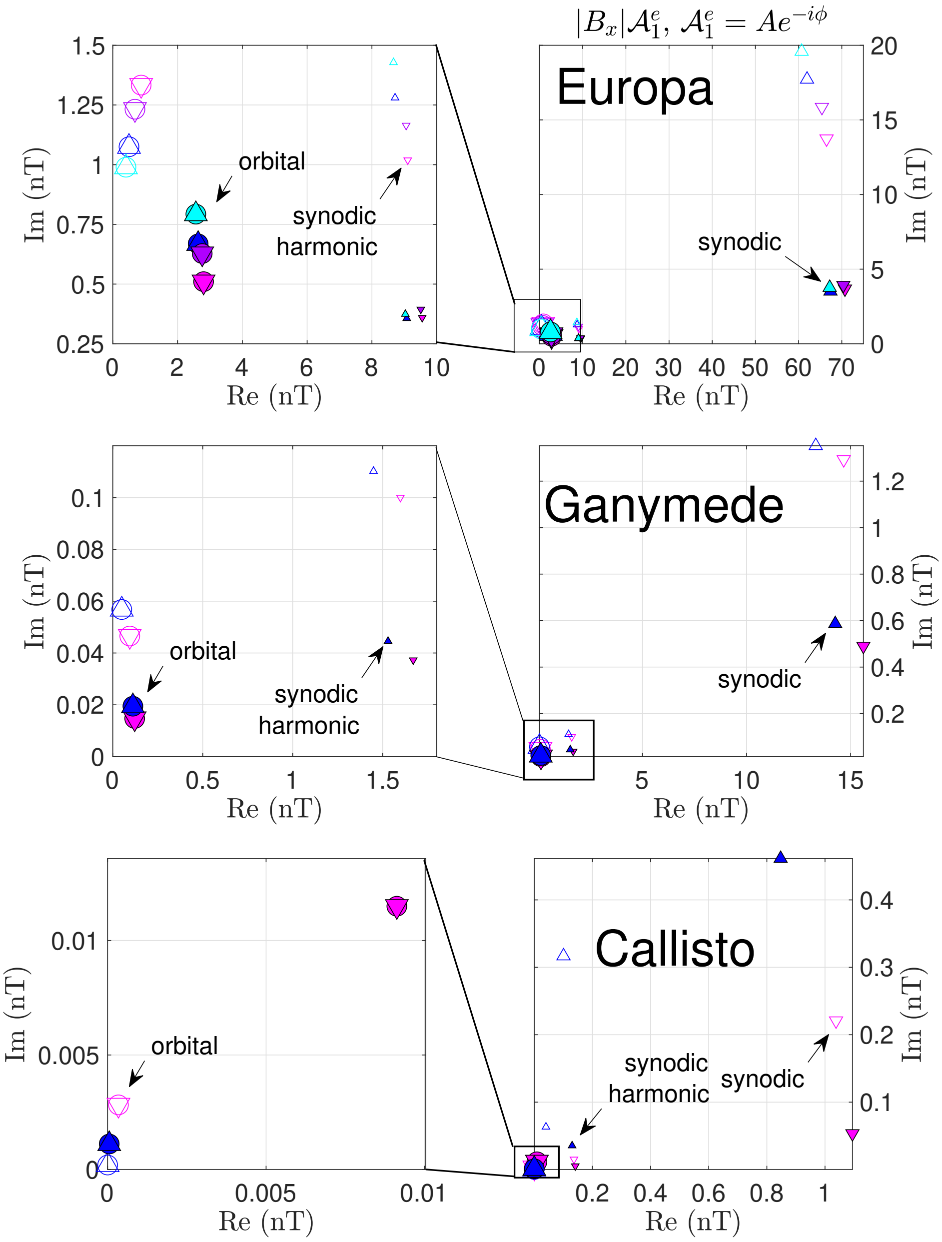


**Figure S6.** Real and imaginary components of the diffusive induction response to the changing $B_x$ component of Jupiter's magnetic field at the main driving periods (Figure 1) for {Europa,Ganymede,Callisto}. The real part (on the $x$-axis) is in phase with the excitation field, and the imaginary part (on the $y$-axis) is 90° out of phase, as detailed in Section 2.6. Subpanels on the left side show the lower-magnitude signals of panels on the right. Filled symbols are for the higher concentrations. Upward and downward triangles are for thicker ice ({30,95,130} km) and thinner ice ({5,26,100} km), respectively. Symbol sizes scale with the period of the oscillation, denoting the orbital (largest), the synodic (intermediate), and the synodic harmonic (smallest). Circles are added to the orbital periods to guide the eye.

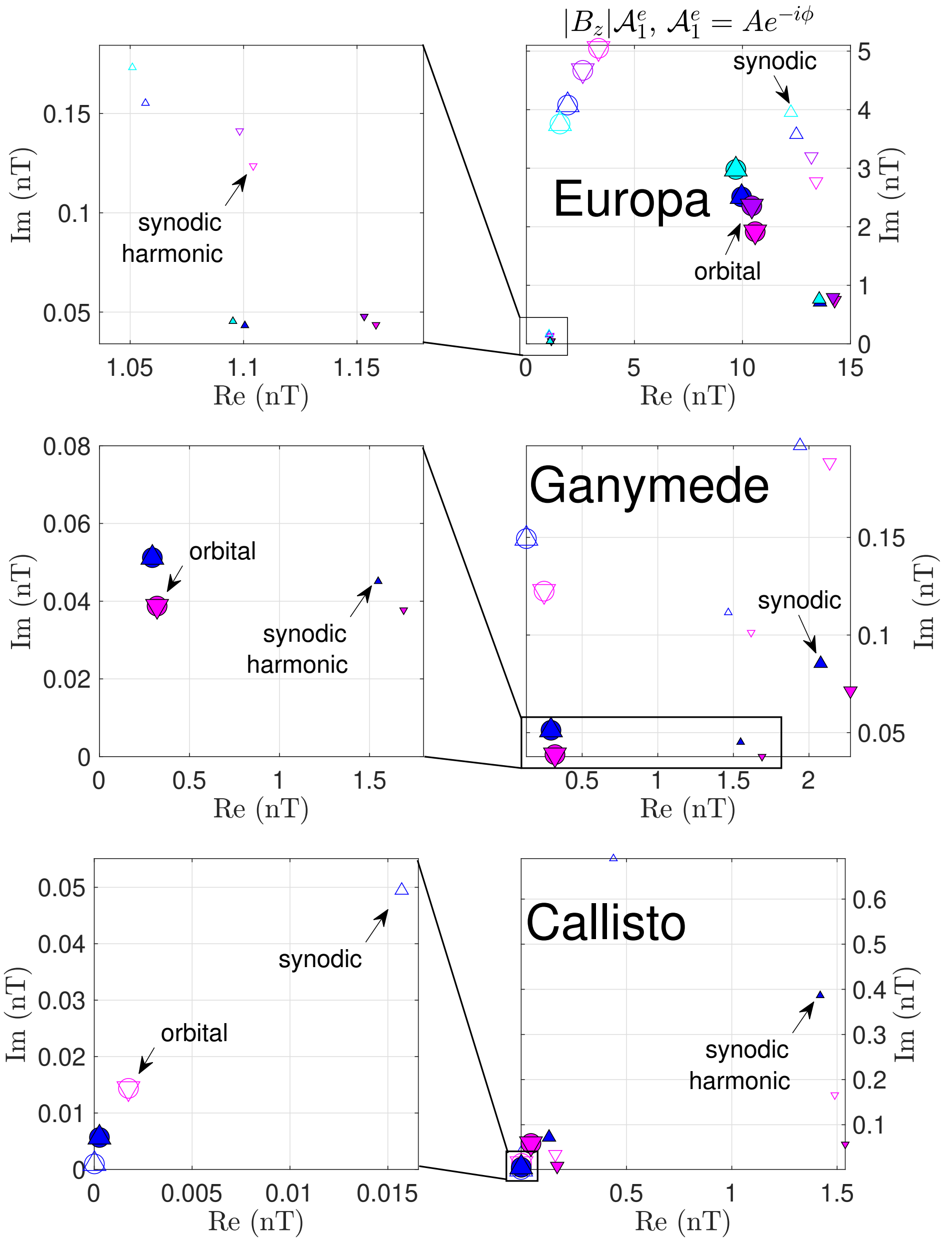


**Figure S7.** Real and imaginary components of the diffusive induction responses to the changing $B_z$ component of Jupiter's magnetic field at the main driving periods (Figure 1) for {Europa,Ganymede,Callisto}. The real part (on the $x$-axis) is in phase with the excitation field, and the imaginary part (on the $y$-axis) is 90° out of phase, as detailed in Section 2.6. Subpanels on the left side show the lower-magnitude signals of panels on the right. Filled symbols are for the higher concentrations. Upward and downward triangles are for thicker ice ({30,95,130} km) and thinner ice ({5,26,100} km), respectively. Symbol sizes scale with the period of the oscillation, denoting the orbital (largest), the synodic (intermediate), and the synodic harmonic (smallest). Circles are added to the orbital periods to guide the eye.

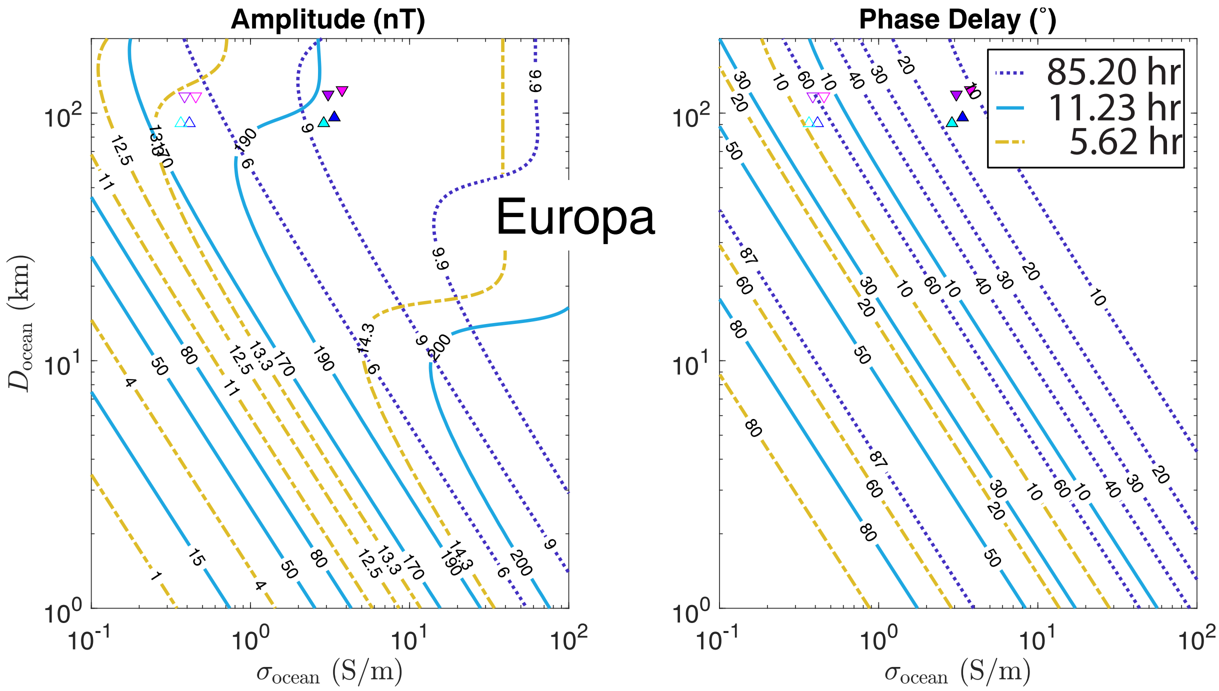


**Figure S8.** Europa: Reproduction of main text Figure 2, with points showing the coordinates of the studied models. The marked points match the identification scheme described in Figure 7.

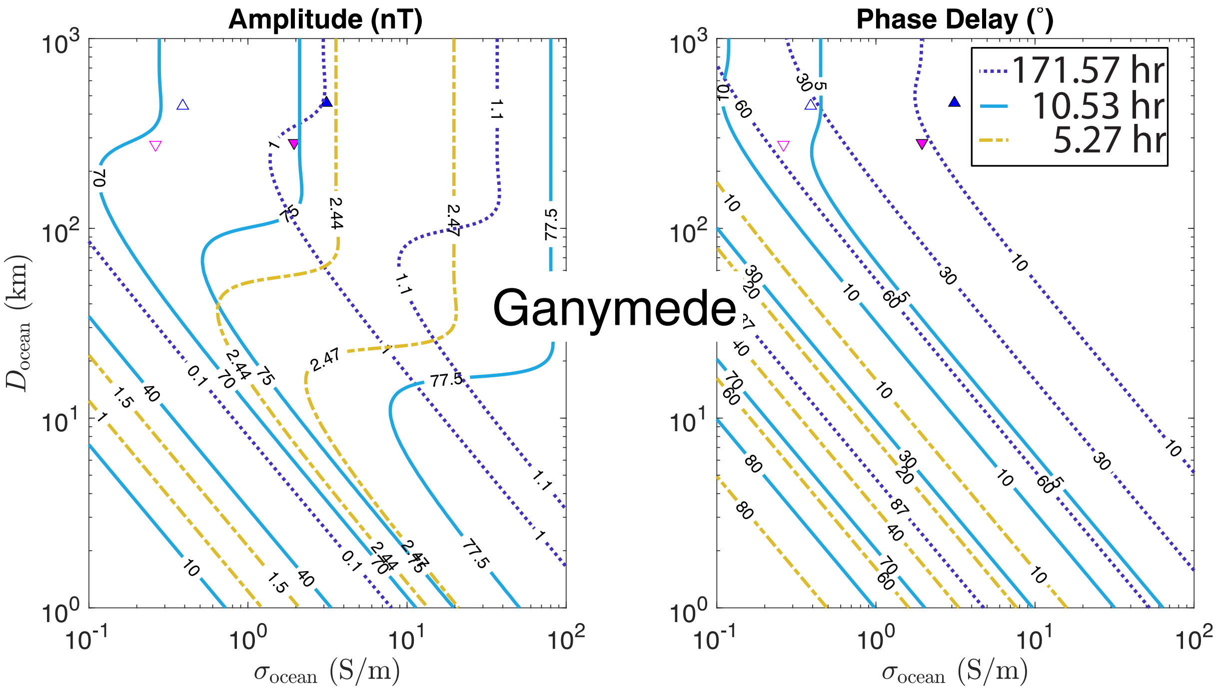


**Figure S9.** Ganymede: Reproduction of main text Figure 3, with points showing the coordinates of the studied models. The marked points match the identification scheme described in Figure 7.

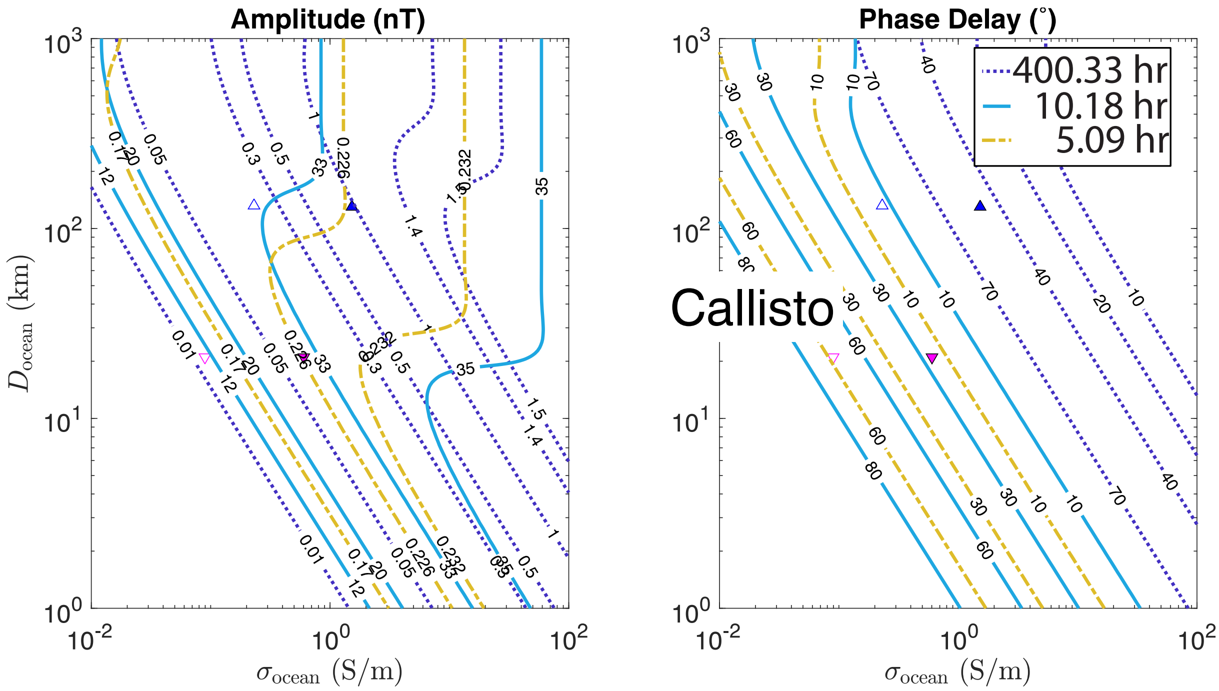


**Figure S10.** Callisto: Reproduction of main text Figure 4, with points showing the coordinates of the studied models. The marked points match the identification scheme described in Figure 7.

| **Europa** | | Period (hr): | | **5.62** | **11.23** | **85.20** |
|---|---|---|---|---|---|---|
| | | $B_x$ (nT): | | **10.03** | **75.55** | **3.17** |
| $T_b$ (K) | $\overline{T}$ (K) | $D_\mathrm{I}$ (km) | $D_\mathrm{ocean}$ (km) | | $B_x\mathcal{A}_1^e$ (nT) | |
| **Ionosphere Only** | | | | **Re Im** | **Re Im** | **Re Im** |
| Pedersen | | | | 0.000 0.069 | 0.001 0.262 | 0.000 0.001 |
| **$MgSO_4$ 1 wt%** | | | | **Re Im** | **Re Im** | **Re Im** |
| 273.1 | 273.9 | 5 | 117 | 9.106 1.019 | 66.471 13.737 | 0.876 1.333 |
| Pedersen | | | | 9.108 1.021 | 66.488 13.741 | 0.877 1.334 |
| $\overline{\sigma} = 0.4533$ S/m | | $\Delta\mathcal{A}_1^e$ (%) | | 0.36 -0.41 | 0.39 -0.08 | 0.85 0.50 |
| $\sigma_\mathrm{top} = 0.4107$ S/m | | $\Delta\mathcal{A}_1^e$ (%) | | 0.10 7.75 | -0.45 8.80 | -12.31 -3.57 |
| 270.4 | 271.1 | 30 | 91 | 8.714 1.280 | 61.952 17.717 | 0.500 1.075 |
| Pedersen | | | | 8.718 1.282 | 61.980 17.723 | 0.501 1.076 |
| $\overline{\sigma} = 0.4132$ S/m | | $\Delta\mathcal{A}_1^e$ (%) | | 0.22 -0.10 | 0.24 0.01 | 0.55 0.34 |
| $\sigma_\mathrm{top} = 0.3847$ S/m | | $\Delta\mathcal{A}_1^e$ (%) | | -0.09 6.49 | -0.88 6.09 | -10.65 -4.23 |
| **$MgSO_4$ 10 wt%** | | | | **Re Im** | **Re Im** | **Re Im** |
| 272.7 | 274.1 | 5 | 124 | 9.552 0.359 | 70.730 3.681 | 2.803 0.510 |
| Pedersen | | | | 9.553 0.361 | 70.733 3.687 | 2.803 0.510 |
| $\overline{\sigma} = 3.7646$ S/m | | $\Delta\mathcal{A}_1^e$ (%) | | 0.23 -3.83 | 0.33 -2.87 | 0.49 -0.10 |
| $\sigma_\mathrm{top} = 3.3197$ S/m | | $\Delta\mathcal{A}_1^e$ (%) | | -0.01 2.28 | -0.01 2.13 | -0.34 11.33 |
| 269.8 | 270.8 | 30 | 96 | 9.075 0.357 | 67.382 3.517 | 2.635 0.668 |
| Pedersen | | | | 9.076 0.359 | 67.386 3.526 | 2.636 0.669 |
| $\overline{\sigma} = 3.3661$ S/m | | $\Delta\mathcal{A}_1^e$ (%) | | 0.18 -2.30 | 0.23 -1.35 | 0.30 0.02 |
| $\sigma_\mathrm{top} = 3.0763$ S/m | | $\Delta\mathcal{A}_1^e$ (%) | | -0.01 1.41 | 0.08 2.77 | -0.81 7.99 |
| **Seawater 0.35165 wt%** | | | | **Re Im** | **Re Im** | **Re Im** |
| 274.9 | 275.7 | 5 | 117 | 9.076 1.102 | 65.860 14.958 | 0.758 1.275 |
| Pedersen | | | | 9.078 1.103 | 65.879 14.961 | 0.759 1.276 |
| $\overline{\sigma} = 0.4124$ S/m | | $\Delta\mathcal{A}_1^e$ (%) | | 0.41 -0.33 | 0.44 -0.04 | 0.96 0.58 |
| $\sigma_\mathrm{top} = 0.3670$ S/m | | $\Delta\mathcal{A}_1^e$ (%) | | 0.05 9.74 | -0.77 10.45 | -15.30 -5.17 |
| 270.0 | 270.7 | 30 | 91 | 8.667 1.428 | 60.705 19.584 | 0.407 0.990 |
| Pedersen | | | | 8.670 1.430 | 60.738 19.589 | 0.408 0.991 |
| $\overline{\sigma} = 0.3651$ S/m | | $\Delta\mathcal{A}_1^e$ (%) | | 0.26 -0.07 | 0.29 0.03 | 0.65 0.42 |
| $\sigma_\mathrm{top} = 0.3339$ S/m | | $\Delta\mathcal{A}_1^e$ (%) | | -0.23 8.27 | -1.49 7.33 | -13.72 -5.87 |
| **Seawater 3.5165 wt%** | | | | **Re Im** | **Re Im** | **Re Im** |
| 270.8 | 271.9 | 5 | 119 | 9.509 0.394 | 70.355 3.930 | 2.761 0.628 |
| Pedersen | | | | 9.510 0.396 | 70.358 3.936 | 2.761 0.628 |
| $\overline{\sigma} = 3.0760$ S/m | | $\Delta\mathcal{A}_1^e$ (%) | | 0.24 -3.32 | 0.33 -2.24 | 0.46 -0.03 |
| $\sigma_\mathrm{top} = 2.7347$ S/m | | $\Delta\mathcal{A}_1^e$ (%) | | -0.02 2.08 | 0.04 2.37 | -0.74 10.53 |
| 268.2 | 269.1 | 30 | 91 | 9.032 0.374 | 67.196 3.767 | 2.564 0.793 |
| Pedersen | | | | 9.033 0.376 | 67.201 3.777 | 2.564 0.793 |
| $\overline{\sigma} = 2.8862$ S/m | | $\Delta\mathcal{A}_1^e$ (%) | | 0.18 -1.89 | 0.22 -0.95 | 0.28 0.03 |
| $\sigma_\mathrm{top} = 2.6476$ S/m | | $\Delta\mathcal{A}_1^e$ (%) | | 0.01 1.46 | 0.10 3.88 | -1.26 7.23 |

**Table S1.** Europa: Magnetic induction field strengths {Re,Im}($B_x\mathcal{A}_n^e$), in nT, at the main inducing periods in Figure 1. For the different ocean compositions and thicknesses of the upper ice I lithosphere/ocean ($D_\mathrm{I}/D_\mathrm{ocean}$; Figure 6), the adiabatic response is listed first. These values are also shown in Figure S6. Following these are the deviations from the adiabatic case (in %) for the responses including a 100 km ionosphere with Pedersen conductance of 30 S (Hartkorn & Saur, 2017), then for the ocean with uniform conductivity set to the mean of the adiabatic ocean ($\overline{\sigma}$), and then for the case with uniform conductivity set to the value at the ice–ocean interface ($\sigma_\mathrm{top}$). The surface responses of the ionosphere in the absence of an ocean are listed at the top of the table.

| **Ganymede** | | | Period (hr): | **5.27** | **10.53** | **171.57** |
|---|---|---|---|---|---|---|
| | | | $B_x$ (nT): | **1.76** | **16.64** | **0.14** |
| $T_b$ (K) | $\overline{T}$ (K) | $D_\mathrm{I}$ (km) | $D_\mathrm{ocean}$ (km) | | $B_x\mathcal{A}_1^e$ (nT) | |
| **Ionosphere Only** | | | | **Re Im** | **Re Im** | **Re Im** |
| Pedersen | | | | 0.000 0.001 | 0.000 0.007 | 0.000 0.000 |
| **$MgSO_4$ 1 wt%** | | | | **Re Im** | **Re Im** | **Re Im** |
| 270.7 | 279.0 | 25 | 442 | 1.598 0.100 | 14.669 1.293 | 0.094 0.047 |
| Pedersen | | | | 1.598 0.100 | 14.669 1.293 | 0.094 0.047 |
| $\overline{\sigma} = 0.5166$ S/m | | $\Delta\mathcal{A}_1^e$ (%) | | 0.87 -8.82 | 1.23 -7.04 | 2.61 1.01 |
| $\sigma_\mathrm{top} = 0.3890$ S/m | | $\Delta\mathcal{A}_1^e$ (%) | | -0.03 4.54 | -0.14 5.86 | -9.33 17.09 |
| 261.6 | 266.2 | 92 | 276 | 1.449 0.110 | 13.326 1.352 | 0.050 0.057 |
| Pedersen | | | | 1.449 0.110 | 13.326 1.353 | 0.050 0.057 |
| $\overline{\sigma} = 0.3322$ S/m | | $\Delta\mathcal{A}_1^e$ (%) | | 0.95 -5.29 | 1.18 -2.65 | 2.44 1.41 |
| $\sigma_\mathrm{top} = 0.2623$ S/m | | $\Delta\mathcal{A}_1^e$ (%) | | 0.08 3.83 | 0.45 10.74 | -22.82 -3.32 |
| **$MgSO_4$ 10 wt%** | | | | **Re Im** | **Re Im** | **Re Im** |
| 270.2 | 278.3 | 25 | 458 | 1.670 0.037 | 15.614 0.490 | 0.122 0.015 |
| Pedersen | | | | 1.670 0.037 | 15.614 0.491 | 0.122 0.015 |
| $\overline{\sigma} = 4.0699$ S/m | | $\Delta\mathcal{A}_1^e$ (%) | | 0.29 -10.57 | 0.41 -9.78 | 1.48 -3.07 |
| $\sigma_\mathrm{top} = 3.1150$ S/m | | $\Delta\mathcal{A}_1^e$ (%) | | -0.00 2.03 | -0.01 2.84 | -0.18 7.55 |
| 260.0 | 263.5 | 93 | 282 | 1.530 0.045 | 14.262 0.586 | 0.112 0.019 |
| Pedersen | | | | 1.530 0.045 | 14.262 0.586 | 0.112 0.019 |
| $\overline{\sigma} = 2.3476$ S/m | | $\Delta\mathcal{A}_1^e$ (%) | | 0.27 -7.17 | 0.38 -6.43 | 1.01 -0.28 |
| $\sigma_\mathrm{top} = 1.9483$ S/m | | $\Delta\mathcal{A}_1^e$ (%) | | 0.00 1.71 | -0.00 2.51 | -0.11 15.65 |
| **bottom layer: 30 km 20 S/m** | | $\Delta\mathcal{A}_1^e$ (%) | | 0.00 -0.00 | 0.00 -0.00 | -1.20 0.20 |
| Pedersen | | $\Delta\mathcal{A}_1^e$ (%) | | 0.00 0.10 | 0.00 0.04 | -1.20 0.20 |

**Table S2.** Ganymede: Magnetic induction field strengths $\{\mathrm{Re,Im}\}(B_x\mathcal{A}_n^e)$, in nT, at the main inducing periods in Figure 1. For the different ocean compositions and thicknesses of the upper ice I lithosphere/ocean ($D_\mathrm{I}/D_\mathrm{ocean}$; Figure 6), the adiabatic response is listed first. These values are also shown in Figure S7. Following these are the deviations from the adiabatic case (in %) for the responses including a 100 km ionosphere with Pedersen conductance of 2 S (Hartkorn & Saur, 2017), then for the ocean with uniform conductivity set to the mean of the adiabatic ocean ($\overline{\sigma}$), and then for the case with uniform conductivity set to the value at the ice–ocean interface ($\sigma_\mathrm{top}$). The surface responses of the ionosphere in the absence of an ocean are listed at the top of the table.

| **Callisto** | | | Period (hr): | **5.09** | | **10.18** | | **400.33** | |
|---|---|---|---|---|---|---|---|---|---|
| | | | $B_x$ (nT): | **0.17** | | **1.31** | | **0.03** | |
| $T_b$ (K) | $\overline{T}$ (K) | $D_{\mathrm{I}}$ (km) | $D_{\mathrm{ocean}}$ (km) | | | $B_x\mathcal{A}_1^e$ (nT) | | | |
| **Ionosphere Only** | | | | **Re** | **Im** | **Re** | **Im** | **Re** | **Im** |
| Pedersen | | | | 0.013 | 0.047 | 0.027 | 0.193 | 0.000 | 0.000 |
| Cowling | | | | 0.154 | 0.065 | 0.832 | 0.701 | 0.000 | 0.001 |
| **$MgSO_4$ 1 wt%** | | | | **Re** | **Im** | **Re** | **Im** | **Re** | **Im** |
| 257.4 | 259.6 | 99 | 132 | 0.137 | 0.015 | 1.038 | 0.221 | 0.000 | 0.003 |
| Pedersen | | | | 0.139 | 0.017 | 1.054 | 0.228 | 0.000 | 0.003 |
| Cowling | | | | 0.154 | 0.024 | 1.159 | 0.250 | 0.001 | 0.004 |
| $\overline{\sigma} = 0.2307$ S/m | | $\Delta\mathcal{A}_1^e$ (%) | | 0.49 | -0.44 | 0.53 | -0.08 | 1.45 | 0.96 |
| $\sigma_{\mathrm{top}} = 0.1965$ S/m | | $\Delta\mathcal{A}_1^e$ (%) | | 0.06 | 14.62 | -1.03 | 15.03 | -26.08 | -13.62 |
| 250.8 | 250.9 | 128 | 21 | 0.040 | 0.063 | 0.101 | 0.317 | 0.000 | 0.000 |
| Pedersen | | | | 0.068 | 0.079 | 0.199 | 0.459 | 0.000 | 0.000 |
| Cowling | | | | 0.159 | 0.055 | 0.950 | 0.656 | 0.000 | 0.001 |
| $\overline{\sigma} = 0.0895$ S/m | | $\Delta\mathcal{A}_1^e$ (%) | | 0.04 | 0.02 | 0.04 | 0.03 | 0.05 | 0.03 |
| $\sigma_{\mathrm{top}} = 0.0874$ S/m | | $\Delta\mathcal{A}_1^e$ (%) | | -3.26 | -0.99 | -4.12 | -1.87 | -4.52 | -2.28 |
| **$MgSO_4$ 10 wt%** | | | | **Re** | **Im** | **Re** | **Im** | **Re** | **Im** |
| 255.7 | 256.9 | 99 | 130 | 0.141 | 0.005 | 1.094 | 0.053 | 0.009 | 0.011 |
| Pedersen | | | | 0.142 | 0.007 | 1.098 | 0.062 | 0.009 | 0.012 |
| Cowling | | | | 0.151 | 0.018 | 1.135 | 0.118 | 0.010 | 0.012 |
| $\overline{\sigma} = 1.5256$ S/m | | $\Delta\mathcal{A}_1^e$ (%) | | 0.20 | -2.91 | 0.26 | -1.74 | 0.69 | 0.39 |
| $\sigma_{\mathrm{top}} = 1.3789$ S/m | | $\Delta\mathcal{A}_1^e$ (%) | | 0.01 | 1.12 | 0.12 | 3.18 | -10.78 | -1.59 |
| 250.8 | 250.9 | 128 | 21 | 0.130 | 0.035 | 0.847 | 0.461 | 0.000 | 0.001 |
| Pedersen | | | | 0.135 | 0.037 | 0.897 | 0.467 | 0.000 | 0.001 |
| Cowling | | | | 0.160 | 0.033 | 1.146 | 0.419 | 0.000 | 0.002 |
| $\overline{\sigma} = 0.6025$ S/m | | $\Delta\mathcal{A}_1^e$ (%) | | -0.00 | -0.00 | -0.00 | -0.00 | -0.00 | -0.00 |
| $\sigma_{\mathrm{top}} = 0.6062$ S/m | | $\Delta\mathcal{A}_1^e$ (%) | | 0.08 | -0.53 | 0.28 | -0.34 | 1.23 | 0.61 |

**Table S3.** Callisto: Magnetic induction field strengths $\{\mathrm{Re},\mathrm{Im}\}(B_x\mathcal{A}_n^e)$, in nT, at the main inducing periods in Figure 1. For the different ocean compositions and thicknesses of the upper ice I lithosphere/ocean ($D_{\mathrm{I}}/D_{\mathrm{ocean}}$; Figure 6), the adiabatic response is listed first. These values are also shown in Figure S6. Following these are the responses (in nT) including a 100 km ionosphere with {Pedersen,Cowling} conductance of {800,6850} S (Hartkorn & Saur, 2017), then the deviations from the adiabatic case (in %) for the ocean with uniform conductivity set to the mean of the adiabatic ocean ($\overline{\sigma}$), and then for the case with uniform conductivity set to the value at the ice–ocean interface ($\sigma_{\mathrm{top}}$). The surface responses of the ionosphere in the absence of an ocean are listed at the top of the table.

| **Europa** | | Period (hr): | | **5.62** | **11.23** | **84.63** |
|---|---|---|---|---|---|---|
| | | $B_z$ (nT): | | **1.22** | **15.24** | **11.97** |
| $T_b$ (K) | $\overline{T}$ (K) | $D_{\mathrm{I}}$ (km) | $D_{\mathrm{ocean}}$ (km) | | $B_z\mathcal{A}_1^e$ (nT) | |
| **Ionosphere Only** | | | | **Re Im** | **Re Im** | **Re Im** |
| Pedersen | | | | 0.000 0.008 | 0.000 0.053 | 0.000 0.006 |
| **$MgSO_4$ 1 wt%** | | | | **Re Im** | **Re Im** | **Re Im** |
| 273.1 | 273.9 | 5 | 117 | 1.104 0.124 | 13.409 2.771 | 3.339 5.049 |
| Pedersen | | | | 1.105 0.124 | 13.412 2.772 | 3.342 5.052 |
| $\overline{\sigma} = 0.4533$ S/m | | $\Delta\mathcal{A}_1^e$ (%) | | 0.36 -0.41 | 0.39 -0.08 | 0.85 0.50 |
| $\sigma_{\mathrm{top}} = 0.4107$ S/m | | $\Delta\mathcal{A}_1^e$ (%) | | 0.10 7.75 | -0.45 8.80 | -12.31 -3.57 |
| 270.4 | 271.1 | 30 | 91 | 1.057 0.155 | 12.497 3.574 | 1.910 4.078 |
| Pedersen | | | | 1.057 0.155 | 12.503 3.575 | 1.913 4.082 |
| $\overline{\sigma} = 0.4132$ S/m | | $\Delta\mathcal{A}_1^e$ (%) | | 0.22 -0.10 | 0.24 0.01 | 0.55 0.34 |
| $\sigma_{\mathrm{top}} = 0.3847$ S/m | | $\Delta\mathcal{A}_1^e$ (%) | | -0.09 6.49 | -0.88 6.09 | -10.65 -4.23 |
| **$MgSO_4$ 10 wt%** | | | | **Re Im** | **Re Im** | **Re Im** |
| 272.7 | 274.1 | 5 | 124 | 1.158 0.044 | 14.268 0.743 | 10.590 1.916 |
| Pedersen | | | | 1.158 0.044 | 14.268 0.744 | 10.591 1.916 |
| $\overline{\sigma} = 3.7646$ S/m | | $\Delta\mathcal{A}_1^e$ (%) | | 0.23 -3.83 | 0.33 -2.87 | 0.49 -0.10 |
| $\sigma_{\mathrm{top}} = 3.3197$ S/m | | $\Delta\mathcal{A}_1^e$ (%) | | -0.01 2.28 | -0.01 2.13 | -0.34 11.33 |
| 269.8 | 270.8 | 30 | 96 | 1.101 0.043 | 13.592 0.709 | 9.962 2.510 |
| Pedersen | | | | 1.101 0.044 | 13.593 0.711 | 9.963 2.510 |
| $\overline{\sigma} = 3.3661$ S/m | | $\Delta\mathcal{A}_1^e$ (%) | | 0.18 -2.30 | 0.23 -1.35 | 0.30 0.02 |
| $\sigma_{\mathrm{top}} = 3.0763$ S/m | | $\Delta\mathcal{A}_1^e$ (%) | | -0.01 1.41 | 0.08 2.77 | -0.81 7.99 |
| **Seawater 0.35165 wt%** | | | | **Re Im** | **Re Im** | **Re Im** |
| 274.9 | 275.7 | 5 | 117 | 1.101 0.134 | 13.285 3.017 | 2.893 4.833 |
| Pedersen | | | | 1.101 0.134 | 13.289 3.018 | 2.896 4.836 |
| $\overline{\sigma} = 0.4124$ S/m | | $\Delta\mathcal{A}_1^e$ (%) | | 0.41 -0.33 | 0.44 -0.04 | 0.96 0.58 |
| $\sigma_{\mathrm{top}} = 0.3670$ S/m | | $\Delta\mathcal{A}_1^e$ (%) | | 0.05 9.74 | -0.77 10.45 | -15.30 -5.17 |
| 270.0 | 270.7 | 30 | 91 | 1.051 0.173 | 12.245 3.951 | 1.556 3.755 |
| Pedersen | | | | 1.051 0.173 | 12.252 3.952 | 1.559 3.759 |
| $\overline{\sigma} = 0.3651$ S/m | | $\Delta\mathcal{A}_1^e$ (%) | | 0.26 -0.07 | 0.29 0.03 | 0.65 0.42 |
| $\sigma_{\mathrm{top}} = 0.3339$ S/m | | $\Delta\mathcal{A}_1^e$ (%) | | -0.23 8.27 | -1.49 7.33 | -13.72 -5.87 |
| **Seawater 3.5165 wt%** | | | | **Re Im** | **Re Im** | **Re Im** |
| 270.8 | 271.9 | 5 | 119 | 1.153 0.048 | 14.192 0.793 | 10.435 2.358 |
| Pedersen | | | | 1.153 0.048 | 14.193 0.794 | 10.435 2.358 |
| $\overline{\sigma} = 3.0760$ S/m | | $\Delta\mathcal{A}_1^e$ (%) | | 0.24 -3.32 | 0.33 -2.24 | 0.46 -0.03 |
| $\sigma_{\mathrm{top}} = 2.7347$ S/m | | $\Delta\mathcal{A}_1^e$ (%) | | -0.02 2.08 | 0.04 2.37 | -0.74 10.53 |
| 268.2 | 269.1 | 30 | 91 | 1.095 0.045 | 13.555 0.760 | 9.695 2.979 |
| Pedersen | | | | 1.095 0.046 | 13.556 0.762 | 9.696 2.979 |
| $\overline{\sigma} = 2.8862$ S/m | | $\Delta\mathcal{A}_1^e$ (%) | | 0.18 -1.89 | 0.22 -0.95 | 0.28 0.03 |
| $\sigma_{\mathrm{top}} = 2.6476$ S/m | | $\Delta\mathcal{A}_1^e$ (%) | | 0.01 1.46 | 0.10 3.88 | -1.26 7.23 |

**Table S4.** Europa: Magnetic induction field strengths $\{\mathrm{Re},\mathrm{Im}\}(B_z\mathcal{A}_n^e)$, in nT, at the main inducing periods in Figure 1. For the different ocean compositions and thicknesses of the upper ice I lithosphere/ocean ($D_{\mathrm{I}}/D_{\mathrm{ocean}}$; Figure 6), the adiabatic response is listed first. These values are also shown in Figure S6. Following these are the deviations from the adiabatic case (in %) for the responses including a 100 km ionosphere with Pedersen conductance of 30 S (Hartkorn & Saur, 2017), then for the ocean with uniform conductivity set to the mean of the adiabatic ocean ($\overline{\sigma}$), and then for the case with uniform conductivity set to the value at the ice–ocean interface ($\sigma_{\mathrm{top}}$). The surface responses of the ionosphere in the absence of an ocean are listed at the top of the table.

| **Ganymede** | | | Period (hr): | **5.27** | **10.53** | **171.57** |
|---|---|---|---|---|---|---|
| | | | $B_z$ (nT): | **1.78** | **2.42** | **0.38** |
| $T_b$ (K) | $\overline{T}$ (K) | $D_\mathrm{I}$ (km) | $D_\mathrm{ocean}$ (km) | | $B_z \mathcal{A}_1^e$ (nT) | |
| **Ionosphere Only** | | | | **Re Im** | **Re Im** | **Re Im** |
| Pedersen | | | | 0.000 0.001 | 0.000 0.001 | 0.000 0.000 |
| **$MgSO_4$ 1 wt%** | | | | **Re Im** | **Re Im** | **Re Im** |
| 270.7 | 279.0 | 25 | 442 | 1.618 0.101 | 2.137 0.188 | 0.248 0.122 |
| Pedersen | | | | 1.618 0.101 | 2.137 0.188 | 0.248 0.122 |
| $\overline{\sigma} = 0.5166$ S/m | | | $\Delta\mathcal{A}_1^e$ (%) | 0.87 -8.82 | 1.23 -7.04 | 2.61 1.01 |
| $\sigma_\mathrm{top} = 0.3890$ S/m | | | $\Delta\mathcal{A}_1^e$ (%) | -0.03 4.54 | -0.14 5.86 | -9.33 17.09 |
| 261.6 | 266.2 | 92 | 276 | 1.466 0.112 | 1.941 0.197 | 0.131 0.149 |
| Pedersen | | | | 1.466 0.112 | 1.941 0.197 | 0.131 0.149 |
| $\overline{\sigma} = 0.3322$ S/m | | | $\Delta\mathcal{A}_1^e$ (%) | 0.95 -5.29 | 1.18 -2.65 | 2.44 1.41 |
| $\sigma_\mathrm{top} = 0.2623$ S/m | | | $\Delta\mathcal{A}_1^e$ (%) | 0.08 3.83 | 0.45 10.74 | -22.82 -3.32 |
| **$MgSO_4$ 10 wt%** | | | | **Re Im** | **Re Im** | **Re Im** |
| 270.2 | 278.3 | 25 | 458 | 1.690 0.038 | 2.274 0.071 | 0.320 0.039 |
| Pedersen | | | | 1.690 0.038 | 2.274 0.071 | 0.320 0.039 |
| $\overline{\sigma} = 4.0699$ S/m | | | $\Delta\mathcal{A}_1^e$ (%) | 0.29 -10.57 | 0.41 -9.78 | 1.48 -3.07 |
| $\sigma_\mathrm{top} = 3.1150$ S/m | | | $\Delta\mathcal{A}_1^e$ (%) | -0.00 2.03 | -0.01 2.84 | -0.18 7.55 |
| 260.0 | 263.5 | 93 | 282 | 1.548 0.045 | 2.077 0.085 | 0.294 0.051 |
| Pedersen | | | | 1.548 0.045 | 2.077 0.085 | 0.294 0.051 |
| $\overline{\sigma} = 2.3476$ S/m | | | $\Delta\mathcal{A}_1^e$ (%) | 0.27 -7.17 | 0.38 -6.43 | 1.01 -0.28 |
| $\sigma_\mathrm{top} = 1.9483$ S/m | | | $\Delta\mathcal{A}_1^e$ (%) | 0.00 1.71 | -0.00 2.51 | -0.11 15.65 |
| **bottom layer: 30 km 20 S/m** | | | $\Delta\mathcal{A}_1^e$ (%) | 0.00 -0.00 | 0.00 -0.00 | -1.20 0.20 |
| Pedersen | | | $\Delta\mathcal{A}_1^e$ (%) | 0.00 0.10 | 0.00 0.04 | -1.20 0.20 |

**Table S5.** Ganymede: Magnetic induction field strengths $\{\mathrm{Re,Im}\}(B_z \mathcal{A}_n^e)$, in nT, at the main inducing periods in Figure 1. For the different ocean compositions and thicknesses of the upper ice I lithosphere/ocean ($D_\mathrm{I}/D_\mathrm{ocean}$; Figure 6), the adiabatic response is listed first. These values are also shown in Figure S7. Following these are the deviations from the adiabatic case (in %) for the responses including a 100 km ionosphere with Pedersen conductance of 2 S (Hartkorn & Saur, 2017), then for the ocean with uniform conductivity set to the mean of the adiabatic ocean ($\overline{\sigma}$), and then for the case with uniform conductivity set to the value at the ice–ocean interface ($\sigma_\mathrm{top}$). The surface responses of the ionosphere in the absence of an ocean are listed at the top of the table.

| **Callisto** | | | Period (hr): | **5.09** | | **10.18** | | **400.33** | |
|---|---|---|---|---|---|---|---|---|---|
| | | | $B_z$ (nT): | **1.82** | | **0.20** | | **0.14** | |
| $T_b$ (K) | $\overline{T}$ (K) | $D_\mathrm{I}$ (km) | $D_\mathrm{ocean}$ (km) | | | $B_z\mathcal{A}_1^e$ (nT) | | | |
| **Ionosphere Only** | | | | **Re** | **Im** | **Re** | **Im** | **Re** | **Im** |
| Pedersen | | | | 0.141 | 0.508 | 0.004 | 0.030 | 0.000 | 0.001 |
| Cowling | | | | 1.677 | 0.708 | 0.130 | 0.110 | 0.000 | 0.005 |
| **$MgSO_4$ 1 wt%** | | | | **Re** | **Im** | **Re** | **Im** | **Re** | **Im** |
| 257.4 | 259.6 | 99 | 132 | 1.489 | 0.166 | 0.162 | 0.034 | 0.002 | 0.014 |
| Pedersen | | | | 1.511 | 0.190 | 0.165 | 0.036 | 0.002 | 0.015 |
| Cowling | | | | 1.683 | 0.265 | 0.181 | 0.039 | 0.003 | 0.019 |
| $\overline{\sigma} = 0.2307$ S/m | | | $\Delta\mathcal{A}_1^e$ (%) | 0.49 | -0.44 | 0.53 | -0.08 | 1.45 | 0.96 |
| $\sigma_\mathrm{top} = 0.1965$ S/m | | | $\Delta\mathcal{A}_1^e$ (%) | 0.06 | 14.62 | -1.03 | 15.03 | -26.08 | -13.62 |
| 250.8 | 250.9 | 128 | 21 | 0.438 | 0.690 | 0.016 | 0.049 | 0.000 | 0.001 |
| Pedersen | | | | 0.746 | 0.865 | 0.031 | 0.072 | 0.000 | 0.002 |
| Cowling | | | | 1.738 | 0.603 | 0.148 | 0.102 | 0.000 | 0.006 |
| $\overline{\sigma} = 0.0895$ S/m | | | $\Delta\mathcal{A}_1^e$ (%) | 0.04 | 0.02 | 0.04 | 0.03 | 0.05 | 0.03 |
| $\sigma_\mathrm{top} = 0.0874$ S/m | | | $\Delta\mathcal{A}_1^e$ (%) | -3.26 | -0.99 | -4.12 | -1.87 | -4.52 | -2.28 |
| **$MgSO_4$ 10 wt%** | | | | **Re** | **Im** | **Re** | **Im** | **Re** | **Im** |
| 255.7 | 256.9 | 99 | 130 | 1.539 | 0.057 | 0.171 | 0.008 | 0.046 | 0.059 |
| Pedersen | | | | 1.546 | 0.079 | 0.171 | 0.010 | 0.047 | 0.059 |
| Cowling | | | | 1.648 | 0.195 | 0.177 | 0.018 | 0.049 | 0.060 |
| $\overline{\sigma} = 1.5256$ S/m | | | $\Delta\mathcal{A}_1^e$ (%) | 0.20 | -2.91 | 0.26 | -1.74 | 0.69 | 0.39 |
| $\sigma_\mathrm{top} = 1.3789$ S/m | | | $\Delta\mathcal{A}_1^e$ (%) | 0.01 | 1.12 | 0.12 | 3.18 | -10.78 | -1.59 |
| 250.8 | 250.9 | 128 | 21 | 1.420 | 0.386 | 0.132 | 0.072 | 0.000 | 0.006 |
| Pedersen | | | | 1.476 | 0.399 | 0.140 | 0.073 | 0.000 | 0.006 |
| Cowling | | | | 1.743 | 0.358 | 0.179 | 0.065 | 0.001 | 0.010 |
| $\overline{\sigma} = 0.6025$ S/m | | | $\Delta\mathcal{A}_1^e$ (%) | -0.00 | -0.00 | -0.00 | -0.00 | -0.00 | -0.00 |
| $\sigma_\mathrm{top} = 0.6062$ S/m | | | $\Delta\mathcal{A}_1^e$ (%) | 0.08 | -0.53 | 0.28 | -0.34 | 1.23 | 0.61 |

**Table S6.** Callisto: Magnetic induction field strengths {Re,Im}$(B_z\mathcal{A}_n^e)$, in nT, at the main inducing periods in Figure 1. For the different ocean compositions and thicknesses of the upper ice I lithosphere/ocean ($D_\mathrm{I}/D_\mathrm{ocean}$; Figure 6), the adiabatic response is listed first. These values are also shown in Figure S6. Following these are the responses (in nT) including a 100 km ionosphere with {Pedersen,Cowling} conductance of {800,6850} S (Hartkorn & Saur, 2017), then the deviations from the adiabatic case (in %) for the ocean with uniform conductivity set to the mean of the adiabatic ocean ($\overline{\sigma}$), and then for the case with uniform conductivity set to the value at the ice–ocean interface ($\sigma_\mathrm{top}$). The surface responses of the ionosphere in the absence of an ocean are listed at the top of the table.